Development of Designer-Relevant Lattice-Boltzmann Wind Field Model for Urban Canyons and Their Neighborhoods

By

Tianyi Chen

B.Eng. Environment Engineering
Tsinghua University, China, 2014

SUBMITTED TO THE DEPARTMENT OF MECHANICAL ENGINEERING IN PARTIAL FULFILLMENT OF THE REQUIREMENTS FOR THE DEGREE OF

MASTER OF SCIENCE IN MECHANICAL ENGINEERING
AT THE
MASSACHUSETTS INSTITUTE OF TECHNOLOGY
JUNE 2016

Signature of Author: Signature redacted
Department of Mechanical Engineering
May 6, 2016

Certified by: Signature redacted
Leslie K. Norford
Professor of Building Technology
Thesis Supervisor

Certified by: Signature redacted
Steven B. Leeb
Professor of Mechanical Engineering and Electrical Engineering
Reader in Department

Accepted by: Signature redacted
Rohan C. Abeyaratne
Professor of Mechanical Engineering
Chairman, Committee for Graduate Theses

Development of Designer-Relevant Lattice-Boltzmann Wind Field Model for Urban Canyons and Their Neighborhoods

By

Tianyi Chen

Submitted to the Department of Mechanical Engineering on May 6, 2016
in Partial Fulfillment of the Requirements for the Degree of
Master of Science in Mechanical Engineering

ABSTRACT

Wind field analysis is one of the most important components for designers to achieve a thermally-comfortable and energy-efficient building design. Designers need a fast and relatively accurate wind field model to get integrated into the design workflow, but current platforms to work on are either costly and time-consuming conventional Computational Fluid Dynamics (CFD) tools or over-simplified data correlation factors, which makes the workflow undesirable for designers' use.

In this thesis, a novel Lattice-Boltzmann Wind Field Model (LBWFM) is developed and integrated in a designer-relevant Rhino-based environment. Lattice-Boltzmann Method (LBM) is introduced as the solver due to its open-source and parallelism natures, and coded in C# language for three-dimensional urban airflows. Results of the model are validated with experimental measurements as well as conventional CFD tools for both wind velocity and pressure fields. To further enhance the computational efficiency, proper settings of inlet wind profile and optimal modeling domain size are investigated for the LBWFM. And the relative wind pressure coefficient calculated out of the model is then applied in the analysis of wind-driven natural ventilation potential with the indicator of air exchange flow rate. Finally the limitation of the model is stated and future work is discussed on the modifications of buoyancy effect and potential extension is addressed in the application of LBWFM.

Thesis Supervisor: Leslie K. Norford
Title: Professor of Building Technology

Reader in Department: Steven B. Leeb
Title: Professor of Mechanical Engineering and Electrical Engineering

Acknowledgment

I am very grateful to my advisor, Prof. Leslie K. Norford, for his mentoring, guidance and support on both my academics and research. Two years before, I was new to the area of building technology when I first came to MIT. With his passion and patience on the introduction to the scope of research interests, I became more and more informed and motivated to my research topic of development of a designer-relevant wind field model. I admire his kindness to share his new thoughts and ideas with me, and appreciate his encouragement when I got stuck and felt frustrated. I have also learned a lot from his rigorous attitude to the research work, especially his comments on every word and sign in the thesis. I really look forward to my continuous work with him in the coming years for my PhD.

I am also thankful to Prof. Steven B. Leeb, my thesis reader from the Department of Mechanical Engineering. He provided his valuable advice in my course selection and helpful comments on my thesis as well.

I would also like to thank the entire faculty and labmates in the Building Technology Program as well as faculty members from the Department of Mechanical Engineering. Special thanks to Prof. Leon Glicksman for his comments on the natural ventilation potential analysis, and to Dr. Timur Dogan for his efforts on the connections of the model with Grasshopper components. Many thanks for Prof. Christoph Reinhart and Prof. Leslie K. Norford to apply the Lattice-Boltzmann wind field model into real urban site modeling in their class contents and test the robustness and applicability of the model through class assignments. Also thanks for Prof. Rex Britter and Dr. Chao Yuan who gave me insightful instructions on the fundamentals and simulations of urban airflow modeling. Additional thanks to Kathleen Ross and Leslie Regan, whose commitment and spirits made the everyday work convenient and enjoyable.

Finally, I would like to thank my parents and grandparents as well as my friends who were always standing behind me, devoting their strong love, support and encouragement to my studies and work in MIT. They inspired me to do my best and provided every care on my life here.

The research has been funded by the MI-MIT (Masdar Institute — Massachusetts Institute of Technology) flagship project, Development of advanced microclimate and urban energy analysis modeling environment and its validation by wide area sensor networks and remote sensing for future adaptation of urban infrastructure.

Contents

List of Figures

List of Tables

Chapter 1

Introduction

1.1 Background

With the fast pace of urbanization, the outdoor air temperature in urban areas is increasing compared to rural areas, a phenomenon known as the Urban Heat Island (UHI) effect. Thermal mass is concentrated in the urban areas where building densities are relatively high, solar and anthropogenic heat is trapped and air temperature goes up. As is shown in Fig 1.1, the outdoor air temperature remains at a low level in the rural areas until at the edge of suburban areas, where buildings become piled up and air temperature climbs up the "cliff." Close to the urban center, ambient temperature arrives at the peak level and the temperature difference between rural and urban areas reaches the maximum.

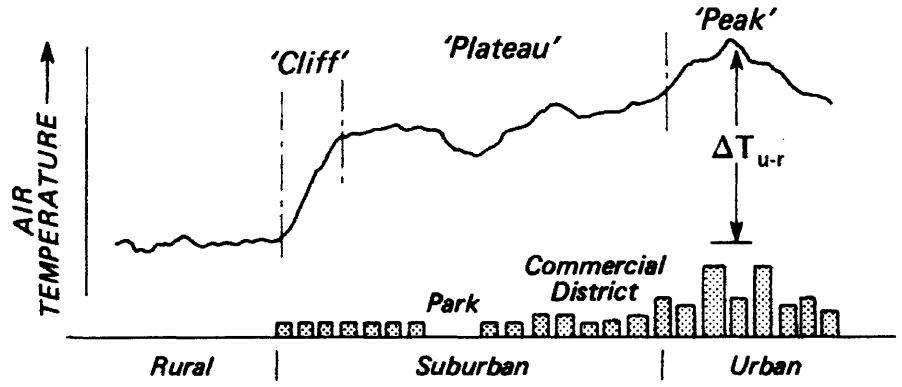

Figure 1.1. Generalized cross-section of a typical urban heat island (Oke 2002).

Meanwhile, most residents live in the urban areas, and urban heating can also have an impact on indoor air temperature and human thermal comfort, which inherently correlate to building energy consumption. Fresh air is needed for the indoor environment, and it inevitably requires a certain amount of air exchanged with outdoor environment. Hot inlet air will mix with the air inside and

thus raise the overall temperature, which imposes higher cooling loads to achieve a comfortable indoor thermal condition, especially in hot seasons. And it results in larger operational energy consumption for the buildings. Fig 1.2 shows the energy flow map for the US in 2014, where building energy consumption (residential and commercial) accounts for over 40% of the total energy sink and heating and cooling loads takes up a large proportion (Ghoniem 2011). Facing the global warming effect largely caused by emissions of energy consumption by-products, CO_2, countries and cities are obligated to manage and reduce the building energy costs, thus achieving energy-efficient building communities.

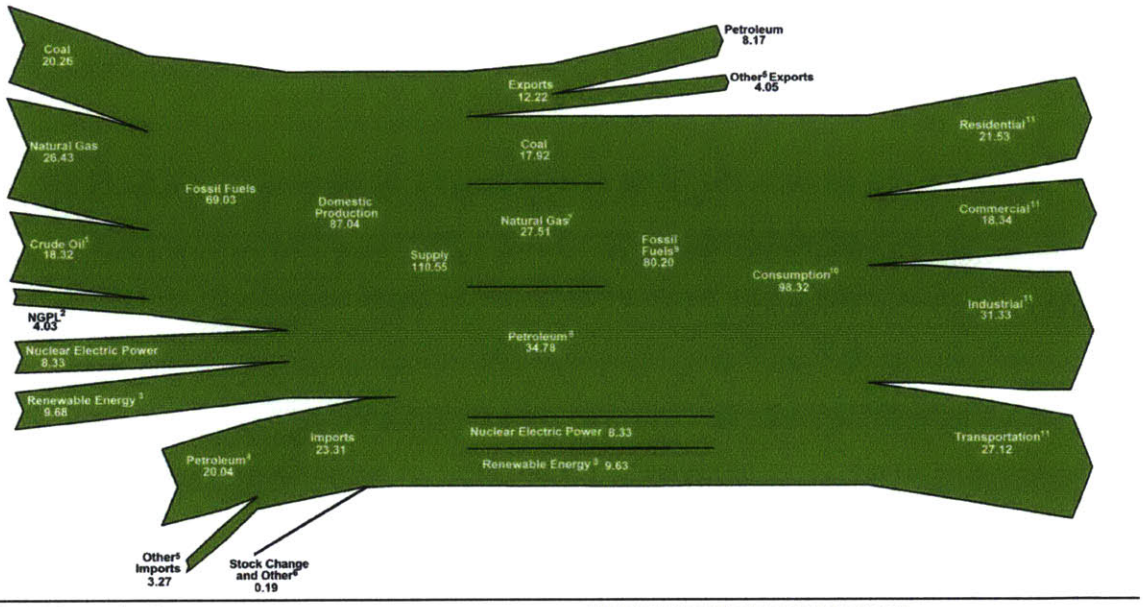

[1] Includes lease condensate.
[2] Natural gas plant liquids.
[3] Conventional hydroelectric power, biomass, geothermal, solar/photovoltaic, and wind.
[4] Crude oil and petroleum products. Includes imports into the Strategic Petroleum Reserve.
[5] Natural gas, coal, coal coke, biofuels, and electricity.
[6] Adjustments, losses, and unaccounted for.
[7] Natural gas only; excludes supplemental gaseous fuels.
[8] Petroleum products, including natural gas plant liquids, and crude oil burned as fuel.
[9] Includes -0.02 quadrillion Btu of coal coke net imports.
[10] Includes 0.16 quadrillion Btu of electricity net imports.
[11] Total energy consumption, which is the sum of primary energy consumption, electricity retail sales, and electrical system energy losses. Losses are allocated to the end-use sectors in proportion to each sector's share of total electricity retail sales. See Note 1, "Electrical Systems Energy Losses," at the end of U.S. Energy Information Administration, *Monthly Energy Review* (March 2015), Section 2.

Notes: • Data are preliminary. • Values are derived from source data prior to rounding for publication. • Totals may not equal sum of components due to independent rounding.

Sources: U.S. Energy Information Administration, *Monthly Energy Review* (March 2015), Tables 1.1, 1.2, 1.3, 1.4a, 1.4b, and 2.1.

Figure 1.2. Energy sources and consumption patterns in the US. (Adopted from the Energy Information Administration / Annual Energy Review 2014)

In order to construct a thermally comfortable and energy-efficient building community, we need to have a better understanding of the urban microclimate with characteristics such as wind, temperature, humidity etc. Analysis of the microclimate is mostly focused on urban canyons, the local outdoor areas surrounded by buildings where humans live and work. Urban canyons are

considered as a simplified miniature of many common urban landscapes and act as the connections between the indoor and outdoor environment.

1.2 Wind field modeling for urban canyons and their neighborhoods

1.2.1 Physical processes happening in urban canyons

Urban canyons, as shown in Fig 1.3, are typically comprised of high-rise buildings on the lateral sides and streets in between. In order to well understand the urban microclimate, we need to get an idea of the physical processes occurring in urban canyons.

One important aspect is the thermal process originated from the solar radiation. After reflection, scattering and absorption by clouds and other atmospheric constituents, the remainder of the shortwave solar heat flux will irradiate the surfaces that sky can directly see, mostly on the building roofs and the upper part of the walls and sometimes on the road when the building intervals are large. When the radiation contacts the surface, part of it will be absorbed into the building materials, and another gets reflected. Due to the larger density in urban areas, the building façades are quite close to each other, and the reflection between the neighboring walls will trap a lot of heat in the canyons. At the same time, the large amount of thermal mass will also emit the previously absorbed heat to the canyons and the outer atmosphere in the form of long-wave radiation. Convective heat transfer can happen when there is wind in the region. Conduction takes place along different layers of the building blocks and ground when temperature gradients exist. Human activities and transportation emit anthropogenic heat to the urban canyons, which is also an ineligible contributor to the urban heating. Trees and plants, however, can take in the heat trapped in the canyons and use their evaporation system to reduce the heating effect.

Another important phenomenon is the mechanical process mainly driven by the wind. As is shown in Fig 1.3, at high levels, the wind field is not affected by the massing and retains the same speed and direction from upstream. However, when it gets close to the building height level, the shear layer on the building top deflects the upstream wind and creates circulation and turbulent mixing within the urban canyons. Wind can help facilitate the convective heat transfer

process and flush out the heat concentrated in the canyons as well as pollutants emitted by the human beings. In addition, pressure differences on the opposite sides of the building façades will push the wind across the openings, which will meet the cooling requirement by natural ventilation.

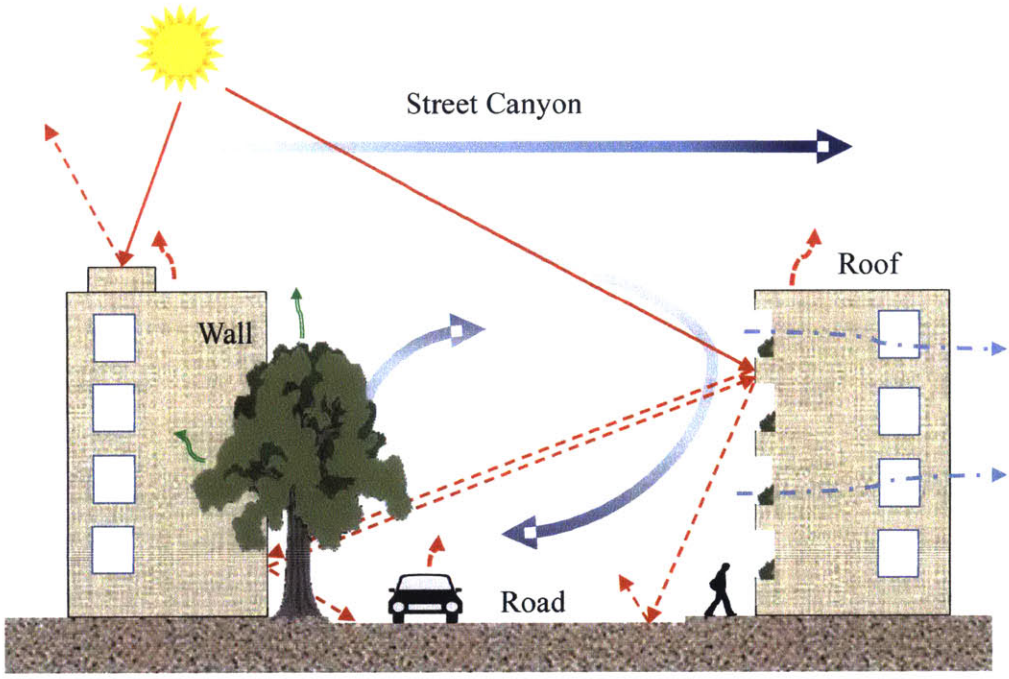

Figure 1.3. Sketch of thermal and mechanical processes in urban canyon areas. Red arrows refer to possible heat transfer approaches (solid line as short wave radiation and broken line as long wave radiation); and blue cycles refer to turbulence generated in street canyons.

To evaluate the microclimate in urban canyon areas, we should take a careful look at the wind fields as they play a significant role in the thermal and mechanical processes happening in the region. The wind field connects the transport of air momentum and heat, and determines the magnitude of convective heat transfer process. It also acts as an important factor in evaluation of outdoor thermal comfort (ASHRAE 2013). Furthermore, the wind field greatly affects the natural ventilation process, since this passive building system depends largely on wind-driven and buoyancy-driven flows. In addition, the wind field mainly determines the pollutant dispersion behavior, which in turn, would influence the indoor energy consumption, i.e. the choice of natural cooling or mechanical cooling systems. In order to guarantee the indoor air quality and

keep healthy, residents will be reluctant to open the windows and let outdoor air circulating across the room to remove the heat if it is highly polluted outside. All in all, studies for wind fields in urban canyons are helpful for predictions of urban microclimate and building energy analysis.

1.2.2 Building morphology in urban canyons and their neighborhoods

Building morphology determines the characteristics of the urban canyons, and it is one of the most important impact factors for the wind field in urban areas. Parameterization of building morphology contributes to a qualitative description of the massing and its interactions with wind environment. Fig 1.4 gives a sketch of a building community as well as the geometric parameters and we can then define the building morphometric parameters based on the geometry marked in the figure. Note that although drawn as building-like, the element is generic, representing all obstacles relevant to airflow. Similarly, the concept is not limited to a grid array. It could include scattered trees, differently shaped houses, and winding streets that are more typical of real cities (Grimmond and Oke 1999).

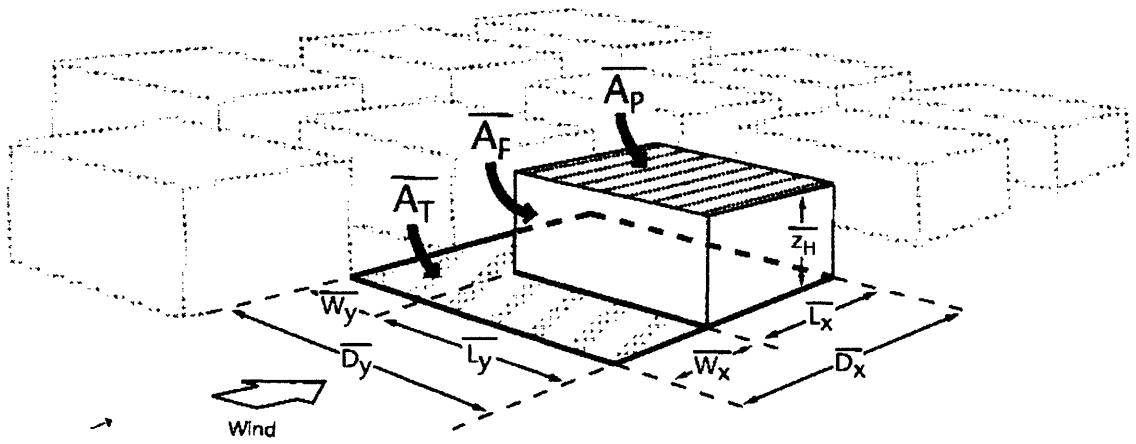

Figure 1.4. Definition of building morphometric parameters (Grimmond and Oke 1999).

The characteristic length of an urban canyon is the area-average building height, which sums up the total volume of the massing in the community and averages over the total horizontal area.

$$h = \sum_i \overline{A_{p,i}} \overline{z_{H,i}} \Big/ \sum_i \overline{A_{p,i}} \tag{1.1}$$

Where the overbar of the geometric parameters means that the value is averaged over local roughness and the following expressions will not include them for simplicity. A_p refers to the plan area or projected area of the building in the horizontal plane and z_H refers to the height of the building.

The following three non-dimensional morphological parameters describe the density of the building community in different perspectives. The first parameter, the plan area density λ_p, describes the massing density in the horizontal plane, and it is defined as the ratio of plan area A_p to the total lot area A_T of the building community.

$$\lambda_p = A_p / A_T = L_x L_y / D_x D_y \tag{1.2}$$

In contrast, the frontal area density λ_f describes the massing density in the vertical plane, and it is defined as the ratio of frontal area A_f to the total lot area A_T of the building community. Note that the frontal plane refers to the projected vertical area orthogonal to upwind direction.

$$\lambda_f = A_f / A_T = z_H L_y / D_x D_y \tag{1.3}$$

Note that both these two density parameters can be extended to the overall average property of the building community if the numerator and denominator are sums of the all the buildings.

The last parameter, aspect ratio λ_r, describes the density of the urban array, and it is defined as the ratio of building height z_H to the width of the streets w in between two neighboring buildings.

$$\lambda_r = z_H / w_{x,y} \tag{1.4}$$

Note that the canyon aspect ratio can be extended to the overall average property of the building community if both numerator and denominator refer to the area-average property of the entire area as similarly defined in Equation (1.1).

1.2.3 Typical approaches in wind field modeling field

There are two prevailing approaches to obtaining a reasonable prediction of wind fields in urban canyons.

One possible method is to use conventional Computational Fluid Dynamics (CFD) tools to calculate dynamic wind flow patterns. These advanced CFD models, based on the continuum hypothesis, solve coupled non-linear Partial Differential Equations (PDEs) with respect to mass, momentum and energy conservation. Detailed turbulence models, e.g. Reynolds-Averaged Navier-Stokes (RANS) equations, Large-Eddy Simulation (LES), etc., are used in the atmospheric turbulence simulation and these models are embedded in many commercial CFD tools, e.g. Fluent, CFX, etc. Although researchers agree on the fact that they can present details on non-uniform facet heat exchange processes and turbulence patterns in canyon areas, the computational costs of these advanced CFD tools are not trivial and needed further consideration in designers' work. Obviously, for instance, designers cannot tolerate waiting a couple of hours in front of computers to see the wind modeling results by a simple shift of building blocks to a certain direction or a small change in building geometries. Besides, these CFD tools are commonly not open source software, and designers also pay a large amount of money for the license of commercial tools, which increases the simulation cost and thus makes CFD analysis hard to apply widely in building design optimization.

The other approach is to use data assimilation methods to correlate wind-field parameters, like the velocity ratio, defined as the ratio of local velocity to a reference velocity, with building geometries, e.g. the planned and the frontal building areas. But the result is very site-specific, and the method requires a large amount of experimental data for the correlation, which increases the overall cost of purchase, installation, operation and maintenance of those measuring tools. What's more, the result is only limited to spatial-average values and takes in little consideration of local turbulence effect in urban canyons. So it is not accurate enough for designers' use in

wind-field modeling, especially at neighborhood scales, where the domain size is relatively small and needs detailed local information of wind field results.

Within a tradeoff of accuracy, computational efficiency and financial costs, the Lattice-Boltzmann Method (LBM) shows its prospective potential by its parallelism and open-source nature (Chen et al. 1998), which are welcome to the workflow of building design. Details of LBM are further explained in Chapter 2.

1.3 Current designer workflow in building simulation

Although wind field simulation by conventional CFD tools is usually expensive and time-consuming, most of the design projects still refer to those results for design optimization because of their wide use and acceptable accuracy. Fig 1.4 shows the current workflow for wind field analysis by conventional CFD tools. It starts from the initial building design from designers, when a pool of CAD-related software is utilized, e.g. Rhino, AutoCAD, etc. To run the wind field simulation, designers must consult building simulation engineers with CAD files exported for the design geometry. But in most cases, the design output contains relatively complex geometries not compatible with CFD software, and engineers must simplify the geometry first. Then discretization is performed for numerical scheme to operate on, with the help of the third commercial mesh-maker software. After setting up the grids, the coupled Navier-Stokes (NS) and energy solver is used and the numerical results are typically routed to a post-possessor to exhibit the wind field map. After that, results are interpreted by engineers and returned to designers for reference. If designers have some further modifications on the design product, another iteration is processed and so on, until the results are satisfactory for the building design.

Looking at the current workflow, we notice that there are many transitions among different commercial software, from the design tool to the simulation solver and from pre-possessors to post-possessors. On the one hand, designers must collaborate a lot with engineers and pay for the simulation results. On the other hand, engineers must master the use of all these commercial CFD tools, and beforehand reconstruct a simplified geometric model for simulation if necessary.

A lot of time and money is expended in the transitions, which acts in opposition to the necessity of wind field analysis.

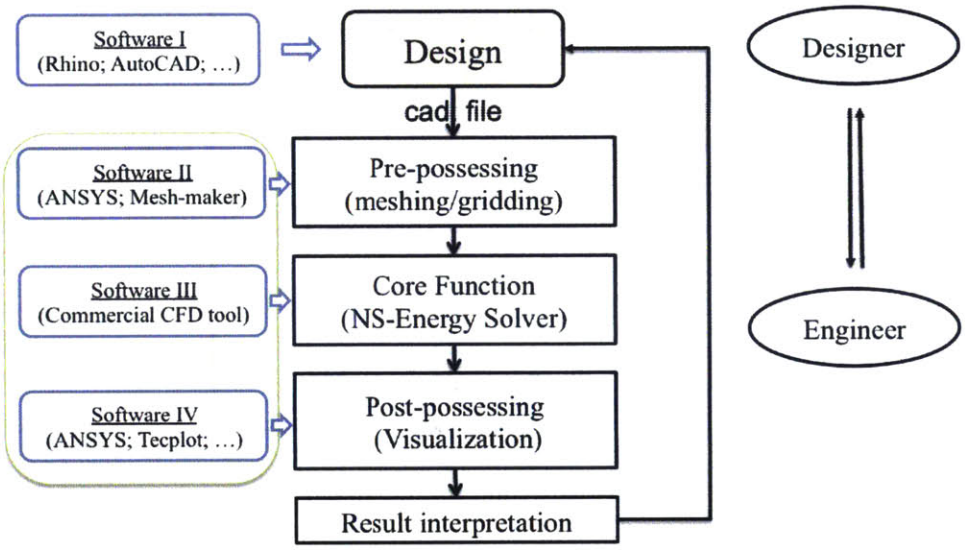

Figure 1.5. Current designer workflow for wind field analysis.

1.4 The objective of the research

The objective of the research is to develop the Lattice-Boltzmann Wind Field Model (LBWFM) to simplify the workflow of the wind field analysis. The most important improvement of LBWFM compared with conventional CFD tools is that it is entirely compatible with Rhino-based environment for designers, using the visual scripting language integrated with Rhino software, Grasshopper, to connect building design and wind field modeling. The model is open source, and well packaged with designer-relevant inputs and outputs, so designers can directly operate on the modeling platform themselves according to their needs. At the same time, the LBWFM is aimed to achieve fast and relatively accurate results, which makes it possible for designers to get feedback from the wind field in a shorter time. Engineers act as the backup force to manage and modify the LBWFM according to designers' requirements, and supply technical support for the proper use and result interpretation. The fast response of the wind field analysis can then appeal to designers and attract more design projects to assess the wind field as well as its applications, e.g. outdoor thermal comfort, natural ventilation potential, etc., in order to achieve thermally-comfortable and energy-efficient building communities.

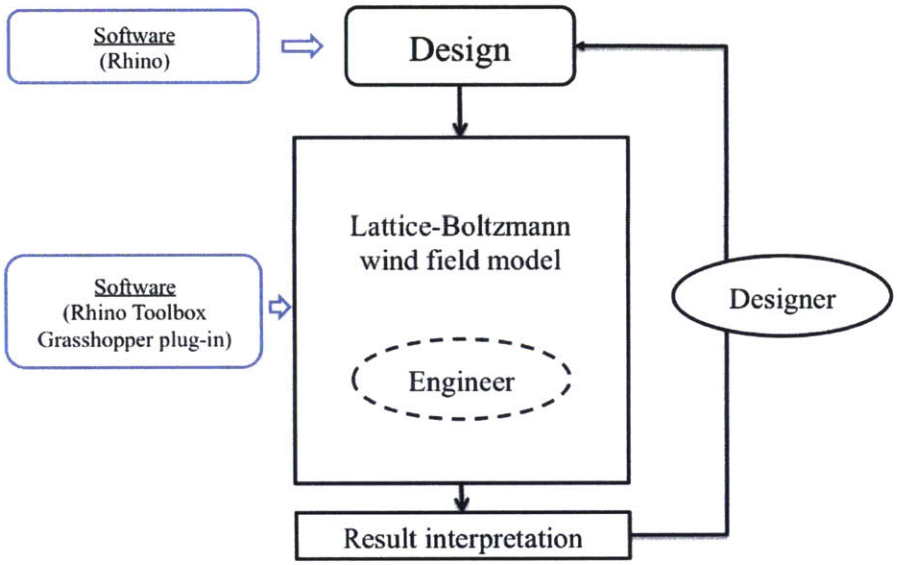

Figure 1.6. Improved designer workflow for wind field analysis.

LBWFM is based on the development of Lattice-Boltzmann Method (LBM) in the early nineties of the last century. Chen and Doolen (1998) reviewed the fundamentals of LBM and its applications in single-phase and multi-phase simulations, e.g. simple cavity flows, turbulence, multicomponent flow through porous media and particle dispersion in fluid flows. And they showed the numerical results of LBM modeling with superior computational efficiency compared to conventional CFD methods. In the early age of applications as shown in the paper, most of the application examples focused in two-dimensional flows with simple geometries, and three-dimensional case studies with irregular boundaries only come out in recent years. Chen et al. (2003) studied the turbulence modeling of LBM by implementing k-ε model, and proved its accuracy and enhanced efficiency in modeling airflow past a moving car. Yu et al. (2006) invented a multi-block method to improve the efficiency of LBM, but the complexity is added in computing multiple distribution functions with non-uniform gridding, thus counteracting with the efficiency obtained from the smaller number of grids. However, there's little research on three-dimensional urban airflow modeling until recent days when supercomputer shows up and cloud computing becomes possible. Research on implementing Large-Eddy Simulation (LES) model onto LBM turbulence modeling is applied, as Obrecht et al. (2015) coded LBM solver for urban airflow on Graphic Processing Units (GPUs), and validated with flow around a wall-

mounted cube. Onodera et al. (2013) also conducted a large-scale LES-LBM simulation on GPUs for wind field in Tokyo, and improved the efficiency by 30% compared to normal computers. In terms of designer-relevant focus, availability of supercomputers or GPUs computing for designers is still under discussion as it is used simply for wind field analysis, and increase in the capital costs should be well balanced for the improved accuracy in LES model and efficiency for modeling.

In the following chapters, a traditional Single-Relaxation-Time LBM model is developed and tested with experimental data and conventional CFD tools for urban airflow simulation with simple building geometries, and LBWFM is then constructed by proper settings of inlet wind profile and numerical modeling domain to achieve a fast and relatively accurate wind field solver, followed by its integration into the designer workflow. LBWFM is also extended in the analysis of natural ventilation potential in Chapter 6. Finally the limitation of LBWFM is stated, and feasible improvements on buoyancy flow simulation are explained in the future work.

Chapter 2

Principles of Lattice-Boltzmann Method

2.1 Introduction

Lattice-Boltzmann Method originates from the Lattice Gas Automaton (LGA) proposed in 1986. The LGA method solves for the transport problems (e.g. fluid flow, heat transfer, etc.) and constructs the world in a discrete lattice space where molecular particles on the lattice site conserve mass, momentum and kinetic energy. At each site, there are two states for particles (at the site or not) noted as Boolean variables $n_i(\mathbf{x},t)$, i = 1, 2, ..., M, where M is the number of directions of the particle velocities. The kinetic equation is borrowed from statistical mechanics and expressed as follows,

$$n_i(\mathbf{x}+\mathbf{e}_i,t+1)=n_i(\mathbf{x},t)+\Omega_i(n(\mathbf{x},t)) \tag{2.1}$$

where $\mathbf{e}_i$ are the local particle velocities, and in the expression give the displacement of particles from time t to t+1. The two terms on the right-hand side elaborate the two basic mechanisms in the evolution process: streaming and collision. The two terms altogether represent the current status of each particle in the lattice and directly propagate to the neighbor node in the direction of its velocity; the second term Ω_i denotes the local collision operator that determines the interactive behaviors of particles at the same lattice with different velocity directions. However, the lattice gas automata suffer from statistical noise in real applications due to the use of the Boolean variables, as well as the large computational cost required by the microscopic nature of the scheme.

The Lattice-Boltzmann Method (LBM) then arises to resolve the deficiencies of the LGA in the simulation process. Statistically-averaged functions replace the previous Boolean variables, as in

Equation (2.1) $f_i = \langle n_i \rangle$ (where $\langle\ \rangle$ represents ensemble average values), and collective behaviors of particles on a single lattice site are investigated instead of individual particle motions. This procedure eliminates the statistical noise in the lattice gas automata. Another important modification of the LGA, made by Higuera & Jiménez (1989), is the linearization of the collision operator by local equilibrium state approximation, which further enhances the computational efficiency for the scheme.

As we could generalize for the universal approaches to solving the transport equations, macroscopic and microscopic views are the two most popular choices. For the macroscopic approach, often called Computational Fluid Dynamics (CFD) simulation, the continuum hypothesis has to be presumed and the nonlinear Navier-Stokes equations are evaluated. To close the solving system, constitutive equations are also included. Different discretization methods need to be implemented and boundary conditions also must be neatly described. In most cases, the algebraic equations have to be solved iteratively until the convergence criteria are reached. Many physical and numerical approximations are made in the problem-solving process, especially for turbulence or other irregular transport patterns. For the microscopic approach, called Molecular Dynamics (MD) simulation, individual particles are well considered, and their local interactions are described as collisions. The nonlinear Partial Differential Equations (PDEs) for solving in macroscopic approach are replaced by simpler ordinary differential equations of momentum conservation (i.e. Newton's second law). Although it is more intuitive, there's also a big problem of memory and storage for numerical solvers. The total number of equations for a single time step is of the same magnitude as the number of molecules of substances, which is really a tremendous burden for the current computers. And it is not even enough because we have to sum up the time range. To make the numerical scheme catch up to the physical process and record the changes of quantities, the numerical time step has to be less than the transient collision time scale, and it leads to the truth that the work to be done might go beyond the capability of the available computers.

The LBM is invented just at the middle of the two scales. It views the whole world in a mesoscopic scale, where individual particle behaviors are analyzed but further collectively integrated in a statistical manner (Fig 2.1). Kinetic equations are solved for the averaged

macroscopic properties, where mass, momentum and kinetic energy are conserved. So the LBM inherits the molecular transport mechanisms, and resolves the tedious work of calculations and storage by summing up to the ensemble properties. These characteristics help achieve the efficiency and relative accuracy of the numerical scheme.

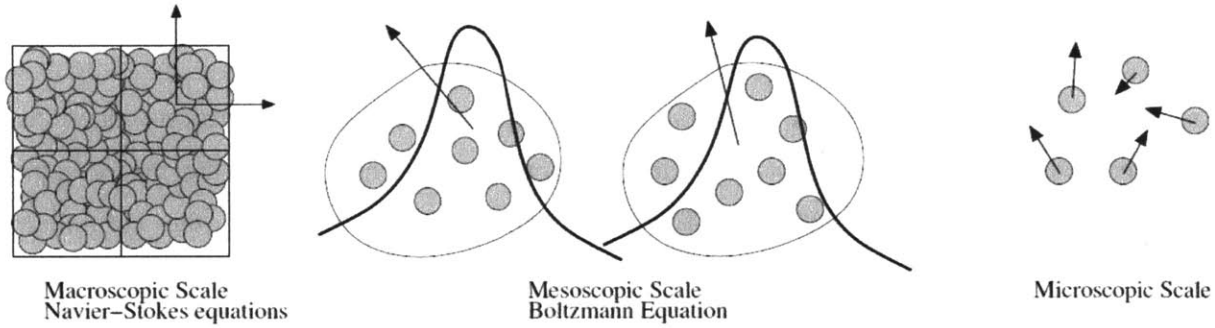

Figure 2.1. Schematic of different approaches to transport problems.

2.2 Governing equation

As we have mention above, the LBM is directly derived from the LGA by simply replacing the Boolean variable with a distribution function f_i, and thus the discrete kinetic equation evolves into the following form (Chen et al. 1998, Mohamad 2011).

$$f_i\left(\mathbf{x}+\mathbf{e}_i\Delta t, t+\Delta t\right)=f_i\left(\mathbf{x},t\right)+\Omega_i\left(f\left(\mathbf{x},t\right)\right) \tag{2.2}$$

where f_i refers to the distribution function for the particle along the i^{th} direction; Ω_i refers to the collision operator which denotes the rate of change of f_i due to the collision process. If it is written in a continuum form, the equation will be rearranged as follows, known as the Boltzmann equation.

$$\frac{\partial f_i}{\partial t}+\nabla\left(f_i\mathbf{e}_i\right)=\Omega_i \tag{2.3}$$

Note that it is achieved by approximating both the lattice spacing Δx and the time interval Δt as small parameters of ε and by truncating the second-order term. No external forces are exerted on the system.

Now we should have a close investigation of the distribution function that is oriented in statistical mechanics, and correlates to the macroscopic properties of most interest. Since the stochastic process of collision is really hard to describe, we prefer to find an equilibrium state when the distribution function is independent of directions. It could be achieved after a certain time period because the description of collision process is inherently assumed to distribute all the particles as the same state with the statistical average. From knowledge of molecular kinetics, the Maxwell-Boltzmann distribution equation could be then derived. As we define the equilibrium state, the equilibrium distribution function can be then expressed as,

$$f^{eq} = \prod_{i}^{M} f_i(\mathbf{e}_i) \tag{2.4}$$

The summation of the distribution function for all possible states should be defined as unity.

$$\int f^{eq} d\mathbf{e} = 1 \tag{2.5}$$

Then we can arrive at the expression of equilibrium distribution function by introducing the Maxwell-Boltzmann distribution function (Chen et al. 1998, Mohamad 2011).

$$f^{eq} = \frac{\rho}{(2\pi RT)^{M/2}} \exp\left[-\frac{(\mathbf{e}-\mathbf{u})^2}{2RT}\right] \tag{2.6}$$

where ρ, $\mathbf{u}$ are macroscopic fluid density and velocity, respectively; R is the Boltzmann constant; T is temperature; M is the degree of freedom. To make it convenient for calculation, we use a Taylor expansion on $\mathbf{u}$ and approximate to the second-order ($\mathbf{u}^2$), so that it is the same order of accuracy with the Navier-Stokes equation.

$$f^{eq} = \frac{\rho}{(2\pi RT)^{M/2}} \exp\left(-\frac{\mathbf{e}^2}{2RT}\right) \cdot \left[1 + \frac{(\mathbf{e}\cdot\mathbf{u})}{RT} + \frac{(\mathbf{e}\cdot\mathbf{u})^2}{2(RT)^2} - \frac{\mathbf{u}^2}{2RT}\right] + o(\mathbf{u}^3) \tag{2.7}$$

As we can see from the expressions above, the distribution function is closely related to the macroscopic quantities. By definition, f_i could be viewed as the generalization of macroscopic density,

$$\rho = \sum_i f_i \tag{2.8}$$

Similarly, we can derive correlations of macroscopic momentum, energy, etc. with the distribution function f_i and particle velocity $\mathbf{e}_i$. For example, the macroscopic momentum is expressed as,

$$\rho\mathbf{u} = \sum_i f_i \mathbf{e}_i \tag{2.9}$$

For an incompressible fluid, the macroscopic density is constant in time and we often assume it as a lattice density ρ_0 and normalize it as unity, so as to keep up with definition of distribution function. Thus, the macroscopic velocity $\mathbf{u}$ can be derived from Equation (2.8) as,

$$\mathbf{u} = \sum_i f_i \mathbf{e}_i \tag{2.10}$$

At the equilibrium state, all the equations from (2.7) to (2.9) will obviously be also satisfied.

$$\begin{aligned} \rho^{eq} &= \sum_i f_i^{eq} = 1 \\ \mathbf{u}^{eq} &= \sum_i f_i^{eq} \mathbf{e}_i \\ e^{eq} &= \frac{1}{2}\sum_i f_i^{eq} (\mathbf{e}_i - \mathbf{u})^2 \end{aligned} \tag{2.11}$$

where e is the internal energy, and according to kinetic theory, $e = MRT/2$.

We could then further simplify the Equation (2.6) by (2.10) into the following form.

$$f_i^{eq} = \rho w_i \left(1 + \frac{(\mathbf{e}\cdot\mathbf{u})}{c_s^2} + \frac{(\mathbf{e}\cdot\mathbf{u})^2}{2c_s^4} - \frac{\mathbf{u}^2}{2c_s^2} \right) \tag{2.12}$$

where w_i is called weight factor, which is determined by lattice arrangements of the domain; c_s is called the lattice sound speed which is derived from kinetic theory by approximating infinite degrees of freedom (i.e. $M \to \infty$).

$$c_s = \sqrt{\gamma RT} = \sqrt{\left(1 + \frac{2}{M}\right) RT} \simeq \sqrt{RT} \tag{2.13}$$

where $\gamma = c_p / c_v = 1 + (2/M)$ is a ratio of specific heat.

In real cases, a velocity vector always consists of three components, and thus we define the magnitude of the lattice sound speed as $c = \sqrt{3c_s^2} = \sqrt{3RT}$. To achieve a dimensionless form of the governing equation, we normally set the value of c as unity in the calculation, and normalize both the particle velocity **e** and fluid velocity **u** by c. Then Equation (2.12) will be rewritten as follows.

$$f_i^{eq} = \rho w_i \left(1 + 3(\mathbf{e}\cdot\mathbf{u}) + \frac{9}{2}(\mathbf{e}\cdot\mathbf{u})^2 - \frac{3}{2}\mathbf{u}^2 \right) \tag{2.14}$$

When we need to evaluate the equilibrium distribution functions, we have to first determine the lattice arrangements of the modeling domain. Typically for a two-dimensional (2D) or three-

dimensional (3D) problem, for example, we could set up the linkage of neighboring lattices as depicted in Fig 2.2.

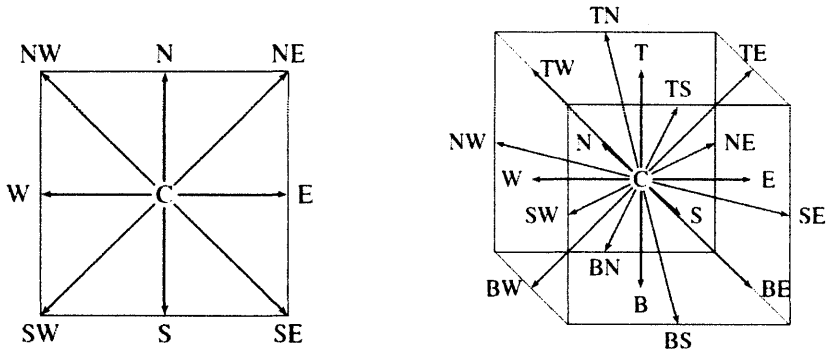

(a) D2Q9 (b) D3Q19

Figure 2.2. Schematics of the lattice arrangements in 2D or 3D cases.

Note that commonly for the notations of the lattice arrangements in the LBM, a terminology is often used as D*n*Q*m*, where *n* refers to the dimension of the problem (*n* = 1 for 1D problem; *n* = 2 for 2D; and *n* = 3 for 3D) and *m* refers to the degrees of freedom for particle velocities (same as *M*).

For the D2Q9 model, each lattice (denoted as center C in Fig 2.2 (a)) is closely connected with 8 neighbors and the whole system is categorized into 3 parts: centered lattice itself (C), orthogonal sublattices (N, E, S, W) as well as diagonal sublattices (NE, SE, SW, NW). To obtain the weight function w_i, He & Luo (1997) use a third-order Hermite formula to approximate the summation in Equation (2.11). Abe (1997) assumes w_i has a simple truncated functional form based on $\mathbf{e}_i$. And both reach the same results as follows.

$$\begin{cases} w_i = 4/9 & \mathbf{e}_i = (0,0) & i \in \{\mathrm{C}\} \\ w_i = 1/9 & \mathbf{e}_i = (0,\pm 1) & i \in \{\mathrm{N,E,S,W}\} \\ w_i = 1/36 & \mathbf{e}_i = (\pm 1,\pm 1) & i \in \{\mathrm{NE,SE,SW,NW}\} \end{cases} \tag{2.15}$$

For the D3Q19 model, each lattice (denoted as center C in Fig 2.2 (b)) is closely related to 18 neighbors and the whole system is also categorized into three parts: centered lattice itself (C),

primitive sublattices (N, E, S, W, T, B) with a distance of one lattice interval to the centered node, as well as secondary sublattices (NE, SE, SW, NW, TN, TE, TS, TW, BN, BE, BS, BW) which are nearly one half of the lattice intervals away from the center. Weight function values can also be derived by the same methods mentioned above.

$$\begin{cases} w_i = 1/3 & \mathbf{e}_i = (0,0,0) & i \in \{\mathrm{C}\} \\ w_i = 1/18 & \mathbf{e}_i = (\pm 1,0,0),(\pm 1,0,0),(\pm 1,0,0) & i \in \{\mathrm{N,E,S,W,T,B}\} \\ w_i = 1/36 & \mathbf{e}_i = (\pm 1,\pm 1,0),(\pm 1,0,\pm 1),(0,\pm 1,\pm 1) & i \in \{\mathrm{NE,SE,SW,NW,TN,TE} \\ & & \mathrm{TS,TW,BN,BE,BS,BW}\} \end{cases} \tag{2.16}$$

Since the collision operator closely relates to the distribution function and we know the function values at the equilibrium state, we can then use a Chapman-Enskog expansion on the collision term and approximate it with the local equilibrium distribution function values to second-order accuracy.

$$\Omega_i(f_i) = \Omega_i(f_i^{eq}) + \varepsilon \frac{\partial \Omega_i}{\partial f_i}(f_i - f_i^{eq}) + o(\varepsilon^2) \tag{2.17}$$

As we have known from the definition that collision process cannot happen at the equilibrium state, we have: $\Omega_i(f_i^{eq}) = 0$. Then we will arrive at a linearized collision operator, and Bhatnagar, Gross and Krook (need date), as well as Welander (1954) both introduced a simplified model for that. The collision operator is replaced as,

$$\Omega_i = \frac{1}{\tau}(f_i^{eq} - f_i) \tag{2.18}$$

where τ is denoted as the relaxation factor, referring to the rate at which the local particle distribution approaches an equilibrium state.

From the expression above, we notice that the collision operator also obeys the conservation laws for macroscopic properties. This can be easily proved if we plug Equation (2.8) - (2.11) into (2.18), and sum up the total N lattice nodes.

$$\sum_N \sum \Omega_i = 0, \quad \sum_N \sum_i \Omega_i \mathbf{e}_i = 0 \tag{2.19}$$

The Boltzmann equation (2.3) can be then rewritten in either a continuum or a discrete form.

$$\frac{\partial f_i}{\partial t} + \nabla (f_i \mathbf{e}_i) = \frac{1}{\tau}\left(f_i^{eq} - f_i\right) \tag{2.20}$$

$$f_i(\mathbf{x} + \mathbf{e}_i \Delta t, t + \Delta t) - f_i(\mathbf{x}, t) = \frac{1}{\tau}\left(f_i^{eq} - f_i\right) \tag{2.21}$$

To relate the relaxation factor to macroscopic properties, we can multiply Equation (2.20) with zeroth order or first order of particle velocity **u**, and then sum them up in all possible directions, which coincide with the continuum mass and momentum conservation equations listed below for an incompressible fluid.

$$\frac{\partial \rho}{\partial t} + \nabla(\rho \mathbf{u}) = 0 \tag{2.22}$$

$$\frac{\partial(\rho \mathbf{u})}{\partial t} + \nabla(\rho \mathbf{u}\mathbf{u}) = -\nabla p + \nu \nabla^2 \mathbf{u} \tag{2.23}$$

The pressure term in LBM can be obtained from the Equation of State (EOS) $p = \rho RT$.

$$p = c_s^2 \rho = \rho / 3 \tag{2.24}$$

When we compare with the incompressible Navier-Stokes equation, the relaxation factor can then be correlated with the normalized macroscopic kinematic viscosity ν in the form.

$$\tau = 3\nu + 0.5 \tag{2.25}$$

Similarly we can extend the correlation to the energy equation, where the relaxation factor depends on thermal diffusivity α.

$$\tau = 3\alpha + 0.5 \tag{2.26}$$

To obtain a higher-order accuracy scheme for the collision operator, the Multi-Relaxation-Time (MRT) model has been proposed. For example, Ginzburg (2005) invented the Two-Relaxation-Time (TRT) model, which splits the distribution function into a symmetric and an asymmetric part. Different values of relaxation factor are imposed on the two parts, thus enhancing the accuracy and improving the numerical stability of the overall results.

2.3 Boundary conditions

In the macroscopic approach, the setting of the boundary conditions is more like an intuitive process, because the continuum hypothesis helps to establish the no-slip (tangent velocity equal to zero) and no-flux (normal velocity conserved) conditions at the wall. But in the LBM, the boundary condition issue arises because the continuum framework does not have a counterpart. And many theories in the area of boundary conditions are proposed, of which the bounce-back mechanism stands out for its simplicity (Chen et al. 1998, Mohamad 2011).

The bounce-back mechanism, as is known from its name, mainly implies that an upstream particle moving towards the solid boundary will bounce back into the flow domain with conservation of mass and momentum. It is used to model solid stationary or moving boundary condition with no-slip velocity, and in application for most cases, solving the problem of flow over obstacles.

There are two different schemes to implement the bounce-back conditions depending on the lattice arrangements on the boundaries, and they have different orders of accuracy in approximation (as is shown in Fig 2.3). The first-order scheme suggests that lattice nodes could be directly placed on the boundaries, while the other suggests that the lattice nodes could be

placed so as to make the solid wall halfway between interior and boundary lattice nodes. Since the lattice spacing is normally uniform, by analogy to the finite difference scheme, we can achieve 2nd-order accuracy boundary conditions.

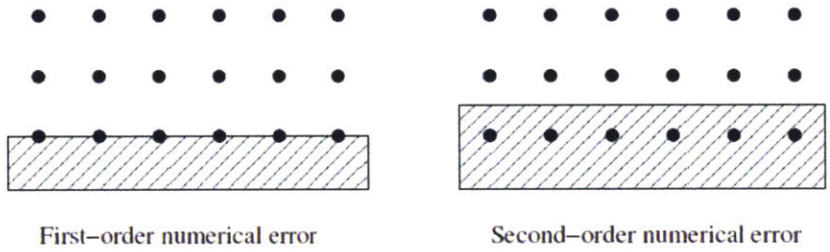

Figure 2.3. The two different schemes to implement bounce-back boundary conditions.

For the second scheme implemented in the D2Q9 framework, the process of bouncing back could be visualized as follows. Firstly, when the upstream particles carrying their lattice-averaged velocities move toward the wall, they will propagate their kinematic properties to the downstream 'virtual' particles residing in the boundaries (Fig 2.4 from (a) to (b)). But since the wall cannot sustain any fluid particles, it forces the mass moving backward to their origins with the same properties at the same orientations (Fig 2.4 from (c) to (d)). In the process, both mass and momentum are conserved.

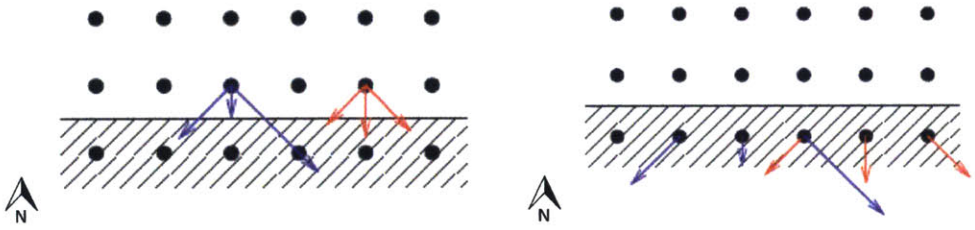

(*a*) Pre-streaming (*b*) Streaming

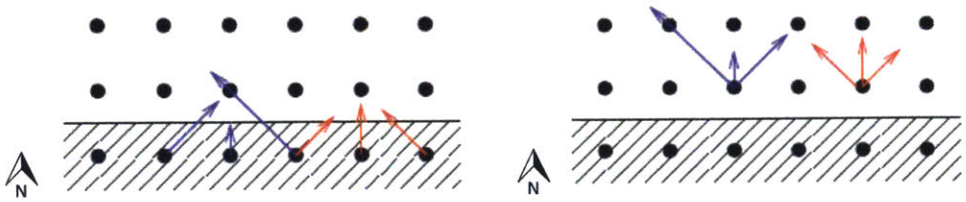

(*c*) bouncing-back (*d*) Post-streaming

Figure 2.4. Bounce-back process in determination of the second-order boundary conditions (Upwind direction is from north).

If we take the center node (i, j) with blue arrows in Fig 2.4 as an example to derive the mathematical expressions for the bounce-back scheme (i^{th} node along horizontal direction, j^{th} node along vertical direction, we have:

$$\begin{aligned} f_N(i,j) &= f_S(i,j) = f_S(i,j+1) \\ f_{NE}(i,j) &= f_{SW}(i,j) = f_{SW}(i+1,j+1) \\ f_{NW}(i,j) &= f_{SE}(i,j) = f_{SE}(i-1,j+1) \end{aligned} \tag{2.27}$$

The derivation of the bounce-back expressions for the D3Q19 from the D2Q9 relations is straightforward and the only difference between the two models is the number of counterparts that have to be set.

When the solid wall is no longer stationary, particles on the boundary should retain the same velocity with the moving solid, because fluid particles cannot sustain any of the shear stress on themselves. And then we can equate the moving boundary velocity $\mathbf{u}_{bc}$ with the macroscopic velocity of the boundary nodes $\mathbf{u}$.

$$\mathbf{u} = \sum_i f_i \mathbf{e}_i = \mathbf{u}_{bc} \tag{2.28}$$

In some problems, the outlet velocity is not known. To obtain a reasonable periphery boundary condition, a linear extrapolation scheme is often used for the unknown distribution functions on the boundary lattice nodes.

When we'd like to impose a periodic boundary condition, for example, the flow region is just repeating, we should set up the distribution function values on the left boundaries as the same with the function values on the right, shown in the figure below.

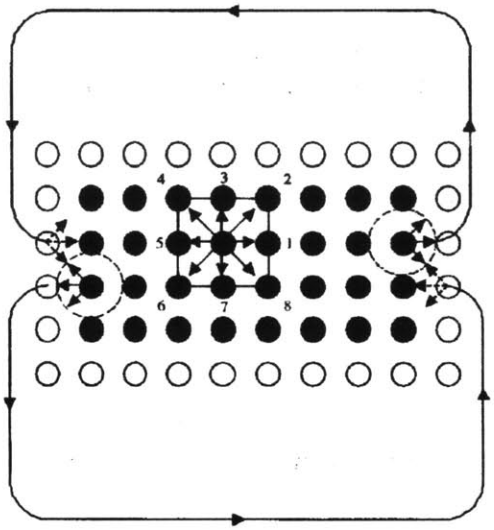

Figure 2.5. Schematic of periodic boundary conditions implemented by the LBM.

2.4 Numerical Stability

In a real case, for example, if fluid problems are to be solved, we need to set up numerical cases that are similar to physical ones. To achieve that, geometric, kinematic and dynamic similarity must be preserved so as to keep the main characteristics of the flow field. Generally, we will construct a dimensionless counterpart between physical and numerical situations, which is known as the famous Reynolds number (Re). In the physical world, it is more intuitive to find a characteristic length scale (L), known freestream velocity (u) and fluid kinematic viscosity (v) to express Re. And in the LBM, since density and sound speed are both normalized into the lattice form, we need to define the lattice velocity (U) and the lattice viscosity (ν) both in dimensionless form. Then a connection on Re is made between the two situations (Kundu et al. 1990, Mohamad 2011).

$$Re_{phy.} = Re_{num.}$$
$$\frac{uL}{\upsilon} = \frac{UN}{\nu} \tag{2.29}$$

Where N is the number of lattice nodes in the direction of the characteristic length.

During the derivation of the governing equation in the LBM, incompressibility of the fluid is presumed in the macroscopic world, and it should be preserved in the framework of the lattice world as well. The criterion for that is the range of Mach number (Ma), defined as the ratio of fluid velocity and sound speed, which is less than 0.3. For the counterpart in the LBM, values of the lattice velocity must be chosen within the same limits, as:

$$Ma = \frac{U}{c} < 0.3 \tag{2.30}$$

Since the lattice sound speed has been defined as the normalized value, the lattice velocity should not be larger than 0.3 to sustain the numerical stability. Typically, U is often set at the scale of 0.1~0.2 to reduce the round-off error.

Another constraint for the numerical stability comes from the setting of the relaxation factor, which is closely related to the macroscopic viscosity. As is shown in Equation (2.25), if the value of the relaxation factor is below 0.5, the macroscopic viscosity will be negative, which is unreasonable in a real case. And if it is just above but very close to 0.5, there will be also possibilities of obtaining instable solutions. So it is important to be really careful in choosing the value of that term, especially in high Re flow (turbulence). Considering the normal range of U and τ, the number lattice nodes will be very large, thus increasing the computational cost.

2.5 Concluding remarks

In recent years, the Lattice-Boltzmann method (LBM) has developed into an alternative and promising numerical scheme for simulating transport problems and modeling the physics in fluids (Chen et al. 1998). The scheme is particularly successful in fluid flow applications

involving complex boundaries, which is commonly seen in building simulation fields. Unlike the conventional CFD methods dealing with simplified NS equations and the MD method coping with individual particle behaviors, LBM is a hybrid, for its "duality" in between continuous and discrete natures. The discrete nature shows up in its construction of kinetic models where the fundamental physics of microscopic processes is well explained. LBM also has its continuous nature in that the principle focus is on macroscopic behavior described by statistically-averaged functions. The two natures are connected by the mesoscopic kinetic equations that enforce the macroscopic average properties derived out of LBM satisfy the desired macroscopic equations. The connections here are reliable at the basic premise that the macroscopic dynamics of a fluid is the result of the collective behavior of many microscopic particles in the system and that the macroscopic dynamics is not sensitive to the underlying details in microscopic physics (Kadanoff 1986).

The hybrid nature of the LBM introduces three important features that distinguish it from other numerical methods.

The most attractive characteristics lie in its computational efficiency. By focusing on averaged particle behaviors, LBM avoids solving the equation of motion for each particle as in MD simulations. By inheriting the advantages of a discrete kinetic model, including linear convection operator, easy implementation of boundary conditions, and fully parallel algorithms, LBM avoids solving nonlinear high-order PDEs and using discretization methods to achieve numerical solutions. Especially for its fully parallel nature, implementations of LBM solver on parallel computers are relatively easy, because particle motion is evaluated by neighboring nodes in the vicinity and can be decomposed locally over many processor cores, which largely enhances the efficiency of the numerical scheme. Furthermore, the LBM utilizes a minimal set of velocities in lattice space (Chen et al. 1998), and thus reduces the continuous Maxwell-Boltzmann equilibrium distribution into finite discrete moving directions, so that transformation from microscopic distribution functions to macroscopic quantities is greatly simplified into algebraic calculations.

Second, the pressure field is easier to obtain in the LBM compared with conventional CFD methods. In contrast, CFD methods deal with coupled equations (continuity equation and the equation of motion) to solve for the velocity and pressure field, which leads to numerical difficulties requiring decoupling and iterations. But in LBM, pressure field is calculated by the equation of state where macroscopic properties are pre-calculated with distribution functions.

Third, complex boundaries are easily implemented using bounce-back mechanism. No boundary equations (no flux and no slip on the boundaries) are required to solve as in conventional CFD methods, thus increasing the computational speed when a large amount of complex geometries are evident in the modeling domain.

Chapter 3

Validation of Lattice-Boltzmann method in wind field modeling

In the former chapter, the Lattice-Boltzmann Method is introduced to solve the transport problems and its advantages over other computational methods are explained, especially from the perspective of wind field modeling for urban canyons and their neighborhoods. In order to validate its merits in simulating wind fields in a fast and relative accurate manner, sample case studies are performed for the velocity and pressure fields, which are the two primary indicators of wind field. Comparisons will be made between LBM simulation results and experimental data (wind tunnel results) as well as CFD commercial tools (scSTREAM). LBM is coded in C#, which is source-friendly to a Rhino-based working environment and could be easily integrated in designers' workspace and post-possessed by Excel and Matlab tools.

3.1 Wind velocity field

3.1.1 Case description

A case study is conducted with a single building in the modeling domain (as is shown in Fig 3.1). The goal of this case study is to validate the LBM performance in calculating the wind velocity field with respect to the wind tunnel experiments constructed by the Architectural Institute of Japan (Shirasawa et al. 2003). In order to compare the results with experimental data, building size and wind field parameters are set to match the experimental settings, which are further explained as follows.

In the physical domain, a single building is located in the center of the domain, with a length of 50 mm, width of 200 mm and height of 200 mm. The upwind velocity distribution satisfies the power law along the vertical direction, which is the typical setting of inlet wind profile in ASHRAE Handbook of Fundamentals (ASHRAE 2013), with the maximum value of 7.84 m/s at

the top of the physical region (maximum height of 1000 mm), and wind speed is uniform in a horizontal plane. The expression of the wind velocity is shown as follows:

$$u(z) = 7.84(z/1000)^{1/4} \tag{3.1}$$

Where z is the height (unit: mm) and u is the wind velocity (m/s) at a certain height.

In the numerical domain of LBM, the building is centered in a cube of 2000 mm in both horizontal directions and 1000 mm in the vertical direction. To keep the dynamic similitude for the LBM model, Equation (2.28) is used to set up the gridding and relevant parameter values, and in the process, the numerical stability analyzed in Chapter 2.4 is also carefully considered. For example, to achieve the incompressibility of the fluid, the lattice velocity (U) on the top of the domain is set as 0.1, which represents the physical value of 7.84 m/s in the real world. In this case, after we calculate the Reynolds Number (Re), we will find that high Re flow takes place in the modeling region, and large numbers of the lattice nodes have to be set to ensure the numerical viscosity is within the safe range of stability. For instance, a uniform gridding is utilized with an interval of 12.5 mm, and thus there are 161 lattice nodes including periphery boundaries in both the x- and y-direction (defined in Fig 3.1), as well as 81 nodes in the z-direction. Roughly 2 million lattices are involved in the calculation.

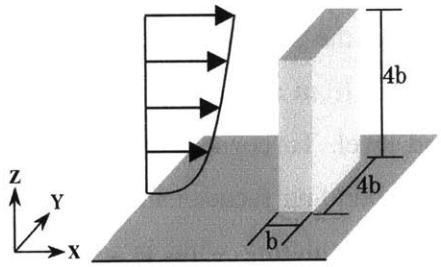

(a) Settings of wind velocity profile and building geometries

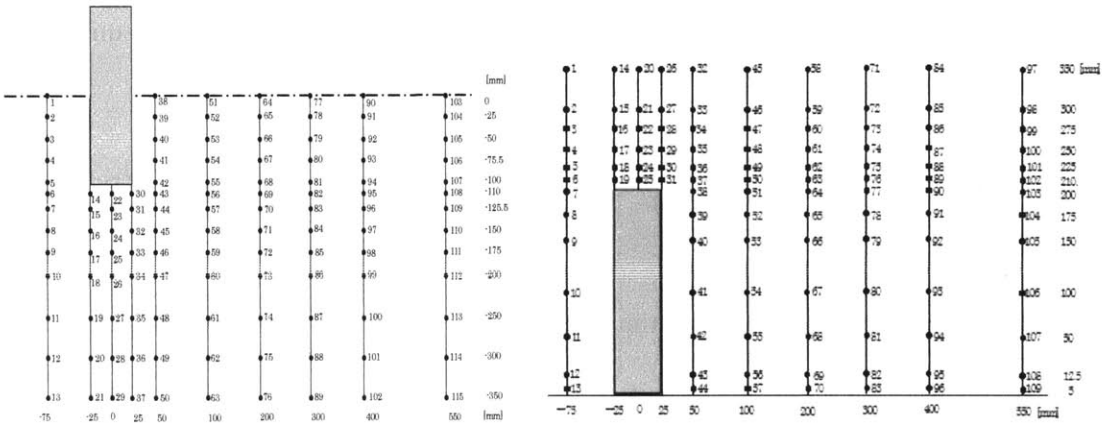

(*b*) Horizontal data point (*c*) Vertical data point

Figure 3.1. Schematic of wind-tunnel experiments and test point locations. (Shirasawa et al. 2003)

3.1.2 Results and Discussions

After running the LBM 3,000 times for the whole domain, we approximate the wind field as steady-state (particles reaching local equilibrium state). Results of the wind field are visualized both in horizontal and vertical planes. Note that for comparisons of wind-tunnel experiments, we pick out two specific cross sections for viewing: the horizontal plane at the height of 12.5 mm above the ground level (z = 12.5 mm), which is analogous to the human respiration zone, and the vertical plane at the centerline of the ground surface (y = 0).

Results on both planes clearly show the stagnation region near the building front (windward) façade. Recirculation flows happen in front of the stagnation region due to the retarding effect of the no-slip surface on the ground level. To conserve the mass balance, an acceleration zone is noticed both on lateral sides of the building façades and the building top. On the rear (leeward) side of the building, a vortex of recirculating wind is formed, which is the typical image of turbulent flows. At a first glimpse, the physical views of the LBM results add credits to the reliability of the simulation tool.

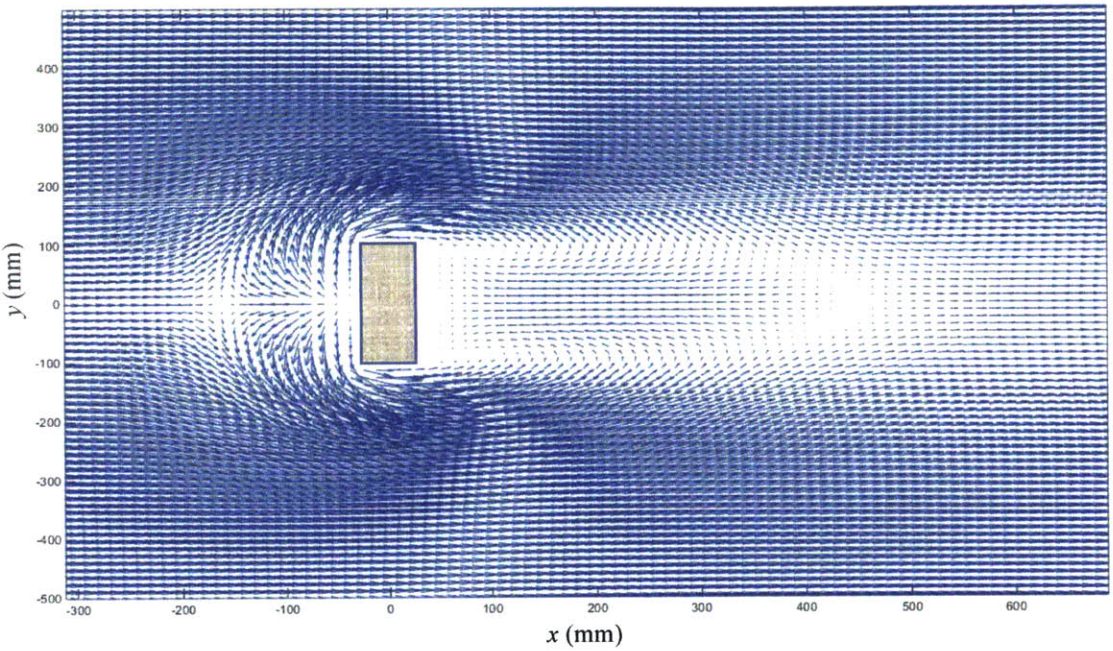

(a) Horizontal plane

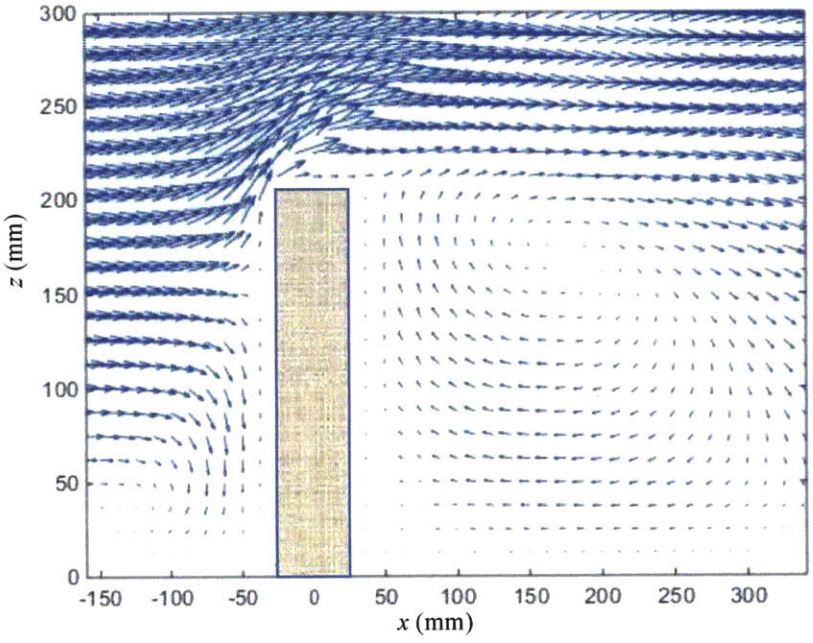

(*b*) Vertical plane

Figure 3.2. Vector velocity field in horizontal and vertical sections simulated by LBM.

3.1.3 Comparisons with wind-tunnel measurements

In addition to the exhibition of the wind vector field map, point-to-point comparisons have been also performed on the magnitude of the velocities between wind tunnel experiments and LBM simulation results.

Firstly, we select a representative position located at 100 mm downstream of the single building, and compare the values of the x-component velocity at a series of vertical test points (from point 45 to 57 in Fig 3.1 (c)). The result is given in Fig. 3.3. The red dashed line gives the ideal correlation that the two results coincide with each other, and the blue dotted line gives the real correlation calculated in the case. Numerical results fit well with the wind tunnel measurements: all the points are evenly distributed along the perfect correlation line, and statistics show a regression factor very close to 1.

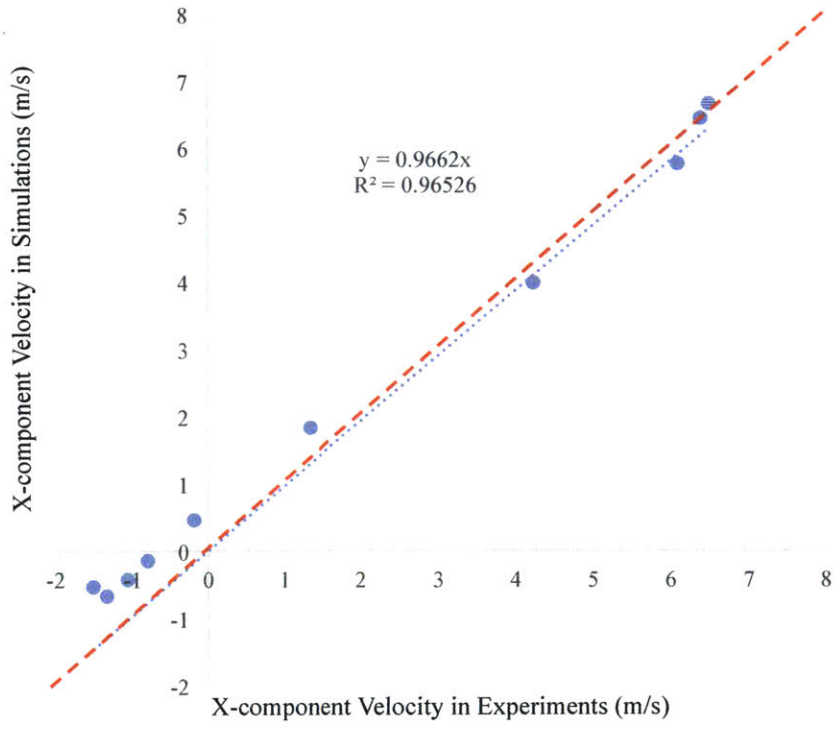

Figure 3.3. Data correlations for wind velocity between the LBM simulation and wind tunnel experiment at centerline vertical plane ($y = 0$) 100 mm downstream (at Position 100).

Another way to physically interpret the results shown above is to plot and compare simulated and measured vertical wind profiles. Here, positions in both upstream and downstream directions are compared. Note that the upstream wind profile is adjusted by the downstream obstacle due to its subsonic nature (Ma < 1), as is shown in Fig 3.4 that the shape of the profile deviates from the initial power law below the building height. But as the wind flows past the building façades, the profile changes a lot from its initial condition, and negative values of the x-component velocity should show up in the downstream direction in order to form vortices in that region. We also notice that the two results are close to each other in both upper and lower heights, which validates the accuracy of the numerical scheme.

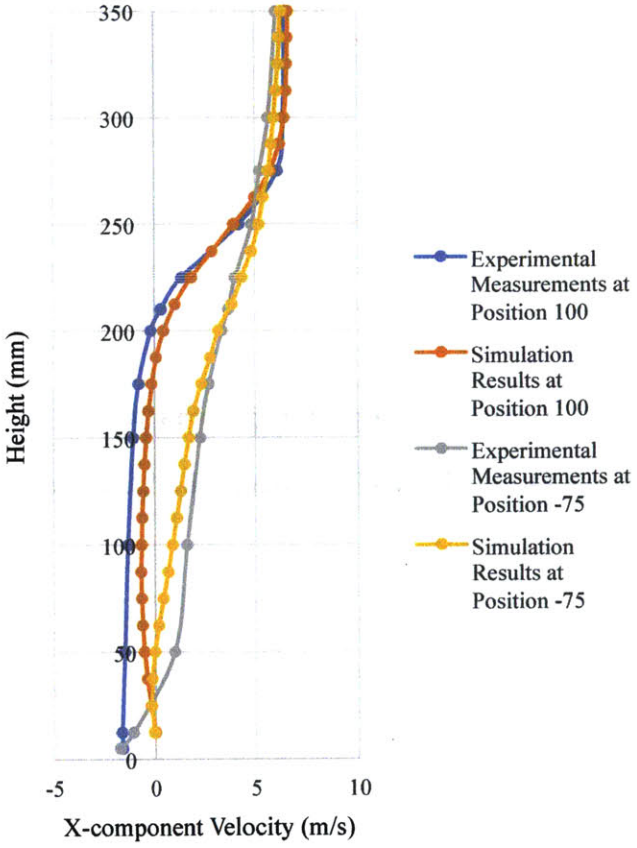

Figure 3.4. The vertical wind velocity profiles from the LBM simulation and wind tunnel experiment. Locations of the vertical lines: 75 mm upstream (Position -75) and 100 mm downstream (Position 100) from the building block.

To further verify the results of LBM for wind field modeling, we compare the numerical simulation results with wind tunnel measurements at the total test points shown in Fig 3.1.

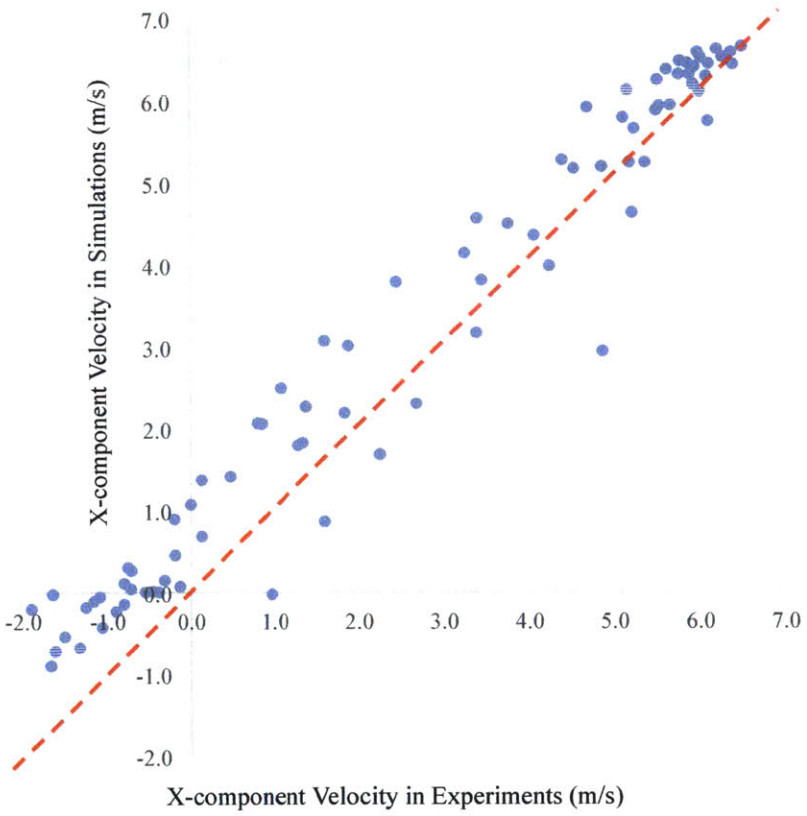

Figure 3.5. Data correlations for wind velocity between the LBM simulation and wind tunnel experiment at centerline vertical plane ($y = 0$).

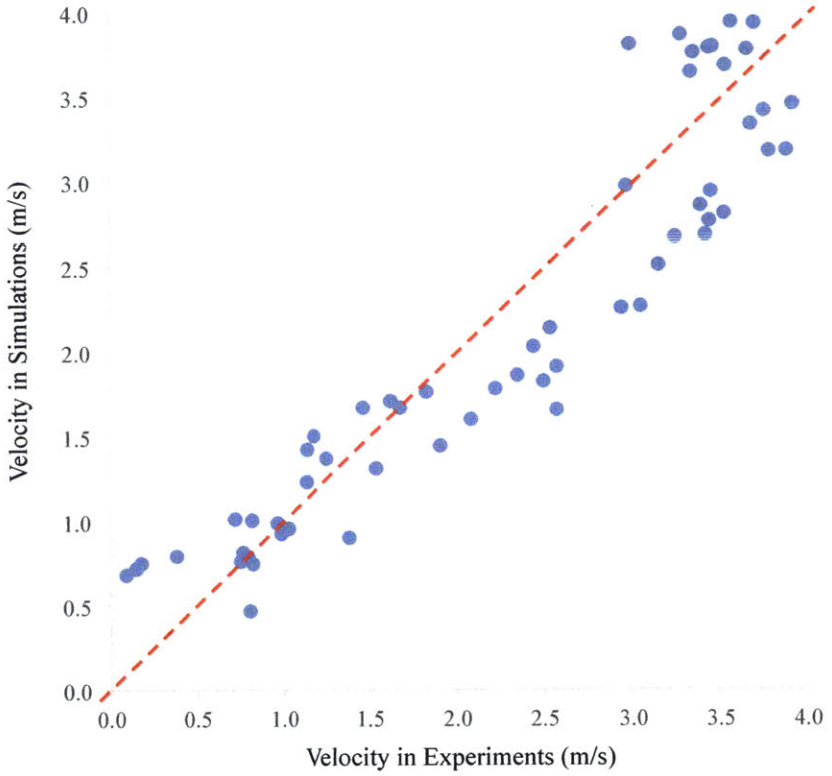

Figure 3.6. Data correlations for wind velocity between the LBM simulation and wind tunnel experiment at horizontal plane (z = 12.5 mm, corresponding to human respiratory zone).

Similarly to Fig 3.3, wind velocities from LBM simulation and wind tunnel experiments are shown above in Fig 3.5 and Fig 3.6. The red dashed line shows the best correlation line where the numerical and experimental data are exactly the same with each other. From the plots above, we can find that the numerical results agree well with wind tunnel measurements. Linear regression also shows a factor of 0.91 and 0.74 for the vertical and horizontal plane, respectively. To give a qualitative estimate of the error, we introduce the Mean Absolute Percent Error (MAPE) defined as follows (https://en.wikipedia.org/wiki/Mean_absolute_percentage_error).

$$\mathrm{M} = \frac{1}{n}\sum_{i=1}^{n}\left|\frac{A_i - F_i}{A_i}\right| \tag{3.2}$$

Where M represents the MAPE value (usually in unit of %); i refers to the test points (i = 1,2, …, n); A and F refer to the actual value (either measured by wind tunnel experiments or simulated by commercial CFD tools) and forecasting values (simulated by LBM), respectively.

The comparison in Fig 3.5 and 3.6 achieves a MAPE of 34.12% for the velocity field in the vertical plane, and 40.52% in the horizontal plane. Although the overall value is not trivial, about 80% of the points are within an error of 15%, which still proves the accuracy of the LBM simulation in wind velocity field.

3.2 Pressure field

3.2.1 Case description

Besides wind velocity, another indicator of wind field is the pressure field. In order to further validate the simulation of LBM, another case study is performed with nine uniform building blocks in the modeling domain (as is shown in Fig 3.7). The goal of this case study is to validate the LBM performance in calculating pressure field with respect to conventional CFD tools. The CFD tool we use for comparison is scSTREAM, and Large Eddy Simulation (LES) with a Smagorinsky model used in turbulent flow simulation. As with LBM, uniform gridding is performed on the whole domain, and roughly 2 million nodes are involved in the simulation. No heat transfer process is simulated in the model (no energy equation is solved), which satisfies the same assumptions with LBM. A first-order upwind scheme is used in the discretization, and all of the building façades besides the ground are set as no-slip wall functions while the top and horizontal edge of the domain are set as free-slip conditions. Steady-state analysis is conducted, and the stop criteria is combined with a maximum of 1,000 iterations and a convergence criterion of 10^{-4}.

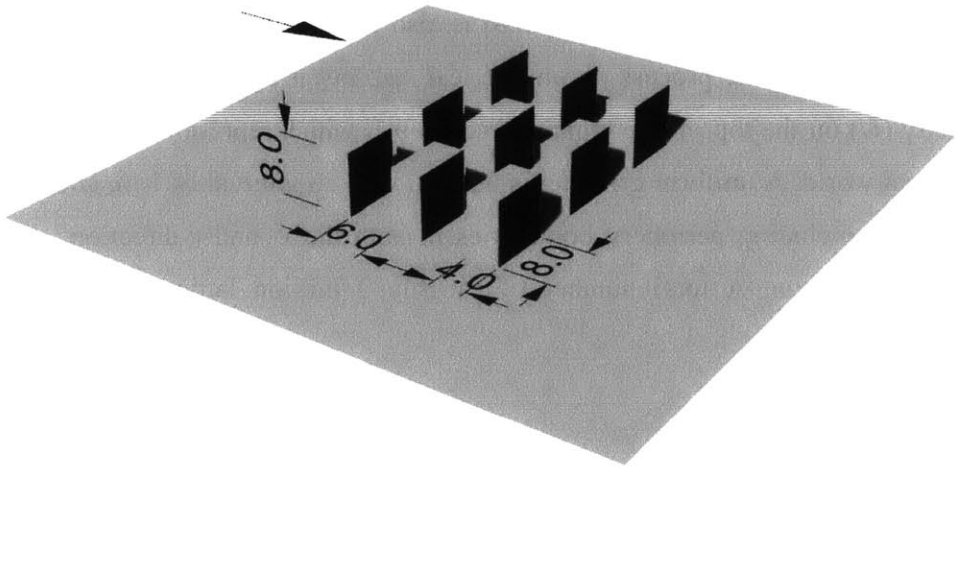

Figure 3.7. Schematic of the uniform building community and the numerical modeling domain with wind coming from left (constructed in Rhino).

In the physical domain, the building community is set up in the center of the domain, with a length of 4.0 m, width of 8.0 m and height of 8.0 m. Intervals between neighboring buildings are uniformly 6.0 m. The upwind velocity distribution satisfies the power law along the vertical direction, which is the typical setting of inlet wind profile in ASHRAE Handbook of Fundamentals (ASHRAE 2013), with the maximum value of 5 m/s at the top of the modeling region (maximum height of 80 m), and wind speed is uniform in horizontal plane. The expression of the wind velocity is shown as follows. Here we choose a pre-defined terrain of the Class IV in scSTREAM, i.e. urban area formed by medium-rise buildings (4-9 story building), and the power is set up approximately as one fourth.

$$u(z) = 5z^{1/4} \tag{3.3}$$

Where z is the height (unit: m) and u is the wind velocity at a certain height (unit: m/s).

In the numerical domain of LBM, buildings are centered in a cube of 160 m in both horizontal directions and 80 m in the vertical direction. Equations (2.8) and (2.24) are used for calculation of the pressure field. As was done in the previous case study, in order to keep the dynamic similitude for the LBM model, Equation (2.28) is also used to set up the gridding and relevant parameter values, and in the process, the numerical stability is again carefully considered. The lattice velocity (U) on the top of the domain is set as 0.1, which represents the physical value of 5 m/s in the real world. A uniform gridding is utilized with an interval of 1 m, and thus there are 161 lattice nodes including periphery boundaries in both the x- and y-direction, as well as 81 nodes in the z-direction. A total number of roughly 2 million lattices are involved in the calculation.

3.2.2 Results and Discussions

Pressure contour maps, simulated by conventional CFD tool and LBM, are plotted respectively for the horizontal plane in Fig 3.8 and Fig 3.9. Note that the pressure shown here is the net pressure deducted from the freestream pressure in the upwind direction. Positive values mean an increase in the total pressure compared with upstream conditions, and in contrast negative values mean a decrease in pressure. The horizontal plane is located at the height of 2 m above the ground level, which is near the human respiration zone. For LBM simulation, we approximate the wind field as steady-state (particles reaching local equilibrium state) after 3,000 runs for the whole domain.

Results show a high pressure area on the front of the building façades, corresponding to the stagnation region. It makes sense since the wind velocity is close to zero and according to Bernoulli Equation (Kundu 1990), $p+\frac{1}{2}\rho v^2 = Const$, pressure reaches local maximum. To satisfy the mass balance for the flow, the wind is accelerated on lateral sides of the building façades, and pressure is largely reduced in the entrance of the building community, shown in both simulation results. Downstream in canyons, the wind velocity gradually recovers from the stagnation region and recirculating flows form, so that the magnitude of pressure will get even smaller. These phenomena qualitatively demonstrate the reliability of the LBM simulation results. The next section will provide a detailed quantitative comparison.

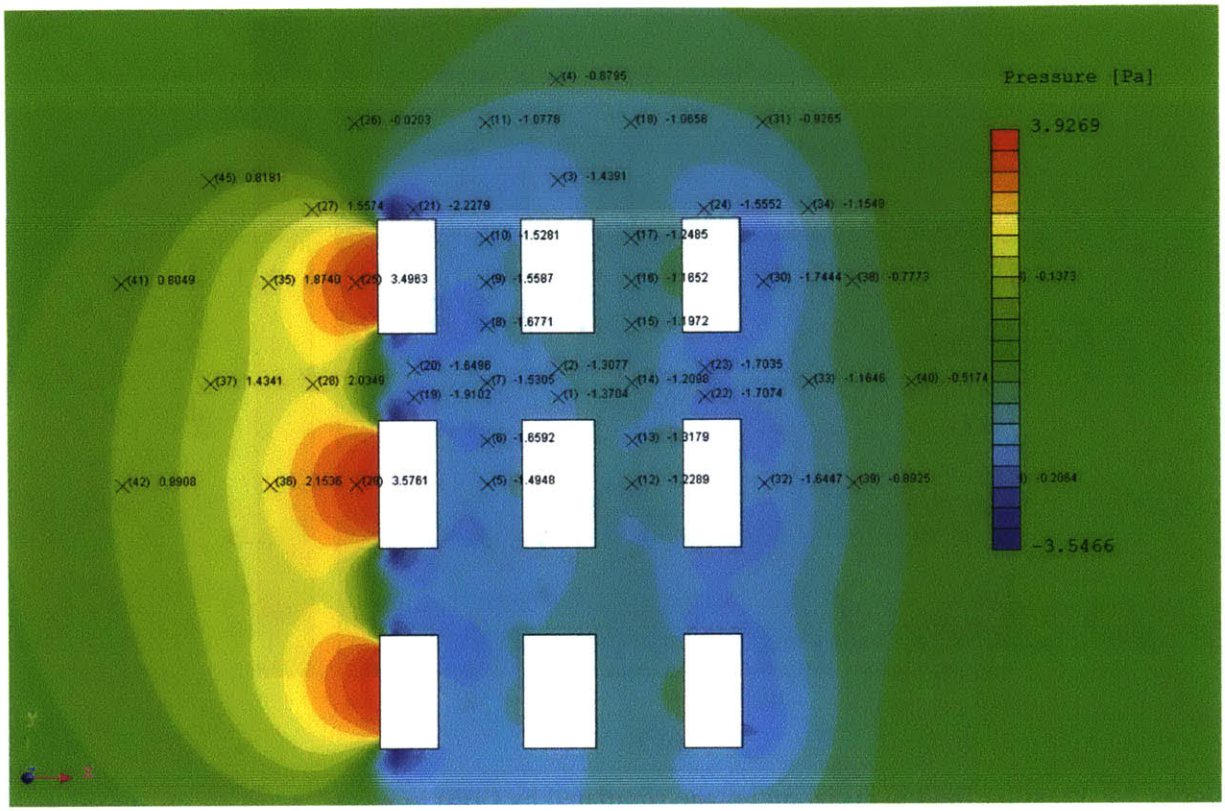

Figure 3.8. Pressure field in horizontal plane simulated by scSTREAM and schematics of test points.

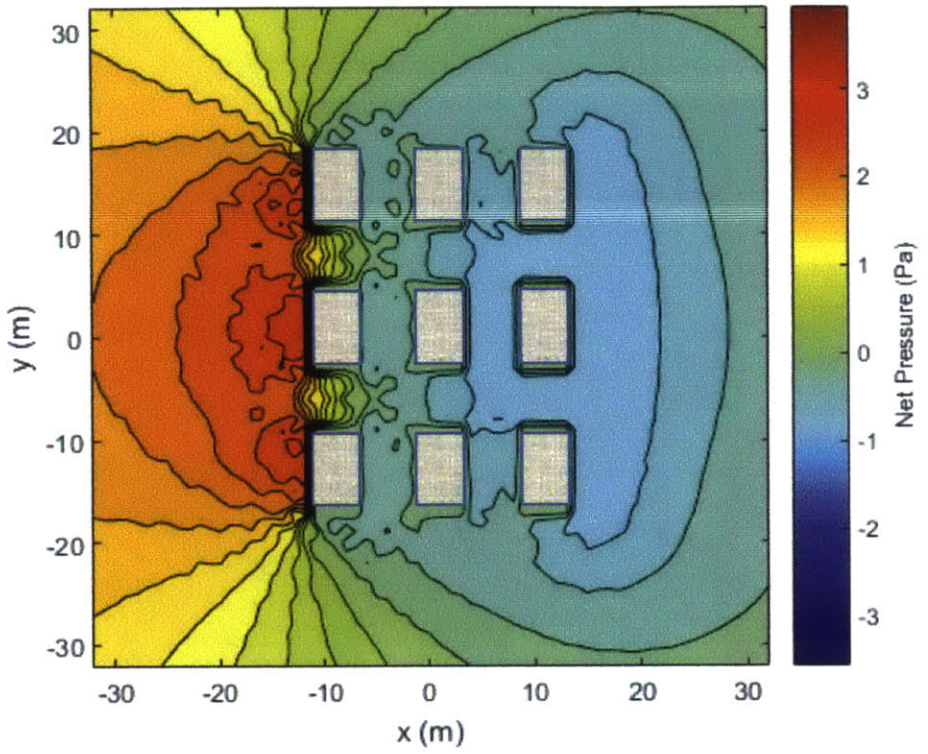

Figure 3.9. Pressure field in horizontal plane simulated by LBM.

3.2.3 Comparisons with CFD simulation results

Test points are chosen only on the upper half of the modeling domain (shown in Fig 3.8), since it is geometrically symmetric. The points are distributed separately both in the upstream and downstream regions. Values of pressure at these points are compared between conventional CFD results and LBM simulation results, as is shown in Fig 3.10. The red dashed line gives the ideal correlation that the two results coincide with each other, and the blue dotted line gives the real correlation calculated in the case.

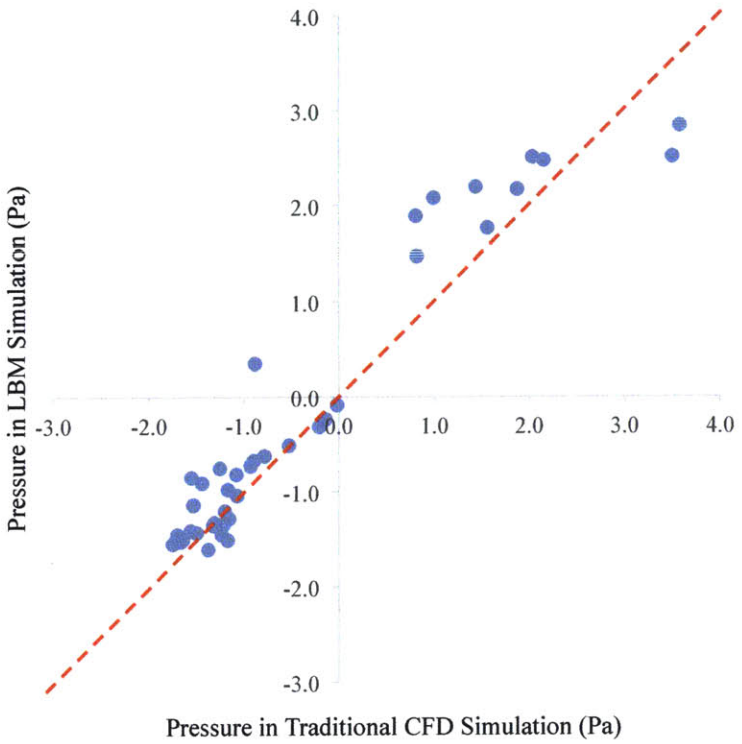

Figure 3.10. Data correlations for wind pressure between the LBM simulation and conventional CFD results at horizontal plane 2 m above the ground level (z = 2 m, corresponding to human respiratory zone).

We can find from the plot above that LBM results fit well with the conventional CFD simulation results, because all the points are evenly distributed along the perfect correlation line, especially for the negative value region. The comparison in Fig 3.10 achieves a high regression factor of 0.90 and a MAPE of 36.74% with more than 90% of the points within an error of 10% for pressure field in horizontal plane; these results combine to validate the accuracy of the LBM simulation in wind pressure field.

If the calculation time is used as a criterion for computational cost, a longer time means an expensive numerical scheme. Typically for a conventional CFD tool, it might take a couple of hours to model the turbulence around building blocks, however, in the LBM, it takes only a couple of minutes to show the simulation results. Combined with the validation results above, we can safely state that LBM is fast and relatively accurate to simulate wind field around urban

canyons, and will be a prospective for designers to evaluate outdoor air condition as well as natural ventilation potential to achieve energy-efficient building design products.

Chapter 4

Derivation of inlet velocity profile and numerical modeling domain

4.1 Three kinds of wind profile

4.1.1 The logarithmic profile

To run our LBM model for wind field simulations in building communities at neighborhood scale, initial conditions should be well investigated, especially for the upstream velocity profile. A realistic inlet velocity profile would save us from modeling an extended domain to achieve the accuracy of results in the neighborhood-scale region of interest. Note that what is meant here is not to develop a wind profile that is very close to the real upstream situation, or there's no need to run any numerical simulations since we could directly obtain the downstream wind field in a similar way.

In the atmospheric studies, the upstream velocity normally scales about 1 to 10 m/s, with building height on the scale of 10 to 100 m, and the kinetic viscosity on the scale of 10^{-5} m^2/s, so the Reynolds number for airflow around buildings scales about 10^6 to 10^8, in the range of turbulence. According to the turbulent theory, we separate the streamwise velocity u into three parts.

$$u = U + \tilde{u} + u' \tag{4.1}$$

Where $U \equiv \langle \bar{u} \rangle$ denotes the time- and spatial-average velocity, the overbar is time average and the angle bracket is spatial average. $\tilde{u} \equiv \bar{u} - U$ denotes the spatial variation of the time-average velocity, and u' denotes the turbulent fluctuation with time. To calculate the mean wind velocity U, we must construct time- and spatial-average momentum equations in a control volume (Raupach and Shaw 1982, Finnigan 2004) as follows.

$$\frac{DU}{Dt}+\frac{1}{\rho}\frac{\partial P}{\partial x_i}=-\frac{\partial}{\partial x_j}\left\langle\overline{u_i'u_j'}\right\rangle-\frac{\partial}{\partial x_j}\left\langle\tilde{u}_i\tilde{u}_j\right\rangle-D_i \tag{4.2}$$

The RHS presents three terms that accounts for the sources of the momentum change per unit mass. The first term could be rewritten as $-\frac{\partial}{\partial x_j}\left\langle\overline{u_i'u_j'}\right\rangle=-\frac{1}{\rho}\frac{\partial \tau_r}{\partial x_j}$, where $\tau_r=-\rho\left\langle\overline{u_i'u_j'}\right\rangle$ denotes Reynolds stress, referring to the spatially averaged momentum exchange due to the turbulent fluctuations. The second term could be also rewritten in the form of $-\frac{1}{\rho}\frac{\partial \tau_d}{\partial x_j}$, where $\tau_d=-\rho\left\langle\tilde{u}_i\tilde{u}_j\right\rangle$ denotes dispersive stress, referring to the time-average momentum exchange due to the spatial variation. Within the control volume, there's another source for momentum change from the local drag force due to the canopy roughness elements. In the following part, statements are all under the assumptions that the buoyancy effect is negligible in the strong wind conditions, and that the dispersive stress is relatively small and thus neglected compared to the Reynolds stress. The former assumption is often used in mechanically-driven flow case, and here for simplification, we avoid further discussion of buoyancy-driven flow near the building façades and ground level. The latter assumption is based on experimental evidence (Finnigan 1985, Cheng and Castro 2002) that the dispersive stress is small near the top of the canopy layer. Although it might be a larger fraction at the bottom of the canopy layer, the two stresses are very small near the ground, the assumption here is reasonable, and later on we will propose a solution for the concern.

When analyzing the airflow, we normally agree on the theoretical basis of the flow over a horizontally uniform environment where the vertical momentum change is of the prior concern (Monin and Obukhov, 1954). Here we introduce the mixing-length theory, and the vertical Reynolds stress $\tau_{rz}=-\rho\left\langle\overline{u'w'}\right\rangle$ will be represented in the following form (Lienhard 2013):

$$\tau_{rz}=\rho l_m^2\left(\frac{\partial U}{\partial z}\right)^2 \tag{4.3}$$

Within the inner part of the turbulent boundary layer, the shear stress dominated by the Reynolds stress remains invariant and the mixing length grows linearly with the dimensional length z (vertically),

$$l_m = \kappa z \tag{4.4}$$

Where κ is the von Karman constant, valued 0.4. In turbulent analysis, it is convenient to introduce a friction velocity u^*, which is defined as follows, in correspondence with pressure-driven freestream velocity.

$$u^* = \sqrt{\frac{\tau_{rz}}{\rho}} \tag{4.5}$$

Note that the friction velocity typically ranges from 0.05 m/s in light wind conditions to 1 m/s in strong wind conditions (Hanna and Britter 2010).

When we plug in the expressions above back to Equation (4.3), it could be then evolved as

$$\frac{\partial U}{\partial z} = \frac{u^*}{\kappa z} \tag{4.6}$$

The differential equation above gives the solution of logarithmic wind velocity, and Monin-Obukhov similarity theory modifies the profile with additional parameters according to the physical characteristics of the atmospheric conditions, which is well accepted to determine the wind profile above the canopy layer.

$$U(z) = \frac{u^*}{\kappa} \ln \frac{z - z_d}{z_0} + \psi(z/L_o) \tag{4.7}$$

Where z_0 refers to the surface roughness length, determined by surface substrates and vegetation heights and typically in the range of 0.2~1.3 m (Grimmond 1998); z_d refers to the displacement

height, accounting for the zero-plane displacement of real wind measurements from the theoretical results, typically at the scale of two thirds of the mean building height (Monin and Obukhov, 1954). The buoyancy effect on the atmospheric flow caused by the inhomogeneous temperature field is also included as a universal function related to the building height and the Obukhov length L_o given as follows.

$$L_o = -\frac{(u^*)^3}{\kappa \frac{g}{T}\frac{q}{\rho c_p}} \tag{4.8}$$

Where T is the local temperature, q is the turbulent heat flux, and c_p as the constant pressure heat capacity. The Obukhov length directly comes from non-dimensional analysis, and it is composed of three parts, i.e. u^* as indicator of turbulent momentum exchange, g/T as factor of buoyancy force, and $q/\rho c_p$ as part of turbulent heat flux. The sign of L_o is determined by the atmospheric conditions: when in stable stratification, the heat flux is downward ($q < 0$), then the Obukhov length is positive; otherwise negative in unstable stratification. Note that for simplification, the atmospheric conditions are all assumed as neutrally stratified, which means $q = 0$ ($L_o \to \infty$), and the universal function equals zero as well.

However, the logarithmic wind profile has the limitation that it can only give us a satisfactory velocity distribution above the top of the canopy layer. As is shown in Equation (4.7), z must be larger than $z_0 + z_d$ to make the streamwise velocity positive. (Although recirculating flow downstream could present negative velocities locally behind building blocks, when averaging up across-stream, it is still not wise to set the upstream horizontally-uniform inlet velocities negative.) So other theoretical analyses are needed to determine the inlet wind profile below the canopy layer.

4.1.2 Modifications on the logarithmic profile and evaluation of aerodynamic properties

In the logarithmic wind profile, we introduce two aerodynamic properties (surface roughness length z_0 and zero-plane displacement height z_d) to account for the effect of roughness elements

on airflow. And thus the evaluation of the two parameters determines the flow pattern around the buildings and affects the accuracy of the inlet wind profile.

Fig 4.1 gives a conceptual illustration of what might be the values or the trends of the values for the two parameters when the density of the building communities is different. As the density increases, the surface roughness length experiences an initial increase, then reaches the maximum, and decreases in high-density area. It makes sense that initially the roughness of the surfaces increases as the density gets higher and more roughness elements are involved, but the situation changes when new added elements work as shelters for neighbors and reduce the effective surface drag due to decrease in turbulent momentum exchange within the canyons. Unlike the peak produced by z_0, z_d increases with density monotonically. At larger densities, the most dominant fraction of the total drag comes from the building façades instead of the ground surface, so the mean height of zero momentum plane (i.e. zero-plane displacement height) goes upwards.

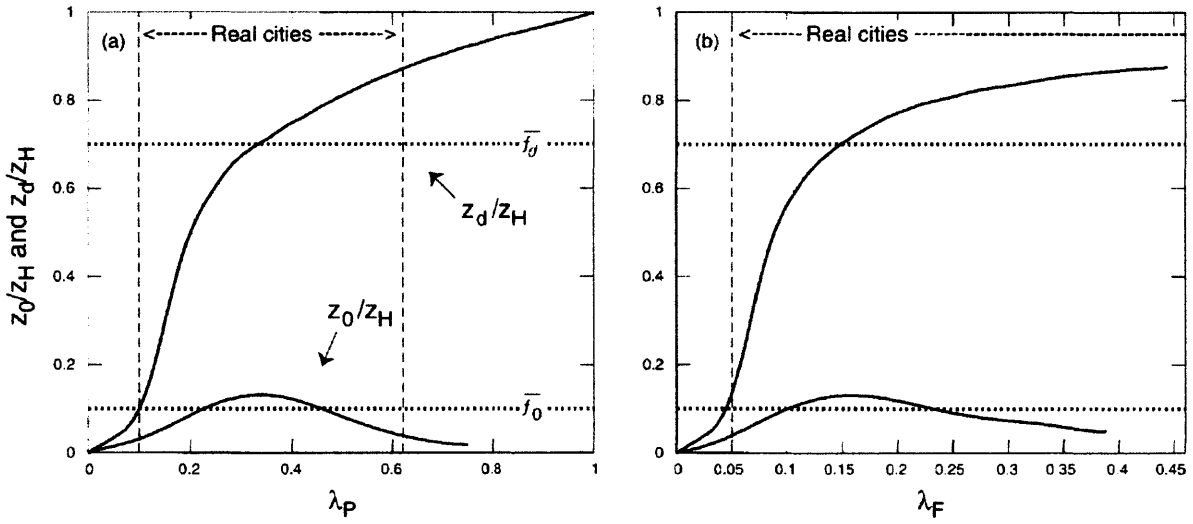

Figure 4.1. Conceptual representation of the relation between height-normalized values of zero-plane displacement (z_d/z_H) and roughness length (z_0/z_H) and the plan area density (λ_P, left) and the frontal area density (λ_F, right). (Grimmond and Oke 1998)

Two types of approaches are available for evaluation of the two aerodynamic properties: one is geometric methods, which set up the correlations between the aerodynamic properties and geometric parameters for estimation; the other is anemometric methods, which use measurements in field tests or scale models to fit for the logarithmic wind profile.

As for geometric methods, no experimental measurements are needed for evaluation, and only some parameters related to the building morphology are included (the frontal area density λ_f and the plan area density λ_p, etc.). The basic and most common geometric approach is a first-order approximation with knowledge of average building height h.

$$z_0 = f_0 h, \; z_d = f_d h \tag{4.9}$$

Where f_0 and f_d are empirical coefficients derived from observations. For simplification, the two coefficients are averaged over many types of land surfaces, and the mean values for f_0 and f_d are 0.1 and 0.7, respectively (shown as the dotted lines in Fig 4.1). Although the values are not site specific and may expose some errors when applied to real cases, they are extremely easy to use for designers and can serve as a first approximation. Many other geometric approaches have been developed, using either λ_p, or λ_f, or combined with drag coefficient and other factors to give values for z_0 and z_d. Grimmond and Oke have reviewed many of them and compared with field measurements individually, and reached a conclusion that none of them prove robust enough for application in a randomly-given real case. The main reason is that geometric methods originate from wind-tunnel experiments with constant upwind direction and regular arrays of buildings on homogeneous roughness surfaces, so they only account for idealized flow patterns with simplified assumptions.

In theory, anemometric methods can provide a more realistic wind profile with sufficient amounts of measurements. But the accuracy is proportional to the expenses it takes. To give a space- and time-average vertical velocity distribution, tall towers have to be installed in the regions of our interest. Even without the feasibilities of the installation, the large amounts of data needed for post-processing as well as the great financial costs will prevent consideration by designers. Especially for design work, the building entities have not been created in the site, and

it is totally impossible to complete the field analysis beforehand. Scale models, or wind-tunnel experiments can be utilized instead, however, Grimmond and Oke address that there is a significant difference between field projects and scale models, leaving the substitutes unwarranted. Part of the discrepancy is due to the irreducible errors from the necessary process of scale effect and geometric simplification. In a nutshell, the sparsity and scattering of the available field sources limit the use of anemometric approaches as our first choice for evaluation.

For our purpose, precise values for the two aerodynamics properties are unnecessary if large costs are paid for that, especially because the logarithmic profile is not very sensitive to uncertainties in z_0 and z_d. After careful tradeoffs between the two methods, we prefer the first-order approximation expressed in Equation (4.9). To make the approach widely applicable, we categorize the building communities into three classes, with low, medium and high densities (as described in Table 4.1). Different values of coefficients are given to achieve the modified estimation of surface roughness length and displacement height.

Table 4.1. Evaluation of the two aerodynamic properties in three different classes of building communities (Values extracted from Grimond and Oke 1999).

Class of building communities	λ_p	λ_f	λ_r	f_0	f_d
Low-density Buildings are small and widely spaced, e.g. single-family houses, light industrial area, and shopping malls with large parking lots.	0.05~0.3	0.05~0.1	0.05~0.3	0.1	0.5
Medium-density Buildings with two to four stories and closely spaced, e.g. combos and apartments with open areas, industrial area, churches and schools.	0.3~0.5	0.1~0.3	0.3~1	0.1	0.6
High-density Tall buildings in densely spaced urban area, e.g. high-rise apartments, industrial factories with tall towers, commercial sites, downtown area.	>0.5	>0.3	>1	0.1	0.7

4.1.3 The exponential profile

In the previous governing equation for momentum exchange, we have found two sources (i.e. Reynolds stress and drag force) acting together to form turbulent flow. When the canopy region is sufficiently extensive, we could then assume that the wind field reaches a steady-state equilibrium, or in other words, the vertical gradient of Reynolds stress and the drag force balance out dynamically.

$$-\frac{1}{\rho}\frac{\partial \tau_{xz}}{\partial z} = -D_x \tag{4.10}$$

To further extend the drag force with regard to the velocity components, we introduce a sectional drag coefficient $\overline{c}_D$, averaged over building height h. According to the definition of the drag coefficient, we could arrive at the following expressions of the total drag force per unit air volume.

$$\rho D_x = \frac{\overline{c}_D \cdot \left(\frac{1}{2}\rho U^2\right) \cdot A_f}{h\left(A_t - A_p\right)} \tag{4.11}$$

Where A_f is the frontal area (vertical-plane area for building façades), A_p is the plan area (horizontal-plane area for building surface), and A_t is the total floor area (horizontal-plane area for both building surface and half of the spacing between neighbors).

Equation (4.11) can then be evolved into the following form where the drag force is in quadratic relations with streamwise velocities.

$$D_x = \frac{U^2}{L_D}, \quad L_D = \frac{2\left(1-\lambda_p\right)}{\overline{c}_D \lambda_f} h \tag{4.12}$$

Where L_D is the canopy drag length, determined by the building geometries, layout and surfaces; λ_f is the frontal area density and λ_p is the plan area density. In practical use, Coceal and Belcher (2004) propose a constant value $\overline{c}_D = 2$ for the average drag coefficient after analyses of different observations, and thus the canopy drag length will be further simplified as,

$$L_D = \frac{1-\lambda_p}{\lambda_f} h \tag{4.13}$$

When we substitute Equation (4.3), (4.12) and (4.13) back into Equation (4.10), it gives,

$$\frac{\partial}{\partial z}\left[\left(\frac{\partial U}{\partial z}\right)^2\right] = \frac{U^2}{l_m^2 L_D} \tag{4.14}$$

Raupach et al. (1980) show that the mixing length in the canopy is expected to be constant, denoted as l_c, because the dominant eddies mixing within the canopy are produced by the strong shear stress at the top of the canopy layer. And thus, the denominators on the RHS are purely constant with respect to z. Here we call them together as l_s, and to make the solution succinct, we impose the relation as follows.

$$l_s^3 = 2 l_m^2 L_D \tag{4.15}$$

Define a variable $y = \frac{\partial u}{\partial z}$ related only to u (here and below, all the U is written as u for symbolic derivation); then $\frac{\partial y}{\partial z} = \frac{dy}{du}\frac{\partial u}{\partial z} = y\frac{dy}{du}$, and Equation (4.14) will collapse into a 1st-order Ordinary Differential Equation (ODE).

$$u^2 du = l_s^3 y^2 dy \tag{4.16}$$

The solution for y is,

$$u = l_s y \tag{4.17}$$

Substitute y in the equation, we can get

$$\frac{du}{u} = l_s dz \tag{4.18}$$

If the wind velocity at the building height u_h is known, then the wind profile will be displayed as,

$$U(z) = u_h \exp\left[(z-h)/l_s\right] \tag{4.19}$$

Apparently, the solution gives us an exponential velocity profile within the canopy layer. When we define a damping factor a, it evolves into (Macdonald 1998),

$$U(z) = u_h \exp\left[-a(1-z/h)\right] \tag{4.20}$$

$$a = h/l_s = h/\left(2i_c^2 L_D\right)^{1/3} \propto \left(h/L_D\right)^{1/3} \tag{4.21}$$

Here we assume that the mixing length is proportional to the average building height, since it is dominated by the shear stress on the top of the canopy layer. And from the Equation (4.13), we could assert that the damping factor is closely related to the building morphology. Macdonald (1998) calculates the damping factor (or in his paper called attenuation coefficient) from the experimental data and plots them together with the frontal area density (or called packing density). And he approximates the damping factor with a linear regression with the density $a = 9.6\lambda_f$, as we can see from the figure below.

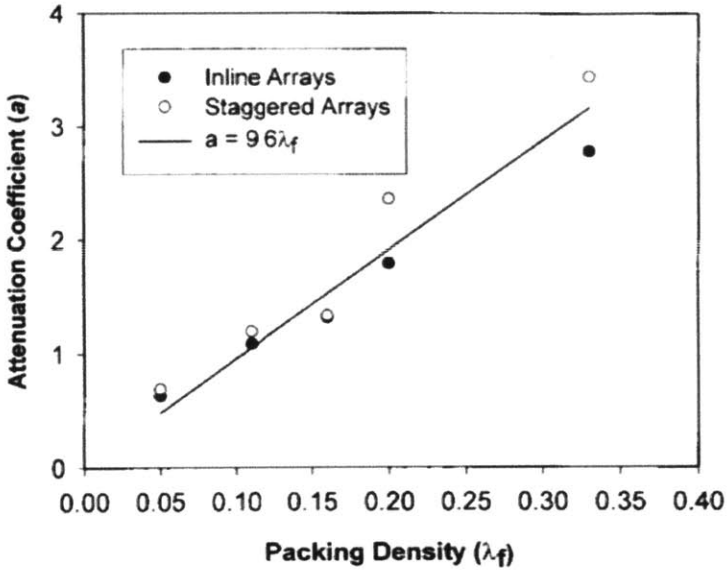

Figure 4.2. Variation of the attenuation coefficient with array packing density. (Macdonald 2000)

The simple exponential profile is more convenient for users to set up, as there is only one lumped parameter in the equation that is also linearly correlated to the frontal area density. The profile could be also rearranged as a dimensionless form with the velocity ratio $(U(z)/u_h)$ and the dimensionless height (z/h). Near the ground level, the wind velocity will still be positive but with very small values, which accounts for the attenuation effect of the recirculating flow with locally negative velocities. However, when in practical use, Macdonald also finds that the exponential profile could only fits well with measurements with $\lambda_f < 0.3$; for high-density building communities, where skimming flow tends to appear within the canyons, it is not accurate enough for application. Furthermore, it is also not feasible to give an exact answer for wind velocity at the average building height, since the velocity gradient is very large in that limited region, thus reducing the accuracy of the absolute values.

4.1.4 The uniform profile

In order to solve for the problems stated above, Britter proposes a characteristic in-canopy velocity U_c, which is representative of the time-average momentum within the whole canopy region. We will no longer care about the the variation of velocity with height. The most

simplified wind profile is established with a single value of a uniform velocity. As we can see below, the typical form of the wind profile is then replaced by a simplified uniform velocity within the canopy layer.

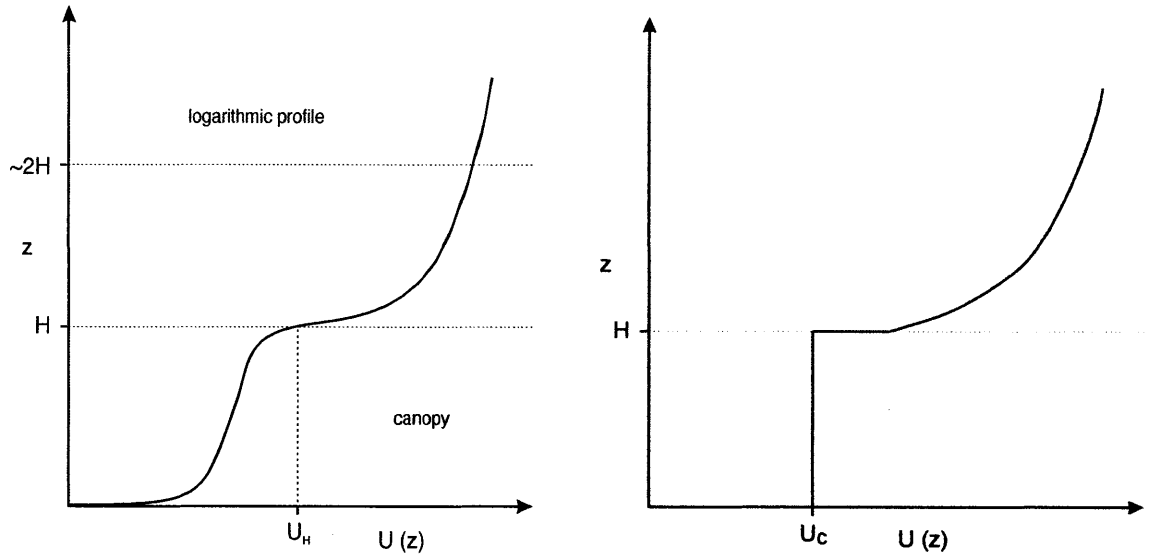

Figure 4.3. Sketch of the simplified wind profile (right) approximated with real case (left). (Britter 2003)

Consider the total drag force acting on the urban canopy, we will have

$$\tau_{rz} A_t = \overline{c}_D \cdot \frac{1}{2} \rho U_c^2 \cdot A_f \tag{4.22}$$

When it is combined with Equation (4.5) and (4.11), we can obtain the expression of the uniform velocity as,

$$U_c = u^* \left(\frac{\lambda_f}{2} \right)^{-1/2} \tag{4.23}$$

The average drag coefficient $\overline{c}_D$ is assumed to be approximately 1 in consideration of rectangular, sharp-cornered buildings, and the comparative results show good agreement with experimental

data for $0.01 < \lambda_f < 0.44$ (Britter 2003). Since further LBM simulations will be performed after the inlet wind profile is given, the lumped velocity seems a good start, and extremely easier for designers' use.

Although a uniform profile is an easier setup for the upwind profile within urban canopy layer, one needs to be careful with the limitation of this simplified approach. I performed a comparative study between exponential and uniform profile set up for building communities with different frontal area densities. The average building height for all the communities is set as 15 m (5-storey high). The frontal area density λ_f ranges from 0.05 to 0.5 with an interval of 0.1. Other useful parameters are valued as shown in Table 4.2, including the two aerodynamic properties for rural (with subscript *r*, and z_{dr} is assumed to be zero) and urban areas (with subscript *c*).

Table 4.2. Parameter values in the comparative study cases (including aerodynamic properties and meteorological measurements).

	z_{dc}	z_{0c}	z_{0r}	z_{ref}	u_{ref}	z_b	u^{*}[1]	u_h[2]
$\lambda_f < 0.3$	7.5	1.5	1	10	2	45	0.410879	1.653213
$0.3 \le \lambda_f < 0.5$	9						0.416157	1.442291
$\lambda_f \ge 0.5$	10.5						0.421806	1.158503

Unit: m

The two velocity profiles are calculated from the parameter values given above, and compared vertically at different heights.

[1] Calculated with Equation (4.34).
[2] Calculated with Equation (4.36).

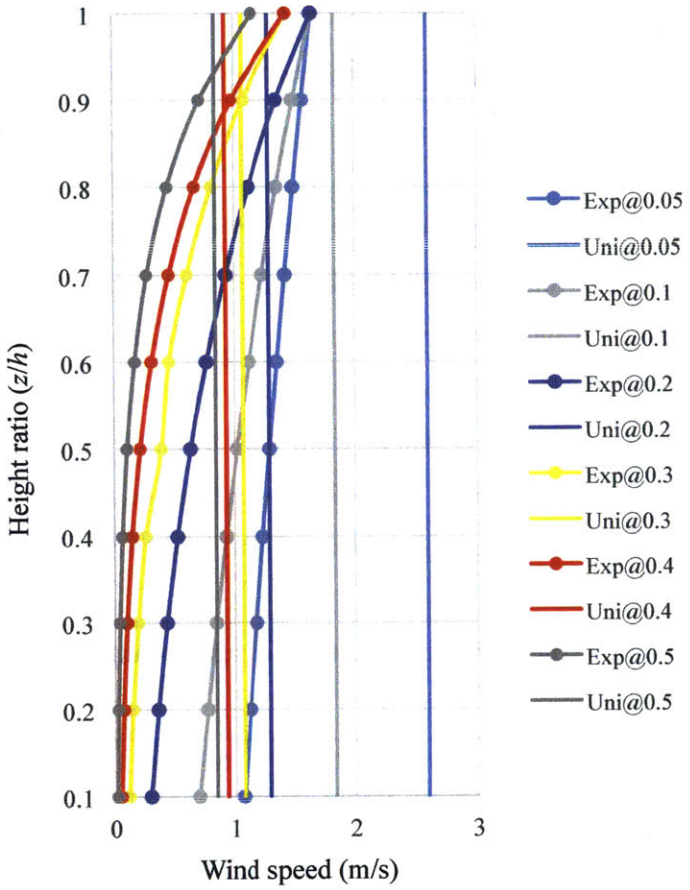

Figure 4.4. Comparison of exponential and uniform profile in different building communities with different frontal area density λ_f. (Exp / Uni refers to exponential / uniform profile; @# refers to the values of λ_f.)

As is shown above, when the density is very small, the uniform profile largely deviates from the exponential shape. When the density is larger or equal to 0.3, the uniform profile intersects the exponential profile, which proves its reliability for the setup of upwind profile in the canopy layer. Combined with the statements before, it is recommended that the uniform profile be constructed when the frontal area density λ_f is larger or equal to 0.3, and otherwise, the more complex exponential profile be set up.

4.1.5 Summary

In this section, three types of wind profile have been examined, and their applicability and limitation are evaluated respectively. The logarithmic profile, based on prevalent turbulent models, best estimates the wind velocity above the canopy layer, or in other words, above the average building height. The two aerodynamic propertes regarding the roughness are evaluated, using a simple first-order geometric approach related to the building height. Different classes of building communities are considered, and different values are given for the coefficients individually, so as to reduce the system errors with respect to the reality. The exponential profile is derived from the dynamic balance between surface drag force and vertical Reynolds stress on building façades. It has been proved practical in a limited region when the frontal area density is smaller than 0.3. And for building communities with high densities, it can be substituted by a uniform wind profile, since the wind velocities are of small values within the urban canyons.

To sum up, the inlet wind profile we choose for LBM modelling is given as follows. Note that surface roughness length z_0 and zero-plane displacement height z_d are obtained from Table 4.1, and that only some morphological parameters (i.e. the mean building height h and mean width of the streets in between the neighboring buildings w, the frontal area density λ_f, the plan area density λ_p, and the canyon aspect ratio λ_r) should be pre-calculated in advance. Note that all the parameters are averaged over the whole modeling domain.

When $\lambda_f < 0.3$,

$$U(z) = \begin{cases} \dfrac{u^*}{\kappa} \ln \dfrac{z - z_d}{z_0}, & z \geq h \\ u_h \exp\left[-9.6\lambda_f \left(1 - \dfrac{z}{h}\right)\right], & z < h \end{cases} \tag{4.24}$$

When $\lambda_f \geq 0.3$,

$$U(z)=\begin{cases}\dfrac{u^*}{\kappa}\ln\dfrac{z-z_d}{z_0}, & z\geq h\\ u^*\left(\dfrac{\lambda_f}{2}\right)^{-1/2}, & z<h\end{cases} \tag{4.25}$$

4.2 Momentum transport from the rural area to the urban canyons

When in practical use, the friction velocity u^* in Equation (4.24) and (4.25) is not straightforward to obtain. According to the definition the variable, we should know either the surface drag force or the average drag coefficient to evaluate it, and the only accurate way is to perform field experiments for real data. This is not feasible for designers. Typically, anenometric instruments (e.g. a meteorological station) are installed in rural areas, especially near the airport, and measurements are taken within the rural boundary layer where little human impact will be exerted on the site, which makes the flow field data more reliable. This section presents a way to connect the rural area with urban canyons in momentum transport, and modifies the inlet wind profile in a practical form. The approach has been successfully applied in Bueno's building energy models, where urban temperature field as well as the wind speed is derived from the reference data in rural area (Bueno 2014).

4.2.1 From rural reference location to rural boundary layer

First we take a view of the whole atmospheric boundary layer. The Atmospheric Boundary Layer (ABL) extends to a height of 1~2 km above the around, which constitutes roughly the lowest 10 pencent of the troposphere (as is shown in Fig 4.5). Within the ABL, momentum, heat and humidity fluxes are widely exchanged, and they are concentrated in the lowest 10% of layer, called the Surface Layer (SL), while the left part called Outer Layer (OL). The SL can be further divided into two parts, i.e. the Roughness subLayer (RL) and the Inertial subLayer (IL). Typically, the RL extends up to twice height of the average building height, where flow patterns are largely affected by local roughness elements; while IL, ranging from the top of RL to the bottom of OL, is the region where local momentum exchanges have been adapted to a non site-specific condition, and surface roughness at the bottom has been averaged out.

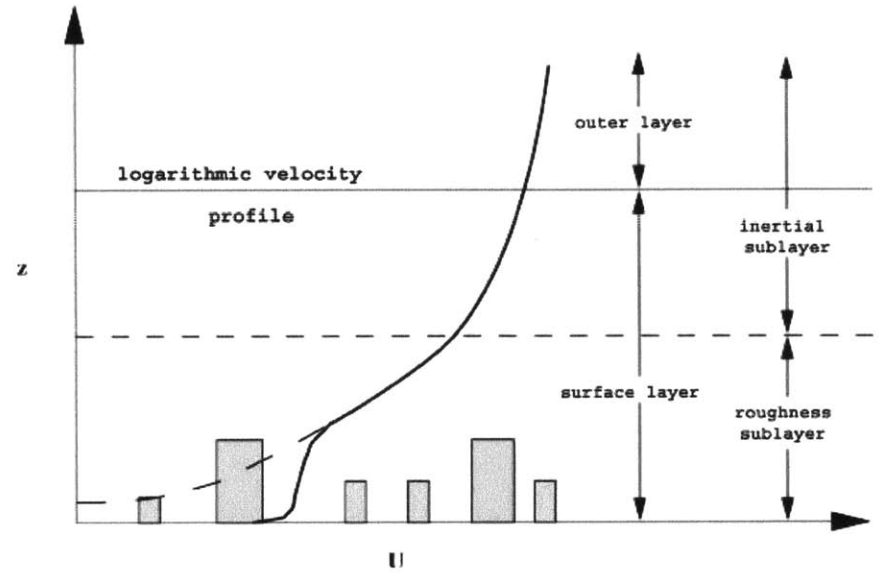

Figure 4.5. Schematic of the atmospheric boundary layer. (Britter and Hanna 2003)

One possible way to evaluate the friction velocity is to utilize a known value of wind velocity at a reference location, and then take it back to the logarithmic profile to obtain the result. Typically, wind velocity is measured at a reference height of 10 m above the ground in rural areas, such as the airport. However, it is within the roughness sublayer, and thus airflow is easily influenced by local roughness elements. So we must extrapolate up to the blending height where the boundary layer has adapted to the integrated effect of the roughness surface. The top of the RL (or the bottom of the IL) seems to be a perfect choice for that, and here we set the blending height z_b as twice of the average building height h (Bueno 2013).

$$z_b = 2h \tag{4.26}$$

Since obstacles are sparsely spaced in rural regions, and in this special case, an airport is widely surrounded by open areas, the logarithmic profile can be extended downward to the reference height, and the zero-velocity plane is very close to the ground. And thus we apply the logarithmic wind profile, plug in the known wind velocity at the reference height, and neglect the displacement height in rural area. Finally, we could then obtain the friction velocity as well as the vertical velocity distribution in the rural area.

$$U_r(z) = \frac{u_r^*}{\kappa} \ln \frac{z - z_{dr}}{z_{0r}} \simeq \frac{u_r^*}{\kappa} \ln \frac{z}{z_{0r}} \tag{4.27}$$

$$u_{ref} = U_r(z_{ref}) = \frac{u_r^*}{\kappa} \ln \frac{z_{ref}}{z_{0r}} \tag{4.28}$$

$$u_r^* = \frac{\kappa u_{ref}}{\ln(z_{ref}/z_{0r})} \tag{4.29}$$

$$U_r(z) = u_{ref} \frac{\ln(z/z_{0r})}{\ln(z_{ref}/z_{0r})} \tag{4.30}$$

Where u_{ref}, z_{ref}, z_{0r} are all known values, and denote the wind velocity at the reference height, reference height and roughness length in rural areas, respectively. All the lower subscript *r* refers to the rural values.

4.2.2 From rural boundary layer to urban boundary layer

Equation (4.29) gives the wind profile in rural areas with respect to all known rural values. In order to derive the profile in urban canyons, we must draw a connection between rural and urban values. In the previous statement, we assert that at the blending height, the wind velocities approach the freestream or geostropic speed, which is not interrupted by the local roughness and not differentiated between rural and urban areas. Thus we assume that the wind velocities are approximately the same at that level.

$$U_r(z_b) = U_c(z_b) \tag{4.31}$$

$$U_c(z) = \frac{u_c^*}{\kappa} \ln \frac{z - z_{dc}}{z_{0c}} \tag{4.32}$$

Where z_b is the blending height, and all the lower subscript *c* refers to the values in urban canyons.

Combine Equation (4.30), (4.31) and (4.32), and we then arrive at the following expression and get the friction velocity in urban areas.

$$u_{ref}\frac{\ln\left(z_b/z_{0r}\right)}{\ln\left(z_{ref}/z_{0r}\right)}=\frac{u_c^*}{\kappa}\ln\frac{z_b-z_{dc}}{z_{0c}} \tag{4.33}$$

$$u_c^*=\kappa u_{ref}\frac{\ln\left(z_b/z_{0r}\right)}{\ln\left(z_{ref}/z_{0r}\right)\ln\left[\left(z_b-z_{dc}\right)/z_{0c}\right]} \tag{4.34}$$

4.2.3 From urban boundary layer to urban canopy layer

When we substitute Equation (4.33) back into the logrithmic profile in urban areas, eventually we get a modified form of the logarithmic profile with only one unknown variable, the vertical height z.

$$U_c(z)=u_{ref}\frac{\ln\left[\left(z-z_{dc}\right)/z_{0c}\right]}{\ln\left[\left(z_b-z_{dc}\right)/z_{0c}\right]}\frac{\ln\left(z_b/z_{0r}\right)}{\ln\left(z_{ref}/z_{0r}\right)} \tag{4.35}$$

Within the urban canyons, as we suggest before, either the exponential profile or the uniform profile should be used. In Equations (4.24) and (4.25), there are still two parameters not straighforward to obtain. For the wind velocity at the mean building height u_h, it is not convenient to get the values directly by field measurements, since the presence of many irregular building façades leads to complex airflow patterns near the rooftops. The alternative way for determination of u_h is to connect the exponential profile with the logarithmic profile, using the continuity nature of fluid flow. At the average building height, the wind velocity calculated from either of the two profiles must reach the same result. This equality shows the value for u_h when we substitute h for z in Equation (4.35).

$$u_h=U_c(h)=u_{ref}\frac{\ln\left[\left(h-z_{dc}\right)/z_{0c}\right]}{\ln\left[\left(z_b-z_{dc}\right)/z_{0c}\right]}\frac{\ln\left(z_b/z_{0r}\right)}{\ln\left(z_{ref}/z_{0r}\right)} \tag{4.36}$$

The other parameter is the friction velocity in the uniform profile, which is obtained in Equation (4.34).

4.3 Adjustment distance along the fetch

Besides the boundary conditions, we also need to define a suitable modeling domain to run the LBM. Obviously in designers' expectation, the minimum computational cost is the priority for the choice of wind field modeling, which is partly affected by the size of the modeling domain. A large domain can provide enough room for the airflow to fully develop but also requires a great amount of numerical calculations on the numerious computational nodes. But we can not arbitrarily reduce the size of the modelling domain, albeit with reduced costs, because the simulation is vulnerable to inaccuracy due to the limited region for adjustment of the roughness effect. So careful analysis of adjustment distance is worthwhile to define the optimal size of modeling domain.

In Section 4.1, we have derived the inlet wind profile in the vertical direction. And we assume that only vertical momentum exchange is prevalent in the airflow, which leads to uniform upstream wind in the horizontal direction. It is always the case along the fetch before the flow meets buildings and trees in urban canyons, and until then, local roughness elements begin to interact with the airflow by the surface drag force. Within the urban canyons, the horizontal momentum exchange can no no longer be neglected, because the entrainment effect dominates around building corners and proceeds to influence the airflow deep within the canyon. The horizontal wind profile is no longer uniformly distributed, and the vertical profile can not retain its upstream shape either due to the horizontal advective fluxes.

Equation (4.2) depicts the change of the momentum in any direction; in the previous sections, the z-component was further analyzed and the exponential wind profile in vertical direction was obtained. Similarly, here it is without loss of generality to assume that the streamwise direction is along the x axis. When we solve the z-component momentum equation within urban canyons, perturbations of the equilibrium vertical wind profile should be considered. A perturbation velocity u_p is added to the time- and spatial-average velocity U to account for the horizontal

advection. The exponential profile continues to be used as before for the average velocity distribution, and if we assume that the initial perturbation velocity is simply proportional to the average velocity along the z-direction, we could imagine that it is of a similar exponential profile for the perturbation velocity along the fetch. To make the solution succinct, we define the origin at the center of the building communities of our interest, and take the average building height as the datum in the vertical direction. And thus, we obtain the expression of the downstream perturbation velocity along the fetch as follows (Coceal and Belcher 2004).

$$u_p(x,h) = u_p(0,h)\exp(-x/L_D) \tag{4.37}$$

It makes sense that the perturbation velocity decays exponentially downstream along the fetch, as the airflow gets far away from roughness elements. To relate the perturbation with the average velocity, dimensional analysis should be conducted on the momentum equation. Since the horizontal momentum fluxes are not negligible, the advection term $u_p \dfrac{\partial U}{\partial z}$ and the drag force D_x must be of the same order. If the average velocity at the mean building height u_h is taken as the characteristic average velocity, the mean building height h as the characteristic length of z, when combined with Equation (4.12), we get

$$\begin{aligned} u_p \frac{u_h}{h} &\sim \frac{u_h^2}{L_D} \\ u_p &\sim u_h h / L_D \end{aligned} \tag{4.38}$$

We define the adjustment distance x_a as the location where the vertical momentum transport recovers its dominance over the airflow and the perturbation velocity is the same order with the friction velocity. Therefore, the expression of x_a will be of the following form (Coceal and Belcher 2004).

$$x_a \sim L_D \ln\left(\frac{u_h}{u^*}\frac{h}{L_D}\right) \tag{4.39}$$

Numerical experiments have been performed to determine the coefficient in Equation (4.39), where u_h, u^* and L_D are calculated from Equation (4.36), (4.34) and (4.13) respectively. Typically, the log factor ranges from 0.5 to 2 in urban areas. Linear regression is also processed on data points for x_a/L_D. Results have shown that the log factor can be approximately taken as 3 (Coceal and Belcher 2004). In practical use, the adjustment distance can be calculated as follows. Note that the morphological parameters here are only averaged over the building communities of our interest.

$$x_a = 3L_D = \frac{3\left(1-\lambda_p\right)}{\lambda_f} h \tag{4.40}$$

From the expression, we can see that the adjustment distance is proportional to the average building height. If the building communities are composed of high-rise buildings, the freestream wind tends to flip across the canyons, tranporting turbulent momentum in limited shallow regions. So it is nature for the adjustment distance to be small. And it can be proved by Equation (4.40) since the frontal area density is very large in this condition. When there are many open areas in building neighborhood, the outer wind can get enough room along the fetch to mix with airflow at lower levels, and thus it requires a longer distance to recover in the downstream. It could also be warranted in the expression above owing to the large value in the plan area density. The approximation of the log factor is reasonable as well, because the factor L_D dominates the RHS in Equation (4.39). Although an increase in canopy drag length can reduce the value of the log factor, it is still less comparable to the increasing trend in itself. So it is applicable to estimate in an approximate way for designers' use.

4.4 Setup for numerical modeling domain

The numerical modeling domain is set up in two dimensions: horizontal and vertical directions. In order to achieve the optimal size in the tradeoff between computational efficiency and numerical accuracy, the definition of adjustment distance is introduced into the horizontal setup. As is discussed in the former section, the origin is created at the geometrical center of the building community of our interest, and the horizontal modeling domain is extended out in the

radial direction from the edge of the building community to a distance of x_a which can be evaluated by Equation (4.40). Usually, we can approximate the horizontal domain as a rectangular region rather than the theoretical ellipse one, to simplify the spatial discretization afterwards. Once the modeling domain is set up in the horizontal direction, vertically, the maximum height of the modeling domain is defined as twice of the maximum building height in the whole extended region. And thus it ensures the freestream, or geostropic wind, as is stated in Chapter 4.2.1, to penetrate into the modeling domain.

Chapter 5

Lattice-Boltzmann wind field model in designer's workflow

5.1 Improved designer workflow in building simulation

The Lattice-Boltzmann Wind Field Model (LBWFM) is based on the Lattice-Boltzmann method to numerically simulate wind field in urban canyons and their neighborhoods. We have discussed in the previous chapters the computational efficiency and accuracy for the numerical scheme, as well as determination of the optimal modeling domain and proper setup of the upwind profile as initial conditions. The following paragraphs explain the workflow of the modeling work when the LBWFM is implemented in the urban design process.

As Fig 5.1 shows, the initial design is constructed in a Rhino-based environment. When it is needed to analyze the wind field within the design map, we can directly run the LBWFM in three phases before achieving the final results.

The first phase is to determine the optimal modeling domain by using the parametric values of building geometries in the building community of our interest. Three parameters are required for evaluation, i.e. the plan area density (λ_p), the frontal area density (λ_f) and the average building height, which have been defined in Chapter 1.2.2. Then we can plug these values in Equation (4.40) to calculate the adjustment distance and create the modeling domain as stated in Chapter 4.4.

After that, we go into the second phase where the inlet wind profile should be set up appropriately. Now three classes of parameters are required, which include the updated building geometric parameters for the whole modeling domain, meteorological data measured at the rural areas in the upwind direction, and a single coefficient for aerodynamic properties. For the building geometric parameters, only the frontal area density and average building height over the

whole region (including both building communities in the center of the modeling domain and the neighboring contexts on the periphery) are needed. For the meteorological data, the measured velocity (u_{ref}) as well as the vertical height (z_{ref}) to set up the anemometer should be recorded. The only aerodynamic coefficient needed is the empirical coefficient (f_d), defined in Equation (4.9), to determine the displacement height based on Table 4.1. Given all these parametric values, we can use Equation (5.1) – (5.3) to construct the inlet wind profile.

Once the initial conditions and modeling domain have been successfully set up, and given that the boundary locations have been already automatically saved in the design process, we enter the last phase to complete the numerical setting, i.e. resolution of lattice nodes and the stop criteria for iterative runs.

After runs of LBWFM, we can end up with the recorded data of wind velocity (both in the form of magnitude and vector components) and pressure for all lattice nodes. We can post-process the data and finally exhibit the velocity vector map to show the magnitude and direction of the wind speed, the velocity contour map to only show the magnitude of wind speed which could be further integrated in the outdoor thermal comfort analysis, and the pressure contour map to show the local wind pressure which could be further integrated in natural ventilation analyses.

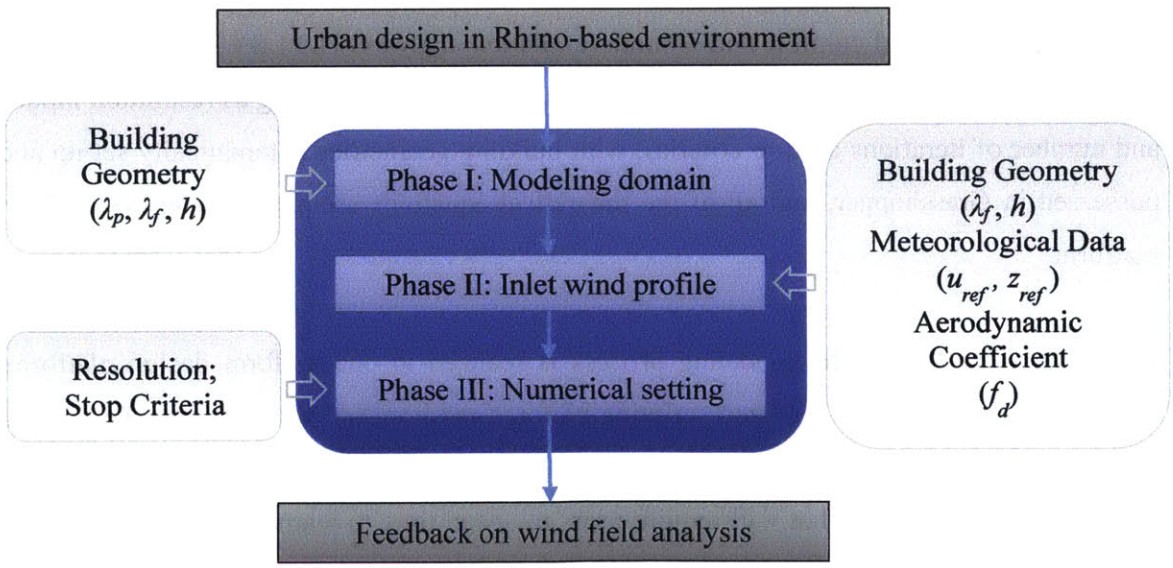

Figure 5.1. Lattice-Boltzmann wind field model implemented in designer's workflow.

Compared with the current workflow of wind field analysis using conventional CFD tools, integration of LBWFM into designer's workflow has the following merits:

First, LBWFM achieves fast and relatively accurate results for the wind field. As is discussed in Chapter 2, LBM has its hybrid nature by combining the merits of conventional CFD methods and molecular dynamics method, and inherits the advantages of easy implementation on parallel computing from discrete kinetic models. The computational efficiency is also embedded in its linear operator, which avoids iterative solving for non-linear equations in conventional CFD methods. In real case tests in Chapter 3, we have found the savings in time costs for LBM and also validated its accuracy within a mean absolute error of 40% compared to both physical experiments and numerical simulation by conventional CFD methods. The decreasing time period for simulation makes designers more willing to run the model, perform the parametric studies and evolve the initial design toward a thermally comfortable and energy efficient one.

Second, inputs of the model can be directly applied with only knowledge of the design rather than an advanced engineering background, which makes it possible for designers to run the model themselves and then realize how the design components affect the wind field as well as the outdoor thermal comfort and natural ventilation analysis. The LBWFM has only five parameters that users must manually input (i.e. u_{ref}, z_{ref}, f_d, lattice spacing as resolution inputs, and number of iterations as stop criteria), with building geometries automatically set up and possessed in Grasshopper, and all of the theoretical equations are packaged in the back-up platform.

Third, the workflow of the modeling process is realized in one uniform design platform, Rhino (together with its visualized scripting editor, Grasshopper), which is very familiar to designers and urban planners. And at the same time, it avoids lots of transitions between several commercial tools that will require users to spend time to learn and gain proficiency. Post-possessing is also directly performed in Grasshopper, and users can see the wind field results on the design products in Rhino-based environment.

5.2 Designer use guide for Lattice-Boltzmann wind field model

5.2.1 Inputs by users

Building Geometry is constructed in a Rhino-based environment and can be automatically transferred as boundary locations for the simulation. Some parameters (building densities and average building height) required to define the size of modeling domain and to set up the upwind profile can be automatically solved in Grasshopper components.

The **modeling domain** in the Lattice-Boltzmann Wind Field Model (LBWFM) is taken as the circular region (or numerically the square region in regular lattice arrangements) centered in the building communities of our interest, with the radius of adjustment distance along the fetch which can be calculated as Equation (4.40).

The numerical resolution of the LBWFM is dependent on user's choices. The total number of lattice nodes allocated in the modeling domain will be then automatically calculated in the core code. For example, we aim to simulate a region of 1 km^2 with height of 50 m. If user define the numerical resolution as 1 m wide, the total lattice nodes aligned in the program will be 1000 × 1000 × 50. Note that uniform gridding is used in the LBWFM. The three-dimensional lattice nodes are connected in an array of *D3Q19* arrangements where each lattice is closely related to 18 neighbors in different orientations, as is shown Fig 2.2 (b).

An **inlet wind profile** is also needed for modeling. The basic framework built in the LBWFM is a combination of a logarithmic profile above the urban canopy layer and either the exponential or uniform profile within the layer. The algebraic equations are shown below. Assumption are made that inlet wind comes only from the left (west) of the modeling domain and that velocity is uniform in the horizontal direction and only changes vertically.

When $\lambda_f < 0.3$,

$$U(z)=\begin{cases} u_{ref}\dfrac{\ln\left[\left(z-z_{dc}\right)/z_{0c}\right]}{\ln\left[\left(z_b-z_{dc}\right)/z_{0c}\right]}\dfrac{\ln\left(z_b/z_{0r}\right)}{\ln\left(z_{ref}/z_{0r}\right)}, & z\geq h \\ u_h\exp\left[-9.6\lambda_f\left(1-\dfrac{z}{h}\right)\right], & z<h \end{cases} \tag{5.1}$$

$$u_h=U(h)=u_{ref}\frac{\ln\left[\left(h-z_{dc}\right)/z_{0c}\right]}{\ln\left[\left(z_b-z_{dc}\right)/z_{0c}\right]}\frac{\ln\left(z_b/z_{0r}\right)}{\ln\left(z_{ref}/z_{0r}\right)} \tag{5.2}$$

When $\lambda_f \geq 0.3$,

$$U(z)=\begin{cases} u_{ref}\dfrac{\ln\left[\left(z-z_{dc}\right)/z_{0c}\right]}{\ln\left[\left(z_b-z_{dc}\right)/z_{0c}\right]}\dfrac{\ln\left(z_b/z_{0r}\right)}{\ln\left(z_{ref}/z_{0r}\right)}, & z\geq h \\ \kappa u_{ref}\dfrac{\ln\left(z_b/z_{0r}\right)}{\ln\left(z_{ref}/z_{0r}\right)\ln\left[\left(z_b-z_{dc}\right)/z_{0c}\right]}\left(\dfrac{\lambda_f}{2}\right)^{-1/2}, & z<h \end{cases} \tag{5.3}$$

Where z refers to the vertical height; u_{ref}, u_h, z_{ref} denote the wind velocity at the reference height, wind velocity at the average building height, and reference height, respectively; and z_{0r}, z_{0c}, z_{dc} denote the roughness length in rural areas, roughness length in urban areas, and displacement height in urban areas, respectively, defined as $z_0 = f_0 h$, $z_d = f_d h$ (f_0 and f_d are empirical coefficients derived from observations. For simplification, the two coefficients are averaged over many types of land surfaces, and the default values set in the model for f_0 and f_d are 0.1 and 0.6, respectively.); z_b is the blending height and defined as $z_b = 2h$; κ is the von Karman constant, given approximately as 0.4.

Designers are responsible for the inputs of several aerodynamic parameters, and they are further explained as follows.

The **reference velocity (u_{ref})** and **reference height (z_{ref})** are directly obtained from the meteorological measurements in rural areas. Typically, the reference wind velocity is measured

at a reference height of roughly 10 m above the ground near the airport. Default values of 2.5 m/s and 10 m are used in the model.

The **displacement height factor (f_d)** is given in Table 4.1 where users can select one of the three senarios and evaluate the term. Default value of 0.6 is used in the model.

The **frontal area density (λ_f)** and **average building height (h)** here are the average properties over the entire modeling region, and they are automatically solved in Grasshopper components.

Numerical convergence criteria (iterative steps) in the LBWFM is user-defined, and it affects the computational efficiency as well as the accuracy. As the value goes up, we can get closer to the steady-state solution, however in the process, more time is consumed for evaluations of the equilibrium functions in the model. A default value is given as 5,000.

5.2.2 Outputs for users

Wind velocity is depicted as a 2D vector field in both horizontal and vertical planes. Note that in the lattice world, all the variables in the model are in dimensionless form. The lattice velocity can be either positive (having the same orientation with the upwind velocity vector) or non-positive, and the magnitude ranges from 0 to 0.1, linearly corresponding to the stagnation velocity and the maximum inlet velocity in the field respectively. The output result returns the original scale in the physical world. The default output for the velocity field is set as a 2D vector field in a horizontal plane at the height of respiration zone (1.5 m or 2 m according to the numerical resolution).

Pressure is depicted as a 2D contour map in both horizontal and vertical planes. In the lattice world, the direct output result is the lattice density, and we can get the pressure field from Equation (2.24). To recover the physical scale, a scaling factor must multiply the lattice pressure. Note that the default inlet pressure is set as 1 atm (101325 Pa) for the whole field, because the vertical dimension of the building relevant studies will not exceed 1 km, which has little affect on the pressure values. Thus the default scaling factor is set as 337.75 Pa.

The **wind pressure coefficient** can also be derived from the pressure term. The expression below gives an algorithm to calculate the effective surface pressure coefficient given the original output of the lattice density field (which will be further analyzed in Chapter 6).

$$C_p^* = C_p - C_{pi} = \frac{p - p_{atm}}{\frac{1}{2}\rho u_{ref}^2} - \frac{p_i - p_{atm}}{\frac{1}{2}\rho u_{ref}^2} = \frac{p - p_i}{\frac{1}{2}\rho u_{ref}^2} = \frac{200}{3}\left(1 - \frac{1}{\rho_{lattice}}\right) \tag{5.4}$$

Where the subscript i refers to the inlet boundary conditions, and the reference velocity u_{ref} is chosen as the maximum inlet wind velocity, valued as 0.1 in the lattice world.

5.3 Modeling interface in Rhino-based environment

Fig 5.2 shows the Grasshopper components constructed for the Lattice-Boltzmann wind field modeling in the Rhino-based environment. This work was a collaboration with Dr. Timur Dogan, who set up the interface and post-possessors for visualization.

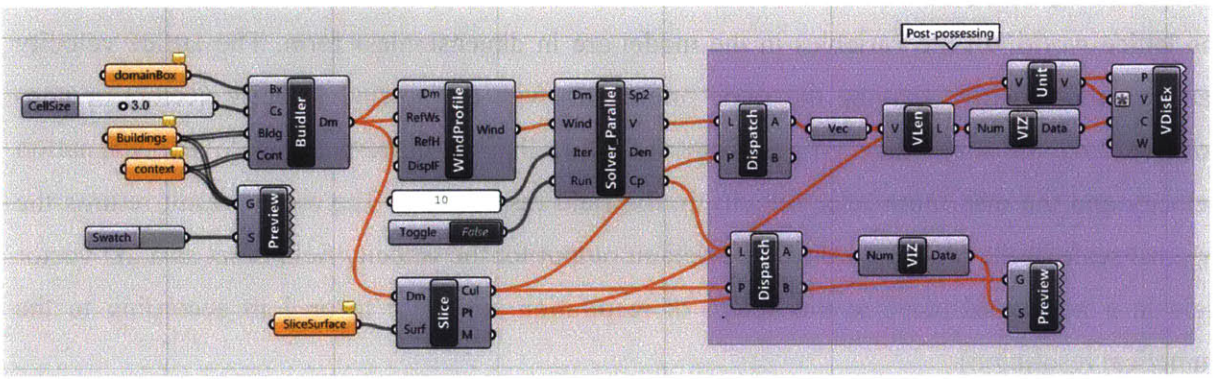

Figure 5.2. Grasshopper components constructed for LBWFM interface in a Rhino-based environment.

As we can tell from the canvas above, there are four boundary representations (breps) awaiting assignment: *domainBox*, describing the size of the modeling domain that users have pre-defined; *Buildings*, telling the program the building communities of interests; *context*, including the neighboring buildings on the periphery of the building blocks of interests, but within region of *domainBox*; and *SliceSurface*, giving the plane of interest to view the wind field results.

The first compiled component, *Builder*, serves to record the building locations constructed in Rhino, and to decide the optimal size of the modeling domain by using the building geometries that are automatically calculated in the component. The geometry builder has four main inputs, i.e. *domainBox*, *cellSize* (resolution of lattice nodes, in unit of meters), *Buildings* and *context*, and one output, *Dm*, which shows the final result of the optimal domain box for modeling. A warning will be given if the pre-defined *domainBox* is smaller than the result, in order to let users realize that the accuracy of the modeling results will be impacted by the limited size of the domain; and a suggestion will also be given if the pre-defined box is larger, in order to let users know that they can actually save computational time by reducing their modeling region without deteriorating the wind field results. Users can then decide whether to take the warning or suggestion in their coming modeling work.

The second compiled component, *WindProfile*, extracts the output of *Builder* as the total modeling domain, and sets up the inlet wind profile by using the average building morphological parameters in the domain as well as three additional inputs, which are *RefWs* (reference wind velocity, u_{ref}), *RefH* (reference height, z_{ref}) and *DisplF* (displacement height factor, f_d). The output of the component is a vertical wind profile based on the calculation results of Equation (5.1) – (5.3) and spread uniformly in the horizontal plane. The wind direction is set as orthogonal to the front face of the *domainBox*, which requires that the angle of *domainBox* itself coincide with the actual inlet wind direction.

The main component in the Grasshopper is the LBWFM solver, which contains a non-parallel and a parallel component (as is shown in Fig 5.2 *Solver_Parallel*). We can then compare and see the enhanced efficiency by using parallel computing. The inputs of the main solver require both the outputs of the first two components to define the computing domain and initial conditions, and also the numerical setting of how much iteration we expect. After the iterative runs, the model gives us four main outputs that can be either directly visualized or further analyzed and integrated. The outputs mainly contain two parts, wind velocity field, *Sp2* referring to the magnitude of velocity and *V* referring to the wind velocity vectors, and wind pressure field, *Den* referring to the density of the wind field and *Cp* referring to wind pressure coefficient. Note that

the magnitude of the wind velocity can be further integrated into outdoor thermal comfort analysis, and wind pressure coefficient into natural ventilation analysis.

The last component, *Slice*, is a visualization tool, which helps to cut a slice on the whole modeling domain and presents a 2D view of wind field at a specific plane.

Given proper contents for the breps and the required parameter values as inputs, we can directly see the visualization results of both wind velocity and pressure field back in Rhino. It will be really convenient for designers to use the models, run the wind field simulation, and directly see whether it satisfies the optimal design of thermal comfort and energy efficiency.

Chapter 6

Application of Lattice-Boltzmann wind field model in natural ventilation analysis

The Lattice-Boltzmann Wind Field Model (LBWFM) has been proved to be a fast and relatively accurate numerical simulator for evaluation of wind velocity and pressure in the external flow, and it has also been successfully incorporated in a Rhino-based environment, which makes the modeling tool designer-relevant. In addition to the two primary parameters (wind velocity and pressure), LBWFM can provide further analysis for wind-driven natural ventilation, an energy-saving alternative for mechanical cooling system to maintain indoor thermal comfort. This shows the possibility of LBWFM to combine outdoor and indoor airflow analysis for building simulation, which extends the application of the model to the design of thermally-comfortable and energy-efficient building communities.

6.1 Wind pressure coefficient

Wind-driven natual ventilation through openings in buildings results from pressure differences supported by external wind. Due to the obstruction of building façades and the shading effect of neighboring buildings, wind speed differs on different locations and, because of the coupling effect of velocity and pressure, creates surface pressure differences as driving force for airflow to go in one specific direction. To evaluate the magnitude of the driving force for building ventilation analysis, surface pressure is commonly expressed in a dimensionless form, known as the wind pressure coefficient. It is defined as follows (ASHRAE 2013).

$$C_p = \frac{p_D}{\frac{1}{2}\rho u_{ref}^2} = \frac{p_T - p_S}{\frac{1}{2}\rho u_{ref}^2} = \frac{p - p_{atm}}{\frac{1}{2}\rho u_{ref}^2} \tag{6.1}$$

Where p_D refers to dynamic pressure; p_S refers to static pressure at static condition (i.e. wind velocity is zero everywhere); and p_T refers to total pressure measured on the building surfaces, which is the sum of static and dynamic pressure. The reference velocity is mainly used to non-dimensionalize the surface pressure, and can be flexibly defined according to researchers' choice. The value used here is the largest freestream velocity at the top of the modeling domain, which corresponds to 0.1 in the settings of Lattice-Boltzmann Method (LBM).

For convenience of the computation in LBM, a relative wind pressure coefficient C_p^* is defined as the difference of the wind pressure coefficient relative to the inlet condition.

$$C_p^* = C_p - C_{pi} = \frac{p - p_{atm}}{\frac{1}{2}\rho u_{ref}^2} - \frac{p_i - p_{atm}}{\frac{1}{2}\rho u_{ref}^2} = \frac{p - p_i}{\frac{1}{2}\rho u_{ref}^2} \tag{6.2}$$

Where p_i is the inlet dynamic pressure, typically its value as the same with the atmospheric pressure.

The non-dimensionality of wind pressure coefficient shows its advantange when the coefficient value can be directly obtained from the parametric values in the lattice world, as is derived as follows with the help of Equation (2.24).

$$C_p^* = C_{p,lattice}^* = \frac{p_{lattice} - p_{i,lattice}}{\frac{1}{2}\rho_{lattice} u_{ref,lattice}^2} = \frac{\rho_{lattice}/3 - \rho_{i,lattice}/3}{\frac{1}{2}\rho_{lattice} u_{ref,lattice}^2} = \frac{2}{3}\left(1 - \frac{\rho_{i,lattice}}{\rho_{lattice}}\right)\frac{1}{u_{ref,lattice}^2} \tag{6.3}$$

$$C_p^* = \frac{200}{3}\left(1 - \frac{1}{\rho_{lattice}}\right) \tag{6.4}$$

Where the reference lattice velocity is valued as 0.1 and positioned at the top of the modeling domain, and the inlet lattice density is valued as 1. Equation (6.3) also tells that the relative wind coefficient can be easily calculated from the lattice density, one of the outputs in LBWFM. The

workflow has also been successfully set up in a Rhino-based environment, as is elaborated in Chapter 5.

From the expression of the relative wind pressure coefficient, it is clear that the wind pressure coefficient is determined by the lattice density which is largely affected by the building geometry, inlet wind direction, and the configuration of the neighboring buildings. The magnitude of the wind velocity will no longer impact wind pressure coefficient by the nature of non-dimensionality.

6.2 Indicator of natural ventilation potential — Air exchange flow rate

To further determine whether natural ventilation can perform as expected to reduce the cooling loads of the building, a quantitative parameter needs to be well defined to account for the strength of the natural ventilation potential. In terms of the cooling effect of natural ventilation, the primary concern is the mass flow rate of the cooler outdoor air and its enthalpy (or temperature) difference with the hotter air inside the buildings, and when combined together, we can then decide how much heat the exchange air can take away. Specifically in the case of wind-driven natural ventilation, the mass flow rate of the exchange air is the primary indicator to quantify natural ventilation potential. Since the density of the air changes little in the atmospheric environment, we can instead use the volumetric flow rate.

In order to calculate the air exchange flow rate through the openings on opposite building façades, we have to start with the widely used orifice equation to determine the volumetric flow rate $\dot{V}$ through one sharp-edged opening as is sketched below.

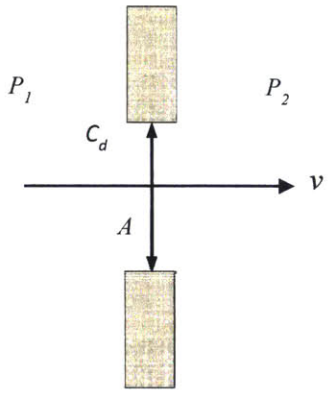

Figure 6.1. Schematic of airflow through an orifice (wind blows from outside to inside of the building).

The orifice equation is given as follows. (Etheridge and Sandberg 1996)

$$\dot{V} = C_d A \sqrt{\frac{2\Delta P}{\rho}} \tag{6.5}$$

Where P_1 and P_2 are wind pressure at outdoor and indoor condition, respectively; A is the orifice area; ρ refers to the air density; C_d refers to the discharge coefficient, defined as the ratio of the actual volumetric flow rate and the ideal flow rate calculated by the Bernoulli equation. ASHRAE Handbook of Fundamentals (ASHRAE 2013) gives a typical value of 0.6 for turbulent flows, which can be applied in atmospheric flow for natural ventilation analysis. Because the openings on building façades normally takes up only a small fraction of the total area of the wall, the orifice equation can be directly applied on determination of airflow rate across each opening.

Fig 6.2 shows airflow across two openings on the opposite side of building façades. For each opening, we can apply orifice equation to account for the corresponding airflow rate.

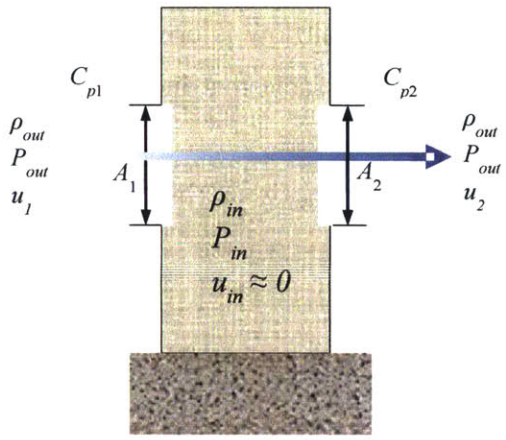

Figure 6.2. Schematic of airflow through opposite building openings (wind blows from left to right).

Applying conservation of mass to the airflow through the openings, we have

$$\dot{V} = \rho_{in} C_d A_1 \sqrt{\frac{2\Delta P_{\text{inflow}}}{\rho_{in}}} = \rho_{out} C_d A_2 \sqrt{\frac{2\Delta P_{\text{outflow}}}{\rho_{out}}} \tag{6.6}$$

where ρ_{in} and ρ_{out} refer to the indoor and outdoor air density, respectively; A_1 and A_2 refer to the area of opening on the left and right side of the building façade, respectively; C_{d} refers to the discharge coefficient, and given that airflow across both openings is turbulent, the values are both set to 0.6. The pressure difference on both inflow and outflow side can be expanded as follows. Note that p_{in} and p_{out} are static pressure, and the dynamic effect should be included as Equation (6.2) shows. And the indoor airflow velocity is assumed to be approximately zero compared to the external flow.

$$\begin{aligned} \Delta P_{\text{inflow}} &= \left(p_{out} + \frac{1}{2} C_{p1} u_{ref}^2 \right) - p_{in} \\ \Delta P_{\text{outflow}} &= p_{in} - \left(p_{out} + \frac{1}{2} C_{p2} u_{ref}^2 \right) \end{aligned} \tag{6.7}$$

Since for wind-driven natural ventilation, airflow is driven by wind pressure difference rather than the temperature difference, we can assume that indoor and outdoor temperatures are the same, and that the equality applies to ρ_{in} and ρ_{out}.

$$\rho_{in} = \rho_{out} = \rho \tag{6.8}$$

Combining Equation (6.5) – (6.7) and rearranging terms, we can finally get

$$\dot{V} = C_d A_1 \left[C_{p1} u_{ref}^2 \left[\frac{1 - \frac{C_{p2}}{C_{p1}}}{\left(\frac{A_1}{A_2}\right)^2 + 1} \right] \right]^{0.5} \tag{6.9}$$

To make the expression succinct , we define an effective opening area A_{eff} as follows.

$$A_{eff} = \left(\frac{A_1^2 A_2^2}{A_1^2 + A_2^2} \right)^{1/2} \tag{6.10}$$

Thus the air exchange flow rate is expressed as follows after plugging Equation (6.9) back into Equation (6.8).

$$\dot{V} = C_d A_{eff} \left(C_{p1} - C_{p2} \right)^{1/2} u_{ref} \tag{6.11}$$

From this expression, we can conclude that airflow rate in wind-driven natural ventilation is largely affected by the magnitude of the wind speed, the strength of the driving force, and the size of the openings for air to go through.

6.3 Case Study

Analysis of natural ventilation in buildings requires a comprehensive understanding of connections between indoor and outdoor airflow. In urban areas, outdoor flows are often very complex. They will change with urban context and perform quite differently from what we observe around isolated buildings. Hence, for designers to evaluate the natural ventilation potential for urban buildings, it is essential to understand the interactions of outdoor airflows with urban environment and building arrays.

A set of case studies is performed with nine uniform building blocks in the modeling domain (as is shown in Fig 3.7). The numerical settings (inlet wind condition, numerical resolution, etc.) are exactly the same as with that case. Details can be found in Chapter 3.2.1. For simplicity in the following discussions, we assume that openings of those buildings are located on the left and right side of façades.

Fig 6.3 shows relative wind pressure coefficients around the building array. Quantitatively, air exchange flow rate, a primary indicator of natural ventilation potential, is proportional to the square root of the differences of wind pressure coefficient (or relative wind pressure coefficient, since the subtraction cancels out the reference pressure term), as is shown in Equation (6.10). Based on the results below, we can make a qualitative conclusion that the first two columns of buildings are likely to have a higher flow rate of ventilated air if openings are set on the left and right side of building façades, but the last column suffers a lot. The magnitude of the differences of wind pressure coefficient is expressed by the contrast of colors. It is clear to see that the last column of buildings is immersed in a blue "sea" so that the differences of wind pressure coefficient on the opposite sides of the building façades are really tiny.

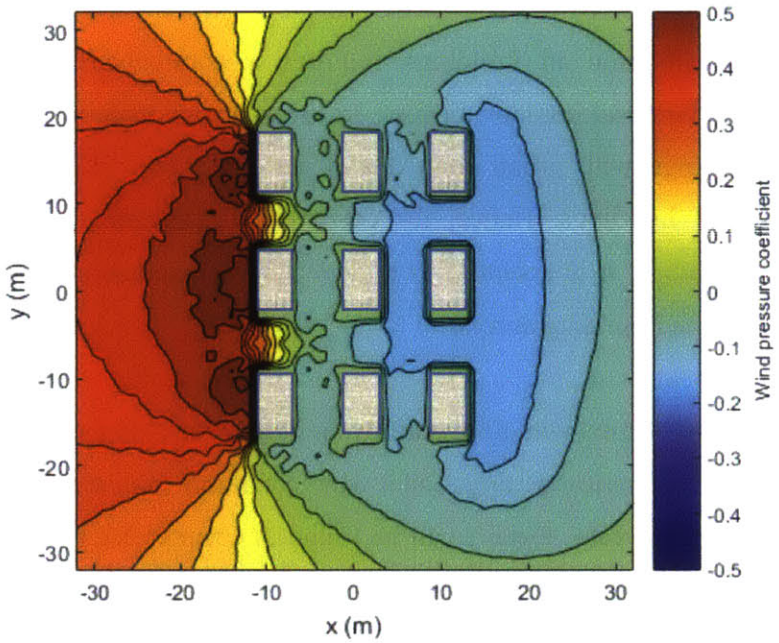

Figure 6.3. Wind pressure contour map in horizontal plane (at the height of respiration zone, z = 2 m) simulated by LBWFM.

Different modifications have been made to the initial design to improve the natural ventilation potential of the last column of buildings. Note that given the open boundary conditions instead of periodic ones on the edge of the domain, the symmetry in the building array determines that the geometic modification only makes sense on the middle building.

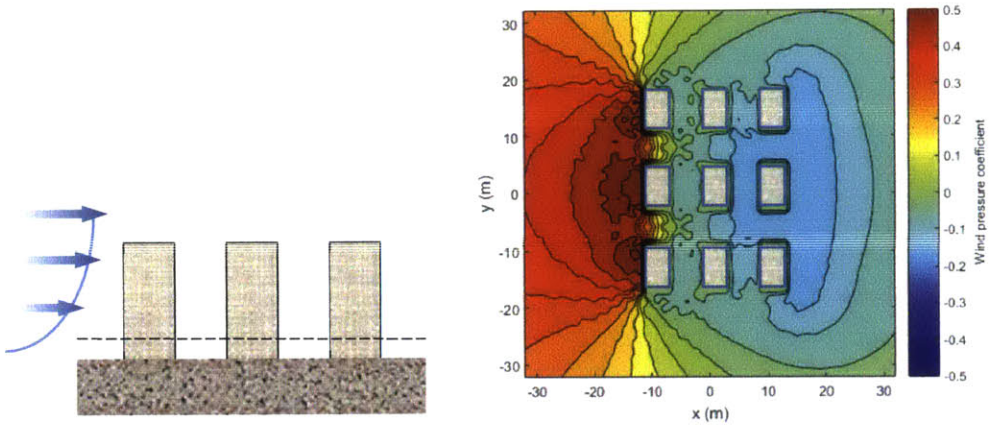

(*a*) Initial design with identical building heights

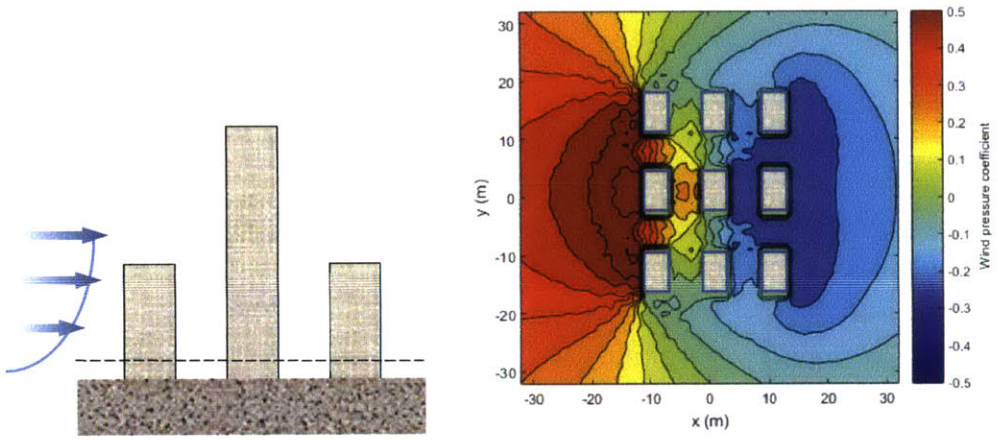

(*b*) Improved design with high-rise building in the middle

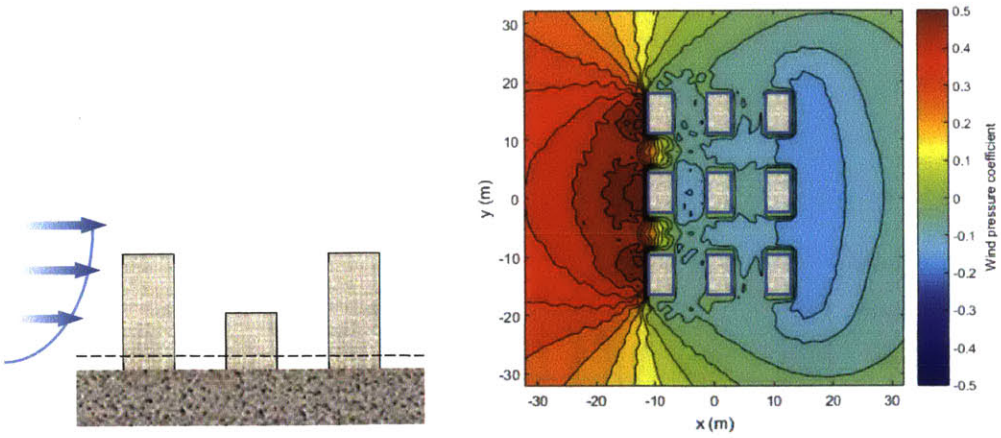

(*c*) Improved design with low-rise building in the middle

Figure 6.4. Comparisons of wind pressure coeffcient in horizontal plane for the three cases.

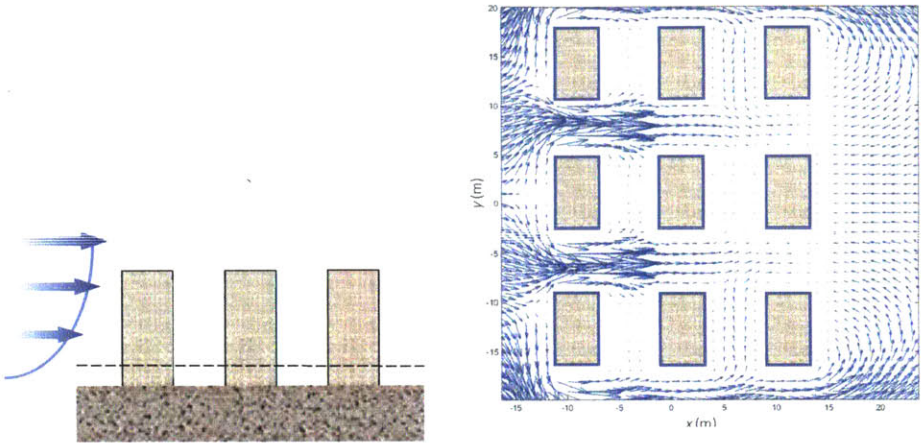

(*a*) Initial design with identical building heights

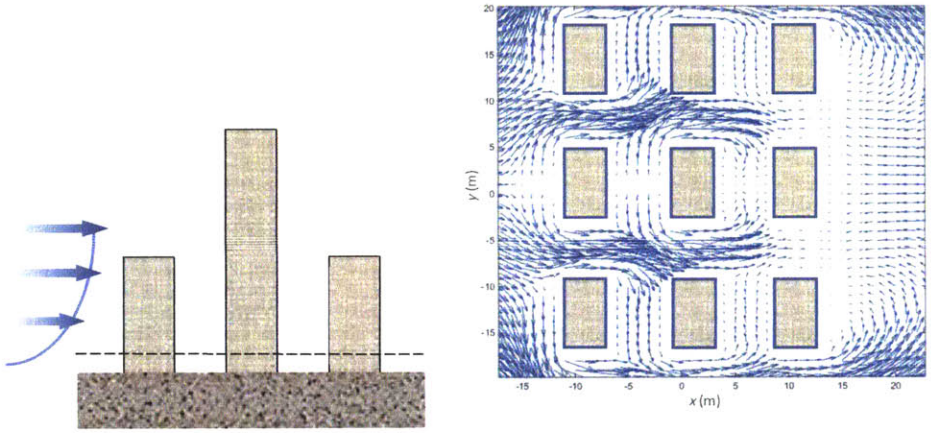

(*b*) Improved design with high-rise building in the middle

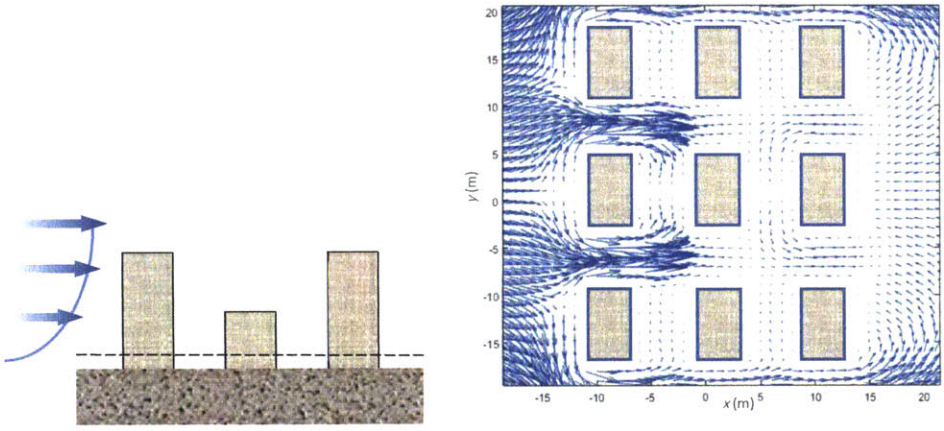

(*c*) Improved design with low-rise building in the middle

Figure 6.5. Comparisons of wind velocity in horizontal plane for different building heights.

Fig 6.4 shows the comparisons of wind pressure coefficients in the modified designs with the initial one when the height of the middle building changes. Sketches of the building design and inlet wind profile are plotted at the lefthand side. The contour map of relative wind pressure coefficient is obtained on the righthand side planed at the respiration zone cut with dotted lines on the left.

When the height of the middle building is twice that of the others, there is a large improvement at the second column. As we can see in the plots, the wind pressure coefficient increases on the front and decreases on the back, creating a larger difference on C_p values and thus leading to an increase in the airflow rate for the second column of buildings. However, the last column is not improved, although the absolute C_p values decrease. On the contrary, for the third design, the problem of less airflow through the opposite building openings is solved for the last column, after the height of the middle building is lowered to half of the others. The reason for this improvement can be further analyzed with the help of wind velocity field depicted in Fig 6.5. While the wind speed gets faster on the lateral sides of buildings for the design with an extruded building in the middle, wind speed on the front side of the last column gets faster for the design with a lower building in the middle. The differences of the wind pattern, contributing to the surface pressure changes near the openings, result from the changes of the configuration of the building array. For the case with a high-rise building in the middle, wind can be pushed down a lot into the front side of the second array because of the blocking effect of the extruded front façade. But air movement acts reversely on the back side of the array, since it must either wind across or climb up the tall middle building, thus creaing a larger difference of the surface pressure on the opposite façades. However, for the case with a low-rise building in the middle, wind will be flushed downward into both the front and back sides of the second array, and create higher pressure on the back side. The flushing effect also contributes to a reverse direction in pressure gradient for the second array as compared with the original and high-rise building cases. In conclusion, a low-rise building in the middle leads to the optimal design of the three cases for a naturally ventilated building community.

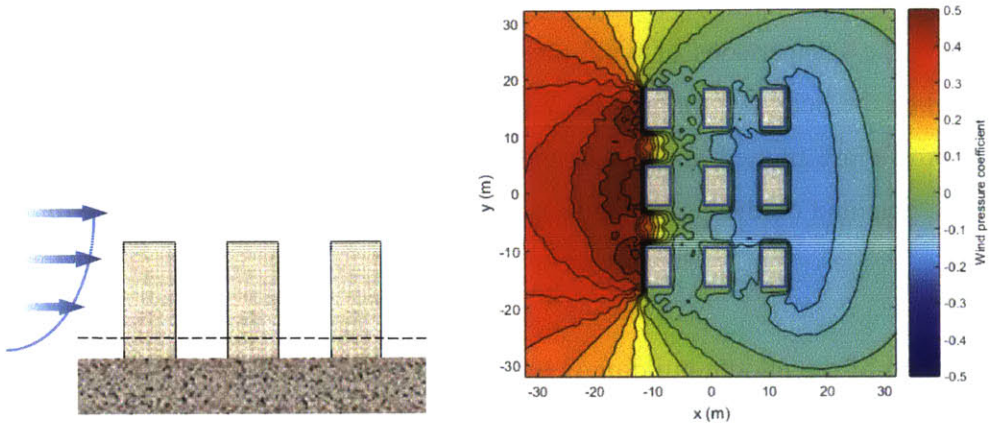

(*a*) Initial design with $\lambda_r \approx 1.3$

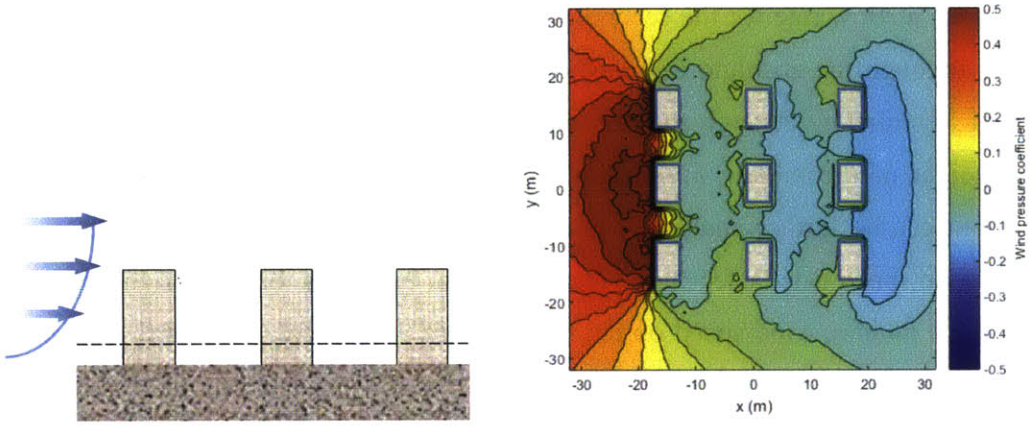

(*b*) Improved design with $\lambda_r \approx 0.7$

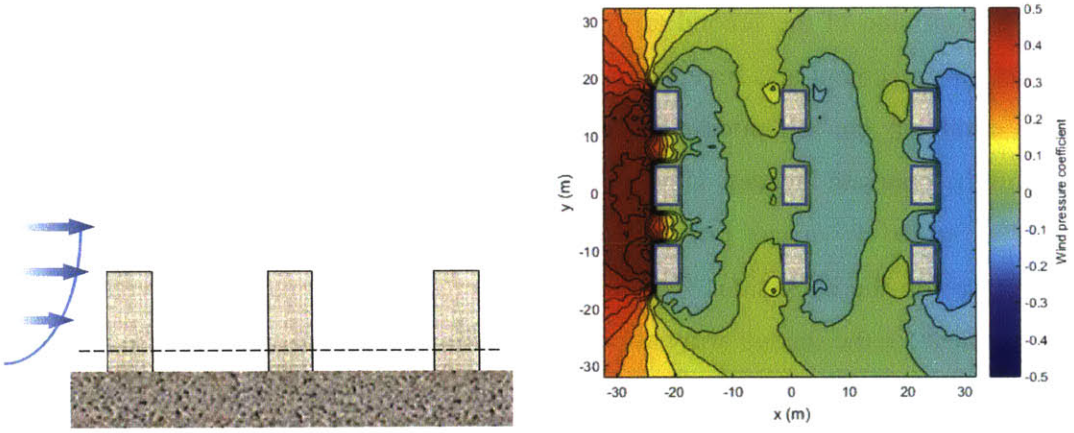

(*c*) Improved design with $\lambda_r \approx 0.4$

Figure 6.6. Comparisons of wind pressure coefficient in horizontal plane for different aspect ratios.

Besides the height of the middle building, another possible impact factor is the aspect ratio as is defined in Chapter 1.2.2. A comparative study is performed on wind pressure coefficient for the modified designs, as shown in Fig. 6.6. Sketches of the building design and inlet wind profile are plotted at the lefthand side. The contour map of relative wind pressure coefficient is obtained on the righthand side planed at the respiration zone cut with dotted lines on the left.

As the aspect ratio gets smaller, or in other words, the street width between neighboring building arrays gets larger, there are progressive improvements to the natural ventilation potential for the last column of buildings, as differences of relative wind pressure coefficient become greater. And even for the last case when $\lambda_r \approx 0.4$, the contour map shows self-similar wind pressure patterns around building façades, which is very close to the pattern with isolated buildings. Although it is clear to conclude that the smallest aspect ratio achieves the best natural ventilated building community, designers should be careful about the expenses paid to reach this solution, i.e. sparsely-distributed building design leading to less financial return and not applicable for densely populated urban environments. Other design metrics can be further modified to obtain an acceptable solution with a moderate aspect ratio.

We admit that other factors, e.g. shape of building array (scattered versus uniform array), orientation of buildings, can also affect the wind-driven airflow rate through the openings. The two case studies here present a possibility of using the LBWFM to give an answer to optimization of naturally ventilated building designs. Because the LBWFM provides detailed information of wind field parameters, its application can extend to analysis of outdoor thermal comfort when it combines with meteorological data and simulation results of temperature field and solar radiation, as well as analysis of pollutant dispersion behavior.

Chapter 7

Limitation and Discussion

7.1 Buoyancy effect on wind patterns in urban canyons

Throughout the work presented in previous chapters, the wind field is dominated by the mechanically-driven flow from the upwind direction. However, this is not always the case in the urban environment. When the outdoor wind speed is very low, solar radiation absorbed by building walls and ground may result in a large heating effect in the urban street canyon due to the reflection between the building façades. Heat is largely trapped between neighboring buildings, and temperature in the canyons will rise to be higher than the ambient temperature. Differences in the absorptivity and reflectivity of the surfaces also lead to the non-uniform surface heating in canyons (Dallman et al. 2014). In addition, because of heating and cooling systems in the housing, room temperature remains relatively constant compared to the seasonal changes of temperature for the ambient environment, which creates temperature differences between the indoor and outdoor environment (Truong 2012).

Temperature differences caused by these effects will generate thermally-driven flows circulating in the urban canyon area comparable to mechanically-driven flows in the wind-driven cases. Hotter air with lower density has the tendency to go up, and cooler air with higher density tends to go downward, represented by buoyancy forces driven by the density gradient. The buoyancy effect can create either vertical or horizontal flows based on the direction of the temperature gradient. For example, the temperature differences between the urban boundary layer and urban canopy layer will typically form a vertical buoyancy flow, whereas temperature differences between building façades will form a horizontal flow. These buoyancy flows can be combined with mechanical flows caused by upwind inertia force to concurrently affect the wind pattern.

7.2 Limitation of Lattice-Boltzmann wind field model

To clarify the effect of buoyancy force on the wind field model, a dimensionless parameter must be introduced in our analysis to quantify the importance of the buoyancy and inertia effects. As is known to all, the Grashof number approximates the ratio of the buoyancy to viscous force acting on a fluid, and the Reynolds number expresses the ratio of the inertia to viscous force. So we could combine the two dimensionless parameters to form the Richardson number, noted as Ri, relating the buoyancy and inertia forces.

$$\mathrm{Ri} = \frac{\text{buoyancy force}}{\text{inertia force}} = \mathrm{Gr}\,\mathrm{Re}^2 = \frac{g\,\Delta T/T\,L}{U^2} \tag{7.1}$$

Where ΔT is the absolute temperature difference either between urban canyons and the outer atmosphere or between building façades, T can be taken as the absoulate atmospheric temperature in Kelvin. In urban studies, the characteristic velocity is generally at the order of 1 to 10, while the characteristic length L, mostly refering to the height of the geometry, is at the order of 10 to 100. T values change with seasons, but still in a range of 230 to 320 K, and ΔT typically ranging within 5 K in most cases (Dallman et al. 2014, Nazarian and Kleissl 2016).

Equation (7.1) shows that in most breezy days (freestream velocity U is relatively large, and ΔT is quite small), the inertia effect dominates; however, in clear and calm conditions (freestream velocity U is quite small, and ΔT is relatively large), the buoyancy effect prevails. Note that the Lattice-Boltzmann Wind Field Model (LBWFM) is developed under the assumption that wind-driven flows are dominant at outdoors. So the model may not achieve an accurate result in purely buoyancy-driven flows or combined flows until some modifications are made in the modeling physics.

From the analysis above, we can then derive a critical freestream velocity as the criteria for designers to determine whether the Lattice-Boltzmann wind field model is appropriate for use.

$$\mathrm{Ri} = \frac{g\,\Delta T/T\,L}{U^2} \sim o(1) \;\Rightarrow\; U_{critical}(z_b) = \sqrt{g(2h)\frac{\Delta T}{T}} \tag{7.2}$$

Here note that the length scale is chosen for the blending height, calculated as twice of the average building height, as is defined and shown in Equation (4.26). Because of its equality between urban and rural areas, it is treated as the characteristic length parameter for the wind field analysis.

The critical velocity acts as a borderline between inertia dominance and buoyancy dominance. But to safely use our model which is assumed inherently wind-driven flow, we should define a minimum wind-driven freestream velocity U_w when the buoyancy effect accounts for only one tenth of the inertia effect.

$$\mathrm{Ri}_{critical} = \frac{g\Delta T/T\, z_b}{U_w^2} = 0.1 \Rightarrow U_w(h) = \sqrt{10}U_{critical}(z_b) = \sqrt{20gh\frac{\Delta T}{T}} \tag{7.3}$$

That is to say, only under the following condition, our LBWFM is robust and accurate enough for designers' use.

$$U(z_b) \geq U_w(z_b) \simeq 6 \text{ m/s} \tag{7.4}$$

Note that $h = 10$ m, $\Delta T = 5$ K, $T = 300$ K are used in the calculation above.

Because the freestream velocity at the blending height is an intermediate parameter calculated in the LBWFM, another criterion can be applied on the reference velocity and derived from Equation (4.30), (7.3) and (7.4).

$$u_{ref} \geq u_{ref,w} = U_w(z_b)\frac{\ln(z_{ref}/z_{0r})}{\ln(z_b/z_{0r})} \simeq 4 \text{ m/s} \tag{7.5}$$

Note that default values of $z_{ref} = 10$ m, and $z_{0r} = 0.1h$ are used in the calculation above. The result tells designers that when the reference velocity measured at the rural weather station is higher than 4 m/s, we can safely accept the wind field results simulated by LBWFM.

Similarly, a maximum buoyancy-driven freestream velocity U_b can also be defined for purely buoyancy-driven flows. Note that the inputs of parameter values are used as the same with the wind-driven case.

$$\mathrm{Ri}_{critical} = \frac{g\Delta T/T\, L}{U_b^2} \sim 10 \Rightarrow U_b(z_b) = \sqrt{0.1}U_{critical}(z_b) = \sqrt{0.2gh\frac{\Delta T}{T}} \simeq 0.6 \text{ m/s} \qquad (7.6)$$

Similarly to Equation (7.5), the criterion can also be applied on the reference velocity.

$$u_{ref} \le u_{ref,b} = U_b(z_b)\frac{\ln(z_{ref}/z_{0r})}{\ln(z_b/z_{0r})} \simeq 0.4 \text{ m/s} \qquad (7.7)$$

When the freestream velocity stands in between the values of U_b and U_w, or the reference velocity in between $u_{ref,b}$ and $u_{ref,w}$, as is summarized in Table 7.1, both buoyancy and inertia effect cannot be neglected, and the buoyancy term must be incorporated in the governing equation and solves the coupled Navier-Stokes equation and heat equation.

Table 7.1. Classification of wind-driven and buoyancy-driven flows.

Driving force for urban airflow	Freestream velocity at the blending height U (m/s)	The reference velocity at the rural weather station u_{ref} (m/s)
Buoyancy-driven	≤ 0.6	≤ 0.4
Combined buoyancy- and wind-driven	$0.6 \sim 6.0$	$0.4 \sim 4.0$
Wind-driven	≥ 6.0	≥ 4.0

7.3 Feasible modifications to the model

As discussed before, when the buoyancy force is included in the governing equations, the energy equation should be also coupled to the momentum equation and solved concurrently, as

temperature field will interact with wind field. Chapter 2 gives a detailed structure of the Lattice-Boltzmann Equation (LBE), which is equivalent to the Navier-Stokes equation under the continuum hypothesis. Now, we need to find the corresponding Thermal Lattice-Boltzmann Equation (TLBE), which is equivalent to the contimuum energy equation.

The LBE only accounts for the momentum viscous dissipation process in the collision operator. As is shown in Equation (2.25), the relaxation factor in LBE is defined as depending only on the momemtum diffusivity, implying that if energy equation is obtained from the same distribution function, it can only be applied in a certain condition where Prandtl number is approximately unity. So in order to achieve the general form of the energy equation in the lattice world, a new variable must be introduced, known as the internal energy density distribution function, which is defined as follows (He et al. 1998).

$$g = \frac{(\mathbf{e}-\mathbf{u})^2}{2} f \tag{7.8}$$

Where **e** is the particle velocity, as is given in Equation (2.16) if D3Q19 (shown in Fig 2.2 (b)) is applied as well; u is the macroscopic fluid velocity defined in Equation (2.10). Note that for differentiation, f is called the mass density distribution function, because the macroscopic density is expressed as the summation of f in all directions, as defined in Equation (2.8). Similarly, the summation of g in all direction gives the macroscopic internal energy.

$$e = \sum_i g_i = \frac{1}{2}\sum_i f_i(\mathbf{e}_i - \mathbf{u})^2 \tag{7.9}$$

Where e is the internal energy, and according to kinetic theory, $e = MRT/2$.

In order to describe the stochastic process of collision, we need to find the equilibrium state independent of particle orientations. A similar equilibrium internal energy density distribution function is defined as follows.

$$g^{eq} = \prod_{i}^{M} g_i(\mathbf{e}_i) \tag{7.10}$$

Then we can arrive at the expression of the equilibrium internal energy density distribution function by introducing the Maxwell-Boltzmann distribution function when we plug the correlation of the two distribution functions into Equation (2.6).

$$g^{eq} = \frac{(\mathbf{e}-\mathbf{u})^2}{2} f^{eq} = \frac{\rho(\mathbf{e}-\mathbf{u})^2}{2(2\pi RT)^{M/2}} \exp\left[-\frac{(\mathbf{e}-\mathbf{u})^2}{2RT}\right] \tag{7.11}$$

where ρ is macroscopic fluid density; R is the Boltzmann constant; T is temperature; M is the degree of freedom. As is similar to Equation (2.12), we use Taylor expansion on $\mathbf{u}$ and approximate to the second-order ($\mathbf{u}^2$). Equation (7.11) will be evolved as,

$$g_i^{eq} = \frac{(\mathbf{e}-\mathbf{u})^2}{2} \rho w_i \left(1 + 3(\mathbf{e}\cdot\mathbf{u}) + \frac{9}{2}(\mathbf{e}\cdot\mathbf{u})^2 - \frac{3}{2}\mathbf{u}^2\right) \tag{7.12}$$

where w_i refers to the weight function and can be calculated using Equation (2.16) for D3Q19.

In the continuous medium, the energy equation will have a form similar to the momentum equation if compression of fluid as well as the viscous dissipation can be neglected. Under the assumptions of incompressible fluid and negligible viscous dissipation effect, the TLBE, either in the continuous or discrete form, is constructed at a similar form with LBE (Guo and Zhao 2005).

$$\frac{\partial g_i}{\partial t} + \nabla(g_i \mathbf{e}_i) = \frac{1}{\tau_T}(g_i^{eq} - g_i) \tag{7.13}$$

$$g_i(\mathbf{x} + \mathbf{e}_i \Delta t, t + \Delta t) - g_i(\mathbf{x}, t) = \frac{1}{\tau_T}(g_i^{eq} - g_i) \tag{7.14}$$

To relate the relaxation factor to macroscopic properties, we can multiply Equation (7.14) with the second order of particle velocity **u**, and then sum them up in all possible directions, which coincides with the continuum energy conservation equations for an incompressible fluid. And thus we find that the relaxation factor depends on thermal diffusivity α (Chen et al. 1998, Mohamad 2011).

$$\tau_T = 3\alpha + 0.5 \tag{7.15}$$

To account for the buoyancy effect on the wind field, there will be an external force term on the LBE as well. Equation (2.21) will be modified as,

$$f_i\left(\mathbf{x}+\mathbf{e}_i\Delta t, t+\Delta t\right) - f_i\left(\mathbf{x},t\right) = \frac{1}{\tau}\left(f_i^{eq} - f_i\right) + \Omega_{F_i} \tag{7.16}$$

Here Ω_{Fi} refers to the collision operator induced by the buoyancy force. As compared to the continuum world, the external force is expressed as follows with the Boussinesq approximation (Lienhard 2013).

$$\mathbf{F} = \rho \mathbf{g} \beta \Delta T, \quad \beta \simeq \frac{1}{T} \tag{7.17}$$

In comparison with the momentum collision operator, the buoyancy operator will be evolved in the form of the following expressions. Note that Equation (2.19) should be satisfied for the operator as well. (Mohamad and Kuzmin 2010)

$$\Omega_{F_i} = w_i\left(\mathbf{e}\cdot\mathbf{g}\right)\beta\left(T - T_{ref}\right)/c_s^2 \tag{7.18}$$

Where T_{ref} is the reference temperature, referring to either cold wall or ambient temperature, usually set to 0 in the LBM scale (Mohamad and Kuzmin 2010).

Boundary conditions for the TLBE are set similarly as LBE. A bounce-back mechanism can also be applied in the temperature field when adiabatic condition is assumed. As an extension to a general Neumann boundary condition with finite heat flux, the bounce-back mechanism is conserved with the internal energy density distribution functions in all directions added up with a non-dimensional heat flux term. For Dirichlet boundary condition, where the temperature T_b is fixed, we can calculate the internal energy at the boundary and correlate to the internal energy density distribution function to give the values.

$$e_b = \frac{MRT_b}{2} = \sum_i g_i \tag{7.19}$$

Researchers have developed the TLBE to account for the heat transfer process and successfully applied onto natural convection (He et al. 1998, Guo and Zhao 2005, Mohamad 2011); however, either the simulation models only the temperature field and not coupled with LBE solver, or the coupling equations are only solved in two-dimensional flows (Mohamad and Kuzmin 2010). Thus the scalability and stability of the coupled LBE and TLBE in three-dimensional airflow simulation is still needed. Furthermore, the TLBE introduces another full set of distribution functions for evaluation, so the coupled solver increases to nearly twice the computational costs of the LBE alone. Comparisons of results between purely wind-driven flow and combined flow for urban airflow simulation should be made to see how much the error could be reduced when the extra complexity of the solving system is added, especially in the period of the annual local urban climate. If wind speed is smaller than the buoyancy-driven criteria listed in Table 7.1 for most of the days in a year, the modifications are then necessary to achieve reliable simulation results. All in all, a tradeoff has to be made between accuracy and computational efficiency in the requirements of the designer's workflow.

Chapter 8

Conclusions and future work

The Lattice-Boltzmann Method (LBM), a relatively newly developed numerical scheme to solve the fluid transport problem, combines the succinctness of the microscopic discrete kinetic equation and the efficiency of a macroscopic description of the field in a coherent manner, and bridges the gaps of the two scales by statistically averaged distribution. The LBM can largely reduce the computational cost due to its parallel nature, which is a desirable characteristic of numerical simulations in real applications, especially for the building design workflow. Because the wind field modeling is an essential precursor in an evaluation of outdoor thermal comfort, natural ventilation potential and pollutant dispersion behaviors to achieve thermally comfortable and energy-efficient building communities, a fast and relatively accurate analysis of wind field is needed for designers' use. Thus, the LBM can be integrated into the design workflow to show a 'real-time' wind field for a specific blueprint.

In this thesis, fundamentals of LBM are reviewed and a three-dimensional D3Q19 LBM model is developed and coded in C# language. To test the reliability of the LBM simulation results in airflow simulation, two case studies, one with a single building and the other with uniform building blocks, are performed and both wind velocity and pressure results are compared with experimental measurements and conventional CFD simulations. Results show that the LBM model can qualitatively catch the characteristics of turbulent flow past building blocks and quantitatively achieve high correlation factors with benchmark. When LBM is applied in real urban airflow simulations, a combined logarithmic and exponential or simplified uniform inlet wind profile is set and the momentum transport theorem is utilized to correlate rural meteorological measurements with urban wind field parameters. An adjustment distance is introduced to determine the optimal modeling domain size, which increases the computational efficiency without deteriorating the overall accuracy. The Lattice-Boltzmann Wind Field Model (LBWFM) is then constructed in a Rhino-based environment, making it possible for designers to

perform wind field analysis on a fast and relatively accurate platform. The LBWFM is also extended in the application of wind-driven natural ventilation analysis by calculating relative wind pressure coefficients and case studies are conducted to show the instructive effect of simulation results on design guidelines.

However, the LBWFM is developed under the isothermal assumption, while the wind field in real cases may also depend on buoyancy forces in the non-isothermal atmosphere. The criteria for the proper use of LBWFM is suggested, i.e. when the daily average of the reference velocity measured at the rural weather station is larger than 4 m/s.

Future work will be mainly focused on three aspects. First is the implementation of the thermal Lattice-Boltzmann equation in the LBWFM. Comparative studies will be performed between purely wind-driven flow and combined flow simulations for the urban airflow to assess the improvement of accuracy and potential increase in computational cost. Judgment will be then made for the necessity of the effort. Scalability and stability for the three-dimensional coupled solvers should be also investigated. Second is the implementation of LBM onto GPUs. Researchers have found that running an LBM simulation on GPUs could achieve 30% reduction in computational cost (Onodera et al. 2013). An assessment of the capital cost with respect to the improvement of accuracy should be conducted and well balanced. Third is the application of LBWFM in outdoor thermal comfort analysis. Wind velocity is one of the most important impact factors of outdoor thermal comfort, and studies will be performed on the combination of LBWFM with solar radiation modeling and meteorological data to provide a designer-relevant platform for numerical simulation.

References

Abe, Takashi. "Derivation of the lattice Boltzmann method by means of the discrete ordinate method for the Boltzmann equation." *Journal of Computational Physics* 131.1 (1997): 241-246.

ANSYS Fluent. http://www.ansys.com/Products/Fluids/ANSYS-Fluent

Arnfield, A. John. "Two decades of urban climate research: a review of turbulence, exchanges of energy and water, and the urban heat island." *International journal of climatology* 23.1 (2003): 1-26.

ASHRAE, FUNIP. "Fundamentals Handbook." *IP Edition* (2013).

Belcher, S. E., and O. Coceal. "Scaling the urban boundary layer." *COST Action.* Vol. 715. 2002.

Belcher, S. E., N. Jerram, and J. C. R. Hunt. "Adjustment of a turbulent boundary layer to a canopy of roughness elements." *Journal of Fluid Mechanics* 488 (2003): 369-398.

Bentham, Tom, and Britter, R. "Spatially averaged flow within obstacle arrays." *Atmospheric Environment* 37.15 (2003): 2037-2043.

Benzi, Roberto, Sauro Succi, and Massimo Vergassola. "The lattice Boltzmann equation: theory and applications." *Physics Reports* 222.3 (1992): 145-197.

Britter, R. E., and S. R. Hanna. "Flow and dispersion in urban areas." *Annual Review of Fluid Mechanics* 35.1 (2003): 469-496.

Bueno, Bruno, et al. "Computationally efficient prediction of canopy level urban air temperature at the neighborhood scale." *Urban Climate* 9 (2014): 35-53.

Bueno, Bruno, et al. "The urban weather generator." *Journal of Building Performance Simulation* 6.4 (2013): 269-281.

Chen, Hudong, et al. "Extended Boltzmann kinetic equation for turbulent flows." *Science* 301.5633 (2003): 633-636.

Chen, Shiyi, and Gary D. Doolen. "Lattice Boltzmann method for fluid flows." *Annual review of fluid mechanics* 30.1 (1998): 329-364.

Chen, Shiyi, et al. "Lattice Boltzmann computational fluid dynamics in three dimensions." *Journal of Statistical Physics* 68.3-4 (1992): 379-400.

Cheng, Hong, and Ian P. Castro. "Near wall flow over urban-like roughness." *Boundary-Layer Meteorology* 104.2 (2002): 229-259.

Chew, Y. T., X. D. Niu, and C. Shu. "Three-dimensional lattice Boltzmann BGK model and its application to flows with heat transfer in a rectangular microchannel." *International journal for numerical methods in fluids* 50.11 (2006): 1321-1334.

Chu, Chia R., et al. "Turbulence effects on the discharge coefficient and mean flow rate of wind-driven cross-ventilation." *Building and Environment* 44.10 (2009): 2064-2072.

Coceal, O., and S. E. Belcher. "A canopy model of mean winds through urban areas." *Quarterly Journal of the Royal Meteorological Society* 130.599 (2004): 1349-1372.

Coceal, O., and S. E. Belcher. "Mean winds through an inhomogeneous urban canopy." *Boundary-Layer Meteorology* 115.1 (2005): 47-68.

Coceal, O., et al. "Structure of turbulent flow over regular arrays of cubical roughness." *Journal of Fluid Mechanics* 589 (2007): 375-409.

Dallman, Ann, et al. "Conditions for thermal circulation in urban street canyons." *Building and Environment* 80 (2014): 184-191.

Etheridge, David W., and Mats Sandberg. *Building ventilation: theory and measurement.* Vol. 50. Chichester, UK: John Wiley & Sons, 1996.

Finnigan, J. J., and S. E. Belcher. "Flow over a hill covered with a plant canopy." *Quarterly Journal of the Royal Meteorological Society* 130.596 (2004): 1-29.

Finnigan, John. "Turbulence in plant canopies." *Annual Review of Fluid Mechanics* 32.1 (2000): 519-571.

Foken, Thomas. "50 years of the Monin–Obukhov similarity theory." *Boundary-Layer Meteorology* 119.3 (2006): 431-447.

Frisch, Uriel, Brosl Hasslacher, and Yves Pomeau. "Lattice-gas automata for the Navier-Stokes equation." *Physical review letters* 56.14 (1986): 1505.

Ghoniem, Ahmed F. "Needs, resources and climate change: clean and efficient conversion technologies." *Progress in Energy and Combustion Science* 37.1 (2011): 15-51.

Ginzburg, Irina. "Equilibrium-type and link-type lattice Boltzmann models for generic advection and anisotropic-dispersion equation." *Advances in Water resources* 28.11 (2005): 1171-1195.

Grasshopper. http://www.grasshopper3d.com

Grimmond, C. S. B., and Timothy R. Oke. "Aerodynamic properties of urban areas derived from analysis of surface form." *Journal of applied meteorology* 38.9 (1999): 1262-1292.

Guo, Zhaoli, and T. S. Zhao. "A lattice Boltzmann model for convection heat transfer in porous media." *Numerical Heat Transfer, Part B* 47.2 (2005): 157-177.

Hanna, Steven R., and Rex E. Britter. *Wind flow and vapor cloud dispersion at industrial and urban sites.* Vol. 7. John Wiley & Sons, 2010.

He, Xiaoyi, and Li-Shi Luo. "A priori derivation of the lattice Boltzmann equation." *Physical Review E* 55.6 (1997): R6333.

He, Xiaoyi, and Li-Shi Luo. "Lattice Boltzmann model for the incompressible Navier–Stokes equation." *Journal of statistical Physics* 88.3-4 (1997): 927-944.

He, Xiaoyi, Shiyi Chen, and Gary D. Doolen. "A novel thermal model for the lattice Boltzmann method in incompressible limit." *Journal of Computational Physics* 146.1 (1998): 282-300.

Higuera, F. J. "Boltzmann approach to lattice gas simulations." *EPL (Europhysics Letters)* 9.7 (1989): 663.

Inamuro, Takaji, Masato Yoshino, and Fumimaru Ogino. "A non□slip boundary condition for lattice Boltzmann simulations." *Physics of Fluids (1994-present)* 7.12 (1995): 2928-2930.

Kundu, P. K., and L. M. Cohen. "Fluid Mechanics, 638 pp." *Academic, Calif* (1990).

Lallemand, Pierre, and Li-Shi Luo. "Theory of the lattice Boltzmann method: Dispersion, dissipation, isotropy, Galilean invariance, and stability." *Physical Review E* 61.6 (2000): 6546.

Letzel, Marcus Oliver, Martina Krane, and Siegfried Raasch. "High resolution urban large-eddy simulation studies from street canyon to neighbourhood scale." *Atmospheric Environment* 42.38 (2008): 8770-8784.

Li, Xian-Xiang, et al. "Flow and pollutant transport in urban street canyons of different aspect ratios with ground heating: large-eddy simulation." *Boundary-layer meteorology* 142.2 (2012): 289-304.

Li, Xian-Xiang, et al. "Large-eddy simulation of flow and pollutant transport in urban street canyons with ground heating." *Boundary-layer meteorology* 137.2 (2010): 187-204.

Li, Xian-Xiang, et al. "Recent progress in CFD modeling of wind field and pollutant transport in street canyons." *Atmospheric Environment* 40.29 (2006): 5640-5658.

Liao, Quan, and Tien-Chien Jen. *Application of Lattice Boltzmann method in fluid flow and heat transfer*. INTECH Open Access Publisher, 2011.

Lienhard, John H. *A heat transfer textbook*. Courier Corporation, 2013.

Macdonald, R. W. "Modeling the mean velocity profile in the urban canopy layer." *Boundary-Layer Meteorology* 97.1 (2000): 25-45.

Martilli, Alberto, Alain Clappier, and Mathias W. Rotach. "An urban surface exchange parameterization for mesoscale models." *Boundary-Layer Meteorology* 104.2 (2002): 261-304.

Masson, Valéry. "A physically-based scheme for the urban energy budget in atmospheric models." *Boundary-layer meteorology* 94.3 (2000): 357-397.

McNamara, Guy R., and Gianluigi Zanetti. "Use of the Boltzmann equation to simulate lattice-gas automata." *Physical Review Letters* 61.20 (1988): 2332.

Mishra, Subhash C., Anjaneyulu Lankadasu, and Kamen N. Beronov. "Application of the lattice Boltzmann method for solving the energy equation of a 2-D transient conduction–radiation problem." *International Journal of Heat and Mass Transfer* 48.17 (2005): 3648-3659.

Mohamad, A. A., and A. Kuzmin. "A critical evaluation of force term in lattice Boltzmann method, natural convection problem." *International Journal of Heat and Mass Transfer* 53.5 (2010): 990-996.

Mohamad, Abdulmajeed *A. Lattice Boltzmann method: fundamentals and engineering applications with computer codes.* Springer Science & Business Media, 2011.

Monin, A. S., and AMf Obukhov. "Basic laws of turbulent mixing in the surface layer of the atmosphere." *Contrib. Geophys. Inst. Acad. Sci. USSR* 151 (1954): 163-187.

Mussa, Alberto, Pietro Asinari, and Li-Shi Luo. "Lattice Boltzmann simulations of 2D laminar flows past two tandem cylinders." *Journal of computational physics* 228.4 (2009): 983-999.

Nazarian, N., and J. Kleissl. "Realistic solar heating in urban areas: Air exchange and street-canyon ventilation." *Building and Environment* 95 (2016): 75-93.

Nourgaliev, R. Robert, et al. "The lattice Boltzmann equation method: theoretical interpretation, numerics and implications." *International Journal of Multiphase Flow* 29.1 (2003): 117-169.

Obrecht, Christian, et al. "Towards aeraulic simulations at urban scale using the lattice Boltzmann method." Environmental Fluid Mechanics 15.4 (2015): 753-770.

Oke, Timothy R. *Boundary layer climates.* Routledge, 2002.

Onodera, N., et al. "Large-scale LES Wind Simulation using Lattice Boltzmann Method for a 10 km× 10 km Area in Metropolitan Tokyo." *Tsubame ESJ* 9 (2013): 2-8.

Peng, Chen. "The Lattice Boltzmann method for fluid dynamics: Theory and applications." *M. Math, Department of Mathematics, Ecole Polytechnique Federale de Lausanne* (2011).

Peng, Y., C. Shu, and Y. T. Chew. "A 3D incompressible thermal lattice Boltzmann model and its application to simulate natural convection in a cubic cavity." *Journal of Computational Physics* 193.1 (2004): 260-274.

Raupach, M. R., and R. H. Shaw. "Averaging procedures for flow within vegetation canopies." *Boundary-Layer Meteorology* 22.1 (1982): 79-90.

Raupach, M. R., R. A. Antonia, and S. Rajagopalan. "Rough-wall turbulent boundary layers." *Applied Mechanics Reviews* 44.1 (1991): 1-25.

Rhinoceros. https://www.rhino3d.com/

scSTREAM. http://www.cradle-cfd.com/products/scstream/index.html/

Shirasawa, T., et al. "Development of CFD method for predicting wind environment around a high-rise building, Part2: The cross comparison of CFD results on the flow field around a 4: 4: 1 prism." *AIJ Journal of Technology and Design* 18 (2003): 441-446.

Stull, Roland B. *An introduction to boundary layer meteorology.* Vol. 13. Springer Science & Business Media, 2012.

Thömmes, Guido, et al. "A lattice Boltzmann method for immiscible multiphase flow simulations using the level set method." *Journal of Computational Physics* 228.4 (2009): 1139-1156.

Tominaga, Yoshihide, et al. "Cross comparisons of CFD results of wind environment at pedestrian level around a high-rise building and within a building complex." *Journal of Asian architecture and building engineering* 3.1 (2004): 63-70.

Truong, Phan Hue. *Recommendations for the analysis and design of naturally ventilated buildings in urban areas.* Diss. Massachusetts Institute of Technology, 2012.

Yu, Dazhi, and Sharath S. Girimaji. "Multi-block lattice Boltzmann method: extension to 3D and validation in turbulence." *Physica A: Statistical Mechanics and its Applications* 362.1 (2006): 118-124.

Yu, Dazhi, et al. "Viscous flow computations with the method of lattice Boltzmann equation." *Progress in Aerospace Sciences* 39.5 (2003): 329-367.

Yuan, Chao, and Edward Ng. "Building porosity for better urban ventilation in high-density cities–A computational parametric study." *Building and environment* 50 (2012): 176-189.

Yuan, Chao, Edward Ng, and Leslie K. Norford. "Improving air quality in high-density cities by understanding the relationship between air pollutant dispersion and urban morphologies." *Building and Environment* 71 (2014): 245-258.

Zhang, Raoyang, Hongli Fan, and Hudong Chen. "A lattice Boltzmann approach for solving scalar transport equations." *Philosophical Transactions of the Royal Society of London A: Mathematical, Physical and Engineering Sciences* 369.1944 (2011): 2264-2273.